Aerodynamic Shape Optimization of a Liquid-Hydrogen-Powered Blended-Wing-Body

V.F. Wilod Versprille

Technische Universiteit Delft

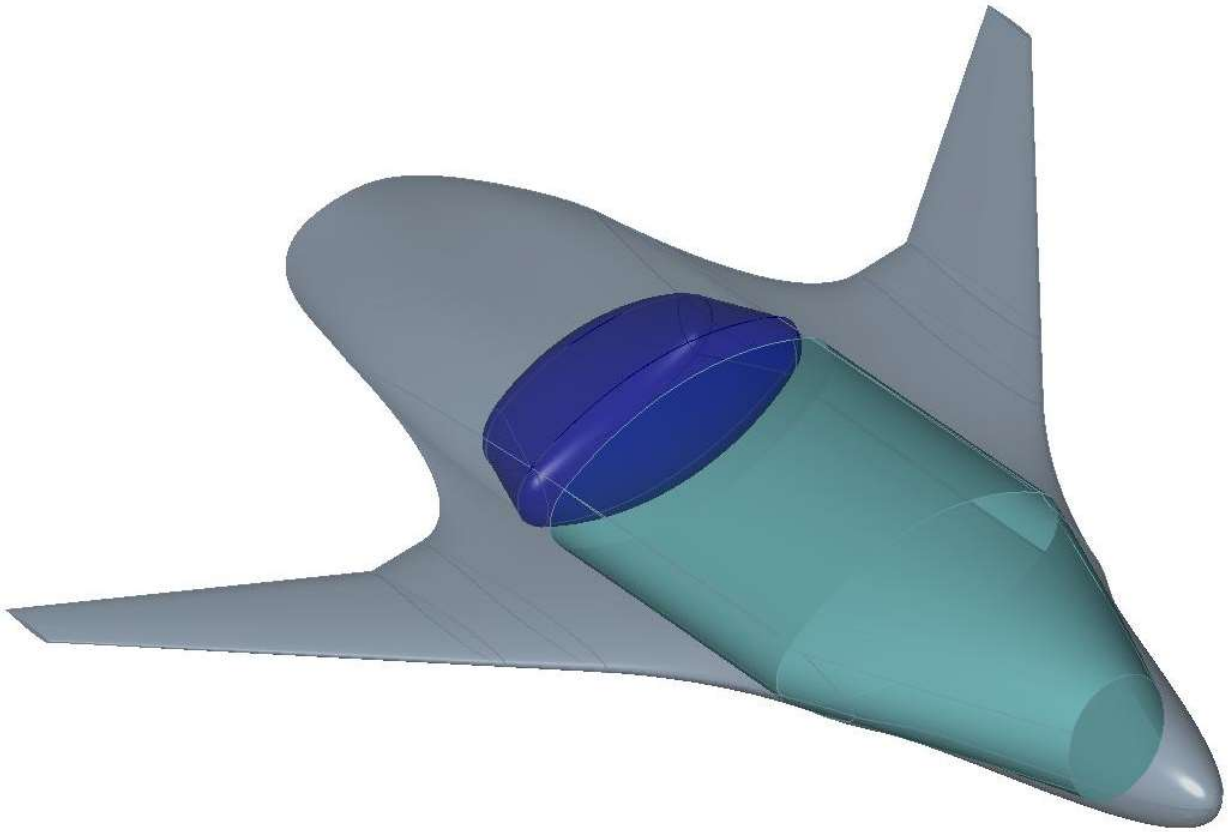

TU Delft Delft University of Technology

Challenge the future

Aerodynamic Shape Optimization of a Liquid-Hydrogen-Powered Blended-Wing-Body

by

V.F. Wilod Versprille

in partial fulfillment of the requirements for the degree of

Master of Science
in Aerospace Engineering

at the Delft University of Technology,
to be defended publicly on Monday February 21, 2022 at 09:30 AM.

Thesis committee: Dr. ir. G. La Rocca, TU Delft
Dr. ir. R. Vos, TU Delft
Dr. ir. A.H. van Zuijlen, TU Delft

An electronic version of this thesis is available at `http://repository.tudelft.nl/`.

TU Delft Delft University of Technology

ABSTRACT

While commercial aviation continues to grow, achieving climate goals set for this industry becomes more important. Since no major breakthroughs have been accomplished in the field of conventional kerosene-powered aircraft lately, new concepts and fuels are required. The use of liquid hydrogen as an aircraft propellant is currently considered to be one of the possibilities to accomplish a large reduction in the climate impact of aviation. However, the large volumes required for liquid hydrogen storage impose a challenge in aircraft implementation. The blended-wing-body concept is identified as a potentially suitable platform for integrating these large tanks due to its relatively large internal volume compared to its wetted area. The objective of this research is to attain the optimum aerodynamic shape of a liquid-hydrogen-powered, 150-passenger, medium-range, blended-wing-body. This is done by performing a constrained shape optimization for maximum aerodynamic efficiency.

The concept specifications and sizes follow from a kerosene-powered reference aircraft. The aircraft geometry is defined for an inside-out driven design where the cabin and tank are integrated in tandem into the centerbody. The ParaPy platform is used to couple the parameterized geometry to a meshing suite and the aerodynamic analysis methods. The geometry is transformed into an unstructured mesh by using the Salome platform. The aerodynamic analysis of the wave and induced drag consists of using the Euler equations and is computed within the Stanford University Unstructured code. Empirical strip methods provide the viscous drag estimate. Two optimization approaches are employed in this study, both making use of an evolutionary algorithm. Optimizations take place based upon a baseline design and include both geometric and aerodynamic constraints. The dual step approach consists of a 13-variable planform optimization followed by a 49-variable optimization of six two-dimensional profiles that are located along the span. The single step approach includes 50 variables of both the planform and wing profiles. The optimization computations take place at a single cruise condition where the Mach number is 0.78, the lift coefficient is equal to 0.2 and the atmospheric conditions follow from a cruise altitude of 11,000 meters.

The dual step and single step optimizations yielded an 8.7% and 7.5% performance increase compared to a baseline. The resulting lift-to-drag ratios of the optimized designs are 20.5 (dual step) and 20.3 (single step). Both optimizations resulted in different shapes. The single step optimization features an aft-positioned outer wing, which has a leading-edge sweep angle of 47-degrees. The dual step optimized design features a more forward-positioned wing with 51-degree leading-edge sweep. Both optimized designs do not display shock-waves and the lift distribution tends to an elliptical shape. The long center chord length of around 37 meter, results in a relatively low centerbody lift coefficient, while a cross-sectional area distribution close to a Sears-Haack body is attained.

PREFACE

This master thesis marks the end of my master's studies in Delft. There are several people I want to thank for helping me complete this work.
First of all, I want to thank my supervisor Roelof Vos. His inspiring lectures on aircraft design persuaded me to perform my research project in this field. During the thesis project, he has guided me towards a result that would not have been possible without his critical insights. Also, he never failed to motivate me during our meetings.
Furthermore, I want to thank Alexander van Zuijlen and Yaïr Brouwer for their help with setting up the SU2 computations as well as the connection with the HPC-cluster.
Then, I am grateful for the moments I shared with my fellow Aerospace Engineering student Tomas Fontes. Despite the COVID pandemic increasing the physical distance, we were always able to have a nice conversation.
I also want to mention my good friends Daan and Jeffrey and thank them for the great moments we shared.
What remains is to thank my family. By always being supportive and motivating me throughout the years, my parents provided a significant contribution to my completion of the study program. I am very grateful I can share this achievement with them. Finally, I want to thank my girlfriend, Jessica, for her love, confidence in my abilities and personal support during this thesis project.

V.F. Wilod Versprille
Delft, February 2022

CONTENTS

LIST OF FIGURES

LIST OF TABLES

NOMENCLATURE

Greek Symbols

α	Angle of Attack [°]
ϵ_{rel}	Relative Error [-]
ϵ_i	Twist Angle at Semi-Chord position [°]
Λ	Sweep angle [°]
λ	Taper ratio [-]
μ_{ow}	Outer Wing Longitudinal Positioning Parameter [-]
ϕ_{kink}	Spanwise Trailing-Edge Kink Location [-]
ρ	Density [kg/m^3]
v_i	Sectional Spanwise Location

Roman Symbols

$\bar{c}_f$	Equivalent Skin Friction Drag Coefficient [-]
$\dot{m}$	Mass Flow rate [kg/s]
$\boldsymbol{V}$	Velocity [m/s]
$a^{(i)}_{\text{LE,low}}$	Lower Leading Edge Cap Control Point [-]
$a^{(i)}_{\text{LE,up}}$	Upper Leading Edge Cap Control Point [-]
$a^{(i)}_{\text{TE}}$	Trailing Edge Outline Control Point [-]
A_i	CST coefficient [-]
b	Wingspan [m]
c	Chordlength [m]
C_D	Drag coefficient [-]
C_F	Skin friction coefficient [-]
C_L	Lift Coefficient [-]
c_l	Sectional Lift Coefficient [-]
C_m	Pitching Moment Coefficient [-]
C_P	Pressure Coefficient [-]
c_{center}	Center Airfoil Chordlength [m]
c_{ow}	Outer Wing Root Chordlength [m]
c_{ref}	Reference Chordlength [m]
C_{D_0}	Zero-Lift Drag coefficient [-]

$C_{D_{\text{inv}}}$	Inviscid Drag coefficient [-]
$C_{D_{\text{visc}}}$	Viscous Drag coefficient [-]
C_{D_i}	Induced Drag coefficient [-]
C_{L_α}	Lift Coefficient Slope [rad^{-1}]
C_{m_α}	Pitching Moment Coefficient Slope [rad^{-1}]
e	Span efficiency factor[-]
e_0	Oswald efficiency factor [-]
FF	Form factor [-]
h	Height [m]
h_1	Oval Fuselage Crown Height [m]
h_2	Oval Fuselage Cabin Height [m]
h_3	Oval Fuselage Keel Height [m]
h_{cruise}	Cruise Altitude [m]
l_{tank}	Tank Length [m]
M	Mach number [-]
p	Pressure [Pa]
r	Radius [m]
Re	Reynolds number [-]
T	Temperature [K]
t	Time [s]
t_{shell}	Shell Thickness [m]
V	Volume [m^3]
w_{cabin}	Cabin Width [m]
w_{fairing}	Fairing Width [m]
$w_{\text{low,i}}$	Lower Leading Edge Cap Control Point Weight [-]
$w_{\text{TE,i}}$	Trailing Edge Outline Control Point Weight [-]
$w_{\text{up,i}}$	Upper Leading Edge Cap Control Point Weight [-]
x_{NP}	Longitudinal Neutral Point Position [m]
z_{TE}	Trailing Edge Height [m]
a	Liquid Hydrogen Tank Allowance [-]
D	Drag [N]
F	Force [N]
L	Lift [N]

1

INTRODUCTION

Climate change has been a widely discussed topic for the past decades. Moving towards more sustainable forms of energy and transport is currently of major interest and aviation has its part herein as well. On the other hand, an annual growth for air passenger traffic of 4.2% is projected between 2018 and 2038 [10]. To reduce the climate impact caused by this growing aviation industry, emission goals have been set. The climate goals set by the European Advisory Council for Aeronautics Research demand a 50% reduction in CO_2 emissions by 2050 [11]. Also, NO_x and noise emissions will have to be reduced drastically.

Around 5.8% of the total oil consumption in the world concerns the aviation industry [12]. While oil is scarce, there is an ongoing worldwide demand for it. Hence the oil prices are expected to continue increasing [13]. Especially with a growing aviation sector, the dependency on fossil fuels should be reduced and the aircraft emissions should display a major decrease to meet climate goals. Research on engines, aerodynamics and air traffic management is ongoing. However, complying with the climate goals is not deemed possible with the use of conventional fuels [14].

One of the possible alternative fuels for aircraft is liquid hydrogen (LH_2). When used in a combustion engine, CO_2 emissions are eliminated and also NO_x emissions are expected to drop. Hence, if the hydrogen is produced in a sustainable way, climate impact can be reduced [15]. Once gradually introduced in the regional and narrow-body aircraft classes from 2035, hydrogen-powered aircraft are expected to yield a 6% to 12% aviation climate impact reduction by 2050 [16]. If hydrogen fuel cells become a feasible option for aircraft, sustainability is increased even further. Fuel cells do not produce any CO_2 and hence emissions only consist of water. However one of the challenges in the use of liquid hydrogen lies in its storage. Four times the volume compared to kerosene is needed to store an equal amount of energy of LH_2. Also, it requires cryogenic storage and therefore the tank needs to be insulated [9].

Another method to reduce aviation climate effects is by introducing aircraft concepts that are different from conventional tube-and-wing aircraft. Such concepts require a high design effort but can make a substantial contribution towards a greener form of air transport. One of these concepts is the blended-wing-body (BWB). This type of aircraft features a fuselage which provides a substantial part of the lift force. To do the latter, the cabin of a BWB has a non-round shape and an airfoil-like shape in the streamwise direction. The BWB is identified as a suitable LH_2 aircraft concept [17, 18]. Airbus recognizes its potential as well since it released the liquid-hydrogen-powered ZEROe aircraft concepts including a BWB in 2020[1]. The BWB has a relatively low wetted surface area compared to its internal volume [19]. This volume can be used to integrate the large LH_2 storage tanks. Also, the BWB concept in itself can provide an aerodynamic performance increase compared to a conventional tube-and-wing aircraft. For example, the BWB features a favorable aerodynamic and structural load distribution [19].

1.1. PROBLEM DEFINITION

Research has been conducted to find out whether a liquid-hydrogen-powered BWB indeed provides for a feasible concept. This research mainly consisted of integrating liquid hydrogen tanks into available BWB concepts [18, 20]. The studies were performed on a more conceptual level and were based on already existing kerosene-powered blended-wing-bodies. This resulted in a decrease in range due to a limited tank volume.

[1] https://www.airbus.com/en/innovation/zero-emission/hydrogen/zeroe, accessed at 09-02-2022

Hence, research results based on BWB's where the large fuel tank has been accounted for in the initial design are very limited. A study with an inside-out driven design that is sized to perform a pre-specified mission can therefore provide valuable results to conduct further research on this concept.

Since the increased internal volume is expected to cause a drag increment, shape features and aerodynamic efficiency are of particular interest. An initial design does not represent the full performance potential of the concept. So, to evaluate the feasibility of the liquid-hydrogen-powered BWB (LH2BWB) concept, an aerodynamic shape optimization study is required. More specifically, the focus is on a medium-sized aircraft.

The LH2BWB concept is based on the Airbus A320 passenger capacity and design range. The class of this aircraft type represents a substantial part of revenue passenger kilometers. This is why a sustainable version could make a noticeable change in aviation climate impact. Also, the aircraft class range yields a required fuel tank volume that is relatively limited and therefore more likely to be suitable for adoption by industry. To assess the feasibility of the concept, not only the aerodynamic aspect should be considered. Also sizing, structural weight and safety of an LH2BWB need to be evaluated in future research. This thesis research aims to provide these studies with beneficial aircraft shapes and a realistic estimation of the aerodynamic efficiency.

1.2. RESEARCH QUESTIONS & OBJECTIVE

Based on the problem description in the previous section, the objective of this study is as follows: to obtain the optimal aerodynamic shape for a liquid-hydrogen-powered blended-wing-body. More specifically, the aircraft must fit 150 passengers and have a medium range. To fulfill this objective, the following steps are performed:

1. Generating and sizing of an LH2BWB concept aircraft
2. Parameterizing the aircraft geometry
3. Coupling of aerodynamic analysis methods to assess aircraft performance
4. Setting up and running the aerodynamic shape optimization

The main research question for this study is as follows:

What is the constrained optimal shape in terms of aerodynamic efficiency during cruise of a medium-range, 150 passenger, liquid-hydrogen-powered blended-wing-body?

To answer the main question, the following sub-questions are formulated:

- How can a liquid-hydrogen-powered blended-wing-body be parameterized?
- Within this parameterized geometry, what shape maximizes the aerodynamic efficiency?
- What are the aerodynamic characteristics of the resulting shape optimized liquid-hydrogen-powered blended-wing-body?

By performing this research both insights on the geometry as well as aerodynamic performance features and figures are attained.

1.3. SCOPE OF THE STUDY

In the process of transforming a new concept into a shape optimized design, a range of assumptions are made. This study focuses on the parameterization of the LH2BWB concept and, the aerodynamic optimization of the shape for cruise conditions. Also, the research is limited to the 150-passenger, medium-range aircraft class. Although no detailed structural study is performed, structural feasibility is accounted for in the concept design and via optimization constraints.

This study does not focus on the conceptual design of the concept. The aircraft configuration used throughout this work is deemed to be a suitable design for the study at hand. Furthermore, the liquid hydrogen tank sizing is based on findings in literature. A more detailed tank sizing requires a thermodynamic model which is a research subject on its own. In this work, only performance around the cruise point of the aircraft is presented. Take-off and landing conditions are therefore not taken into account in the design.

Despite the assumptions, the result of this study is believed to be representative as an input for further research.

1.4. RELEVANCE

The outcome of this study provides aerodynamic values and insights that can be used in conceptual and preliminary design studies on the LH2BWB aircraft concept. Also, the geometry parameterization could serve as a basis for further research. The estimated aerodynamic performance gives an indication of whether the blended-wing-body indeed provides a suitable platform for the integration of liquid hydrogen. Finally, more insight into specific shape features for a BWB fitted with a liquid hydrogen tank is provided.

1.5. THESIS OUTLINE

This work describes research conducted on the aerodynamic shape optimization of the LH2BWB. Firstly, in Chapter 2 an overview of relevant literature on blended-wing-bodies, liquid hydrogen storage and aerodynamic analysis methods is provided. Secondly, the methodology used for concept generation, geometry parameterization and aerodynamic optimization is given in Chapter 3. Thirdly, a verification of the applied methodology is elaborated upon in Chapter 4. Fourthly, the experimental setup as well as the results can be found in Chapter 5. Finally, the conclusion and recommendations are presented in Chapter 6.

2

BACKGROUND INFORMATION

To provide a basis for the research conducted in this work, this chapter presents an overview of relevant literature findings. Firstly, Section 2.1 treats various aspects of the blended-wing-body concepts. Secondly, the use of liquid hydrogen is discussed in Section 2.2. Finally, Section 2.3 provides an overview of drag estimation methods.

2.1. BLENDED-WING-BODY AIRCRAFT

An aircraft concept has a range of characteristics that determine its overall performance. The most relevant of these properties are presented in the first part of this section. The second part elaborates on the aerodynamic shape optimization of BWB's, which is the main focus of this study.

2.1.1. BLENDED-WING-BODY CHARACTERISTICS

The blended-wing-body concept differs from the conventional aircraft configuration in multiple aspects. For clarity, first the distinction between pure flying wings and BWB's is explained. Martinez et al. [21] identify the presence of a flattened fuselage which is merged with the outer wing as the definition for a BWB. A pure flying wing displays straight leading and trailing edges. Some early examples of flying wings designs were made by Horten and Lippish around the second world war. Also Northrop developed flying wing concepts around this time, of which the piston powered XB-35 and the jet propelled YB-35 are examples [22]. After a period of low interest for the concept, the Northrop-Grumann B2 stealth bomber was introduced in 1988. This aircraft, which made use of the flying wing shape for stealth reasons, renewed attention to the concept [22, 23].

The development of the BWB concept started in the 1990s. One of the major studies on the BWB was initiated at McDonnel Douglas by Liebeck and funded by NASA [19, 24, 25]. The aircraft used in this study would later serve as a baseline design for research on a liquid-hydrogen-powered BWB in NASA's Quiet Green Transport study [18]. Studies that continued on the concept also included structural design [26]. The Multidisciplinary optimization of a Blended Wing Body (MOB) project is a European project that focuses on the multidisciplinary aspect of the design by developing tools and methods [27]. Within the MOB project, especially the studies of Qin et al. on BWB aerodynamics give useful insights on the aerodynamic optimization of the concept [28–30].

The BWB concept in general boasts advantages due to its centerbody providing a larger part of the lift compared to conventional aircraft. This leads to an aerodynamically efficient concept with a lower wetted area relative to its volume and a higher lift to drag ratio [19]. These beneficial proportions of the wetted area and the internal volume are also considered to make the BWB suitable for liquid hydrogen tank integration [13, 17]. Besides the higher volume-to-wetted-surface ratio, the interference drag is reduced compared to the conventional concept as well [28]. The study by Liebeck [19] mentions that a 27% reduction in fuel burn per seat could be achieved.

Noteworthy for the BWB are its wing loading and cruise lift coefficient. Since the use of high lift devices is limited, the maximum lift coefficient during landing is relatively low. Therefore the wing loading must also be low [19], which in turn can force the BWB to fly higher to be able to cruise at its optimum lift coefficient [31, 32]. Also the aspect ratio is relatively small. This causes the induced drag to rise quickly with the lift coefficient. So the optimum cruise lift coefficient in itself is relatively low [33]. To accommodate this optimum,

again a low wing loading is beneficial.

Another aspect of the integrated design is that the cabin deck angle cannot be too large. Therefore the centerbody must deliver the required lift at a relatively low angle of attack of 3° [19]. On the aspect of control and stability, the absence of a tail has some major implications. Concepts with or without a vertical tail both exist, but a horizontal tail is never present. The short moment arms for both directional and pitch control make the use of large control surfaces necessary [19]. Also careful design of the BWB's outer shape is crucial to achieving longitudinal stability due to the absence of a tail [34].

One of the major challenges in designing a BWB aircraft is the strong disciplinary coupling between structural integrity and aerodynamics. Therefore an optimization study often requires a multidisciplinary approach [33]. The bending moment on a BWB is reduced by two characteristics: the payload is efficiently distributed over the centerbody. Also the wing has to carry less load since the centerbody provides part of the lift [33]. This is beneficial for the structural weight. However, the centerbody also has to carry the cabin pressure loads [19]. Since the BWB cannot efficiently make use of cylindrical pressure vessels due to its shape, non-linear stresses are introduced that are difficult to predict [33]. Regarding the scalability of the BWB aircraft, Nickol [35] mentions two challenges. Since the height of a human is fixed, a BWB centerbody has a minimum thickness. This thickness imposes a chord length with a certain thickness-over-chord ratio. Also Greitzer et al. [36] mention that small-scale BWB's are less efficient than larger-scale BWB's, due to the height requirement. This leads to unused space and a larger wetted area.

2.1.2. AERODYNAMIC SHAPE OPTIMIZATION FOR BLENDED-WING-BODY AIRCRAFT

Multiple findings from studies on aerodynamic shape optimization of a conventional blended-wing-body are summarized to provide a basis on this subject. These findings can also be used to assess the specifics of integrating a liquid hydrogen tank.

Induced drag is one of the contributors to the total drag and can be minimized by aiming for an elliptical lift distribution. Qin et al. [29] demonstrated how this idea applies to a BWB. Several target lift distributions were defined for which the required twist distribution on the baseline planform was computed. This inverse design method does not aim to directly optimize the objective function but aims to find a geometry with certain characteristics on the flow field [37]. Qin et al.[29] employed a Reynolds-averaged Navier–Stokes equations (RANS) solver on the modified designs. They found that an elliptic load distribution led to a highly loaded outer wing. This caused a strong shock to occur, which raised the wave drag of the aircraft. Also a triangular lift distribution was tested. Since this distribution only moderately loaded the outer wing, the shock was weaker and the wave drag was reduced. However the induced drag was higher than for the elliptic distribution. A combination of a triangular and elliptical lift distribution was found to provide a balance between these two and leads to the highest L/D [30]. It should be noted that computations were performed at a C_L of 0.41 and Mach 0.85 during cruise. A lower cruise C_L might potentially yield a different optimal balance between a triangular and elliptical distribution, since the overall aerodynamic loading is lower. A study by Siouris and Qin [38] focused on the effect of wing sweep. It was found that by increasing the sweep angle, the strong shock and the accompanying wave drag could also be reduced. By using the sweep angle instead of the modified lift distribution to remove the shock, a more elliptical lift distribution was possible [38].

Lyu and Martins [39] performed a comprehensive aerodynamic study on the BWB configuration using a high fidelity (RANS) solver and a free form deformation optimization method. The design cruise conditions were set at a C_L of 0.206, at 10,666 m with Mach 0.85. A twist and shape optimized design led to an elliptical lift distribution and nearly shock-free aircraft. In a case where the aircraft had to be trimmed by constraining the moment around the pitching axis to zero, the optimization results showed two characteristics. The new shape and twist distribution featured a reflex near the trailing edge of the wing. This caused the lift to be generated more on the forward part of the sections. Also, the lift distribution showed a shift of the loading to the centerbody. This led to an increase in lift induced drag. Besides the lift being shifted more inboard, it also shifts forward following the wingsweep. Hence, the load shift on a swept wing proved to be a part of the optimum solution by absence of a tail surface [39]. By imposing constraints on the bending moment with reference to the baseline design, it became clear that a potential lighter wing structure has a large influence on the drag of the BWB. More lift is placed on the centerbody, which relieves the outer wing but also abandons the principle of elliptical lift distribution. This indicates the integrated nature of the BWB again. A planform optimization in this study indicated, that the span is limited by both the bending moment and the increase in wetted area.

The study by Peigin and Epstein [40] used the same baseline design as Qin et al. [29]. Using cruise conditions of C_L=0.41 and Mach 0.85, full Navier-Stokes computations were performed. A genetic algorithm (GA)

was used for the optimization process. An optimization without pitching moment constraint and using the airfoil shape design variables showed airfoil sections with strongly cusped trailing edges. These allowed for a drag reduction. However, the rear loading of the airfoil caused the nose-down pitching moment to increase. When this was limited by adding a constraint on the pitching moment, a drag reduction almost similar to the unconstrained version was achieved. Instead of a trailing edge cusp, now a drooped leading edge was present on the airfoil.

2.2. LIQUID HYDROGEN USE IN AIRCRAFT

The storage of liquid hydrogen introduces a challenge due to its low density compared to kerosene. Table 2.1 presents various properties of these two fuel types. It can be seen that more than ten times the volume compared to Jet-A is required, to store one kilogram of hydrogen in a liquid state at 101325 Pa. On the other hand, this one kilogram of hydrogen contains 2.8 times the combustion heat of one kilogram of Jet-A. This leads to hydrogen needing four times the volume as compared to Jet-A to contain the same amount of energy.

Table 2.1: Properties of hydrogen and kerosene at 101325 Pa [8, 9]

Parameter	Hydrogen	Jet A	Unit
Density (liquid)	70.9	811	kg/m^3
Heat of combustion	120	42.8	kJ/g
Boiling temperature	20.37	439.81	K

The boiling temperatures indicate that to store liquid hydrogen, well-insulated cryogenic tanks are required. Better insulation minimizes the boil-off of hydrogen and hence, the loss of usable fuel. This insulation can either be applied to the tank internally or externally [41]. Even with these cryogenic tanks, boil-off occurs due to heat input. Therefore, part of the liquid hydrogen in the tank is wasted [8]. Hence, a trade-off occurs between the amount of hydrogen allowed to boil-off and the insulation thickness. This trade-off is both relevant on the aspects of volume and weight [20].

The tank operating pressure that is chosen, should be higher than the ambient pressure, preventing outside air from flowing in. On the other hand, it should be as low as possible to minimize the tank volume and weight [8]. Brewer [9] suggested the venting pressure, which determines the operating pressure, to be set at 1.45 bar. Also, the tank shape influences the tank weight and volume. Spherical tanks provide the most efficient solution but since their shape is impractical, cylindrical tanks with a certain length are preferred [42]. The surface along which heat exchange can take place partially determines the boil-off. Therefore, the surface-to-volume ratio of a tank is an important factor. In a study on liquid hydrogen integration into the Flying V aircraft, van Woensel [43] has used an oval pressure shell to efficiently fit the tank into the available volume. Apart from insulation, a liquid hydrogen tank needs a metal or composite shell to sustain the internal pressure. Also, a liner can be required to prevent the small hydrogen molecules from dissipating through the tank wall [42]. Both the tank wall and liner have a relatively low thickness contribution on the tank [20].

In the Cryoplane project, a study on the application of liquid hydrogen technology to a range of aircraft sizes was performed by multiple aircraft manufacturers and universities [1]. The main relevant findings are the following:

- Short- and medium-range conventional aircraft need the hydrogen tanks to be placed on top of the fuselage, as shown in Figure 2.1 [1]. This configuration causes an increase in drag.
- The OEW over MTOW fraction is almost constant for all studied hydrogen aircraft types. Each of them shows an empty weight fraction of 0.68. The MTOW remains more or less constant with respect to kerosene versions.
- The studied hydrogen aircraft show an energy consumption increase per passenger transported over a nautical mile, compared to their kerosene counterpart. For the medium-range aircraft this increase is equal to 10%, and is mainly caused by an increased wetted area. It should be accepted that hydrogen requires an increased energy use because the climate impact of hydrogen is much smaller than for kerosene.
- In a combustion engine, the energy specific fuel consumption ESFC for hydrogen and kerosene differs only by 1%.

- A hydrogen-powered BWB was also studied in the project and deemed less viable due to inefficient use of internal volume. The long cylindrical tanks were fitted in the longitudinal direction, alongside the passenger cabin.

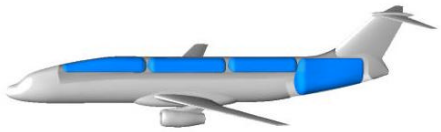

Figure 2.1: The short/medium-range aircraft concept in the Cryoplane study [1]

Smith [44] proposed a design for a very large BWB powered by a hydrogen-fueled distributed electric propulsion system. A kerosene-based aircraft was used as fixed outer shell. The aircraft design mission is to carry 555 passengers with a 7650 NM cruise range at Mach 0.85. The purely hydrogen-driven version requires a hydrogen storage volume of 1,060 m^3. Using cylindrical tanks for the pure hydrogen design, only 405 m^3 of storage space is available. Hence tank integration comes at the cost of passenger capacity.

Goldberg [20] fitted liquid hydrogen tanks into the cargo bay of the existing N3X concept with an estimated L/D of 25. However, only 30% of the kerosene concept fuel energy content could be stored in this manner. Hence, less than half of the original aircraft range remained.

Finally, Guynn et al. [18] studied the performance of a 225 passenger, 3500 NM range BWB that is powered by liquid hydrogen fuel cells. The study took internal volumes into account based on rough assumptions and therefore did not provide a real inside-out approach. A relatively low L/D of 16 was achieved, which was partially caused by a low cruise altitude of 7.5 km. Also, the analysis method used for aerodynamic performance estimation was originally intended for conventional aircraft.

2.3. DRAG ESTIMATION

The aerodynamic performance of an aircraft is often quantified by the drag coefficient at a given lift coefficient. This results in the lift-over-drag ratio of an aircraft. The total drag is built up by various drag components. To get a clearer view of these components that are key in increasing the aerodynamic efficiency, firstly a recap is given in the following section. Subsequently, the Computational Fluid Dynamics (CFD) analysis method is discussed.

2.3.1. AIRCRAFT DRAG COMPONENTS

Multiple approaches to the concept of drag exist. Two of these approaches are discussed here. The first viewpoint is that of aerodynamics in which the drag is attributed to various aircraft features. This leads to a more practical view from an aircraft design standpoint. Examples of distinguished types of drag are trim drag and inlet drag [2].

The trim drag requires attention in the case of a BWB. Liebeck [19] notes that the aerodynamic center of pressure should be located exactly in the center of gravity to have a trimmed BWB. If this is not the case, a control surface deflection is needed to trim the aircraft longitudinally. Since the elevator moment arm is short [19] and the elevator deflection affects the flow on the centerbody of a BWB [39], a small pitching moment should be aimed for on a BWB.

Fluid mechanics is the second possible viewpoint. A division is made between the drag originating from different fluid mechanics phenomena. This viewpoint is applied throughout this work. It allows the ability to reduce drag systematically. Also, there is coherence between drag computations and fluid mechanics. These factors contribute to the wide application of the viewpoint in this field of research. By looking at Figure 2.2 [2], three different contributions can be identified:

- **Profile drag** consists of two components: the pressure drag and the skin friction drag. Viscous pressure drag is caused by normal forces on a body of which lift can be a part. Skin friction drag arises from the tangential forces. Due to the viscosity of the fluid, the flow is slowed down in the region adjacent to the surface. This region is also known as the boundary layer. Whether the boundary layer is laminar or turbulent has a large influence on the skin friction drag [45, 46].

Since this drag is caused by viscosity, inviscid methods are not able to estimate it accurately. So different methods are needed to take the boundary layer into account.

- **Induced drag** is present due to the generation of lift on a 3D wing. This lift causes trailing edge vortex shedding which in turn causes an induced angle of attack. This induced angle of attack limits the effective angle of attack. The resulting force vector on the wing causes the induced drag. This force vector shows a larger inclination with the free stream compared to the case of an infinite wing [2]. The relation of the induced drag to the lift coefficient according to Prandtl's lifting line theory is as follows:

$$C_{D_i} = \frac{C_L^2}{\pi ARe} \tag{2.1}$$

The span efficiency factor (e) in this equation relates closely to the lift distribution and thus is often used to reduce the induced drag.

Methods that can model induced drag are Trefftz Plane analysis [2] and Vortex Lattice Methods (VLM)'s [47]. Examples of VLM are Tornado and the Athena Vortex Lattice (AVL).

- **Wave drag** occurs when supersonic flow regions are present on a body. In the transonic regime, this leads to shockwaves decelerating the flow to subsonic speeds. The momentum loss in such a shock wave leads to wave drag [46]. Although this phenomenon is inviscid, the shock wave leads to a pressure rise and an adverse pressure gradient. The gradient causes the boundary layer to thicken or even separate, increasing the profile drag. The thickening of the boundary layer only is referred to as weak interaction by Vos and Farokhi [48]. When separation occurs as well, strong interaction takes place. In these cases, laminar boundary layers separate earlier than turbulent ones [48].

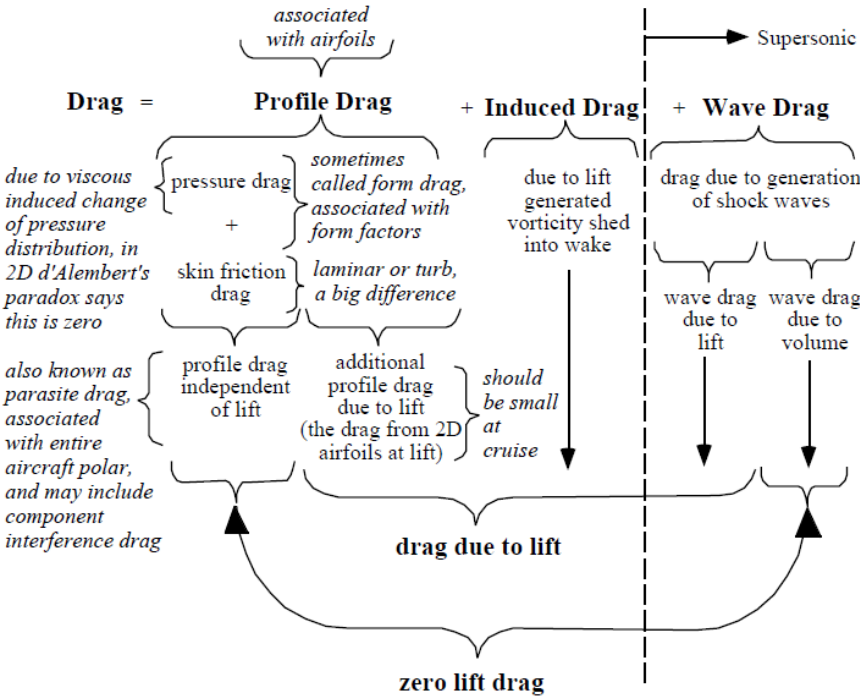

Figure 2.2: Breakdown of the various drag contributions from a fluid mechanics perspective [2]

2.3.2. COMPUTATIONAL FLUID DYNAMICS

When using CFD, computers solve the governing equations of fluid dynamics directly, using numerical methods [47]. These Navier-Stokes equations are a set of non-linear partial differential equations, that can be solved using various levels of simplifications. An overview is given in Figure 2.3 [3]. At the top of the flowchart,

the most complex methods are found. In Direct Numerical Simulation (DNS), all turbulence scales are resolved. This requires an enormous computational effort and hence the technology for aircraft scale application will not be ready for decades [47].

A Large Eddy Simulation (LES) resolves the large turbulence scales and models small turbulence scales. A grid refinement hence leads to numerical and physical improvements. For industrial use, LES still requires too large computational resources however [49].

RANS is the most complex solver that can be used on a full-scale aircraft. All turbulence scales are modeled in this method. It is suitable for attached boundary-layer flows and also steady separated flows according to Cummings et al. [47]. If large regions of unsteady separated flows occur, the RANS approach becomes inaccurate.

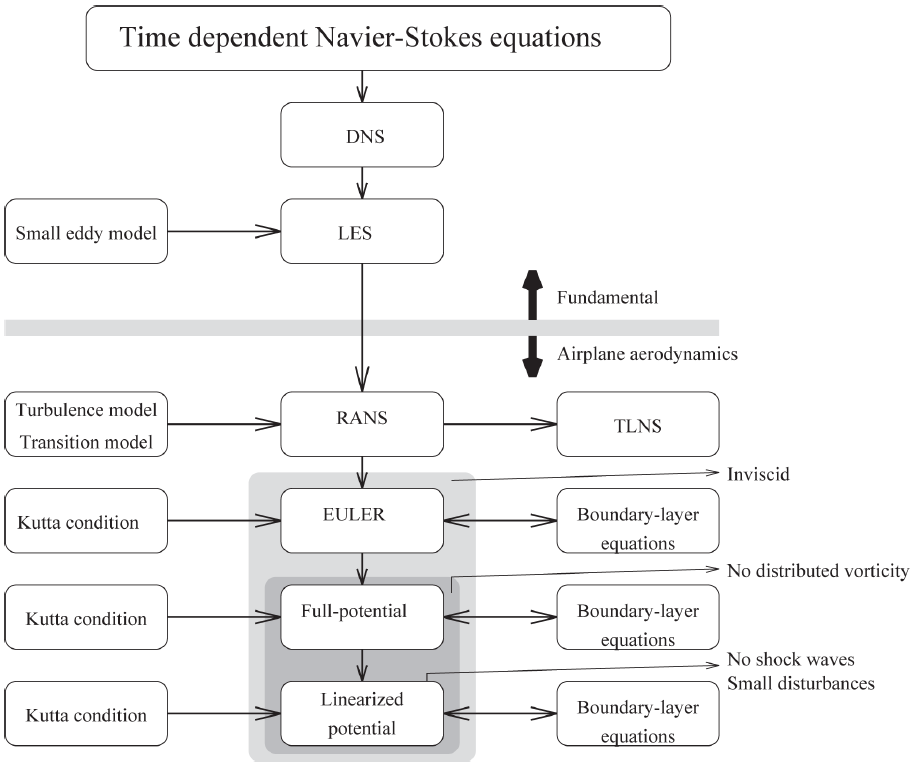

Figure 2.3: Flowchart on mathematical flow models [3]

When the viscous and heat-transfer terms in the RANS equations are omitted, a set of equations called the Euler equations remains. The resulting continuity, momentum and energy equations are given in the following equations respectively:

$$\frac{D\rho}{Dt} + \rho(\nabla \cdot \boldsymbol{V}) = 0 \tag{2.2}$$

$$\rho \frac{D\boldsymbol{V}}{Dt} = -\nabla p \tag{2.3}$$

$$\rho \frac{De}{Dt} + p(\nabla \cdot \boldsymbol{V}) = 0 \tag{2.4}$$

These equations can be solved faster than the RANS equations, which makes it attractive for an optimization study with limited computational resources [48].

The cruise speed of the BWB in this research is within the transonic domain. The chosen method must be able to make an accurate estimation of the effects of the shock wave on the flow since shock waves are expected to occur on the aircraft [30, 50]. Vos and Farokhi [48] explain the relation between Crocco's theorem, given below 2.5, and the shock waves:

$$\frac{\partial \boldsymbol{V}}{\partial t} - \boldsymbol{V} \times \zeta = T\nabla s - \nabla H \tag{2.5}$$

This equation relates the vorticity of the flow (ζ) to unsteady effects ($\partial \boldsymbol{V}/\partial t$), entropy gradients ($\nabla s$) and enthalpy gradients (∇H). In a shock wave, an entropy discontinuity is present across the shock wave. Since Crocco's theorem relates the entropy gradient to vorticity, shock waves can be captured only in rotational flow. When looking at Figure 2.3, it can be seen that the Euler equations are the simplest method that still take vorticity into account. Therefore the method provides a balance between computational effort and the accuracy that is required for the research at hand.

One of the shortcomings of the Euler equations is not including the effect of a thickened boundary layer after a shock wave. The added 'displacement thickness' alters the effective curvature of the body and therefore influences the pressure distribution. The boundary layer thickening is especially relevant for transonic low Reynolds numbers flow conditions. Although a BWB usually operates at high Reynolds numbers, this should be kept in mind when assessing the results on Euler computations. The same applies to the strong interaction between boundary layer and shock wave. Since the full potential and linearized potential do not take vorticity into account, these methods are not treated.

3

METHODOLOGY

To attain the optimum aerodynamic shape for a new aircraft, a set of methods and strategies is in place. These are described in this chapter following the order in which they are applied during the study. Firstly, Section 3.1 describes the generation and sizing of the LH2BWB concept. Secondly, the manner in which the concept geometry is parameterized can be found in Section 3.2. Thirdly, the method applied to transform the geometry into an optimum aerodynamic shape follows from Section 3.3. The aerodynamic analysis methods used in the optimization method are elaborated upon in Section 3.4

3.1. AIRCRAFT SPECIFICATIONS AND ASSUMPTIONS

An aerodynamic optimization of a BWB that accounts for a liquid hydrogen tank already in its initial shape, has not been conducted in any major study yet. Also, no suitable concept was found as starting point for the optimization. Therefore, a new concept has been generated for this purpose. Firstly, the required specifications are elaborated upon. Secondly, the design is presented on a general level. A detailed description of the parameterization can be found in Section 3.2

3.1.1. AIRCRAFT SPECIFICATIONS

To be able to compare the resulting LH2BWB aircraft, it should have similar capabilities as a widely used conventional aircraft. Therefore, the reference aircraft specifications in Table 3.1 are used as requirements for the LH2BWB concept. The CSR-01 is a conventional tube and wing design which has a medium range and passenger capacity [4]. It bears a strong resemblance to the Airbus A320 aircraft, as can be seen in Figure 3.1 [4].

Table 3.1: Key specifications for the CSR-01 reference aircraft [4]

Parameter	Value
Design range at max. payload	2750 NM
Passenger number	150
Cargo	7 LD3-45 containers
Maximum fuel weight	18700 kg Jet-A
Design payload	13608 kg
Maximum structural payload	20000 kg

The absence of a structural weight estimation of the new concept prevents the use of the Breguet range equation. So, the hydrogen fuel weight required for attaining the design range of the CSR-01 cannot be estimated directly. Therefore, the reference aircraft's maximum fuel weight is converted to a liquid hydrogen fuel weight that matches its total energy content. This maximum fuel tank energy content is equal to 800 GJ, which translates to 6670 kg of liquid hydrogen. With the liquid hydrogen density provided in Table 2.1 this requires a volume 93.9 m^3. As discussed in Section 2.2, the storage of liquid hydrogen is less straightforward than for kerosene. Losses due to boil-off as well as insulation have to be accounted for since they require a non-negligible volume. Based on the work by van Woensel [43], a polymer foam with a thickness of 17 cm is

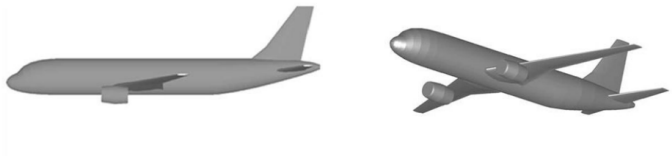

Figure 3.1: The CSR-01 reference aircraft [4]

chosen as insulation. Although the hydrogen tank in this study has a different shape and a higher volume, this is deemed a suitable starting point.

Together with the tank surface area, which depends on the aircraft design, the extra required volume can be calculated. The chosen insulation thickness leads to an estimated boil-off rate, $\dot{m}_{\text{boil-off}}$, of 0.1% per hour. Over a flight time, t_{flight}, of six hours this accumulates to 0.6 m^3 LH_2. Additionally an 4.8% allowance, a, of the required liquid hydrogen volume is suggested by Brewer [9]. The allowance accounts for volume that cannot be used for liquid hydrogen due to tank contraction, internal tank systems and the volume needed to prevent an over-pressure. These lost fuel volumes are added to the total required volume for fuel storage. By applying the above in the equation below an internal tank volume of 98.5 m^3 results:

$$V_{\text{tank,internal}} = V_{LH_2} \cdot \left(1 + t_{\text{flight}} \cdot \dot{m}_{\text{boil-off}} + a\right) \tag{3.1}$$

The cabin floor area sizing is based on a floor area of 1.09 m^2/pax. This value is based on a cabin with 9% business class seats and 91% economy class seats as found by Baan [51]. This floor area per passenger yields a cabin floor area of 137.5 m^2. The economy class seat and aisle width used for the cabin are 0.51 m and 0.48 m respectively [51]. The floor width of the aft cabin is sized based on the economy class seat layout. In the LH2BWB, a 3-4-4-3 abreast seat configuration is chosen for its practicality and efficiency. Also, the resulting cabin floor shape is satisfactory in terms of width to length ratio. Including a 0.2 m margin for cabin structures, leads to a cabin floor width of 9.0 m. This configuration serves as a starting point. To find the actual most efficient seat-placement, a cabin configuration study for the resulting designs should be conducted in further research. A cabin height of 2.1 m is chosen since it allows most humans to stand while the resulting minimum centerbody thickness is still limited. The cabin box has an internal volume of 288.8 m^3. This value excludes the oval shell structure outside of the cabin box. The latter is partially used for the storage of cargo containers.

3.1.2. LH2BWB CONCEPT DESIGN

The LH2BWB concept configuration can be examined in Figure 3.2. Its design is based on the oval fuselage concept by Hoogreef and Vos [52]. When used in a BWB concept, it provides a coupling between the internal cabin and the centerbody outer shape. This concept is elaborated upon in Section 3.2. The LH_2 tank also makes use of oval shapes and is located behind the cabin, adopting the shape of the aft cabin oval. Both the front and aft-facing parts of the tank are fitted with a dome to increase structural feasibility. The layout of the pressure shell at the aft cabin section can be examined in Figure 3.3. A minimum height of 45 inches between cargo floor and cabin floor is maintained to fit the cargo containers as well as the cross beams to support the cabin floor. A cockpit is not accounted for, but the remaining empty volume available in the nose section is deemed large enough for its integration.

The outer shape can be divided into three main components as can be seen in Figure3.2: the centerbody, the wing fairing and the outer wing. A reflexed airfoil with an initial thickness-to-chord ratio of 14.6% is fitted to the centerbody to house the cabin and tank. The outer wing includes both the surface featuring the straight trailing edge as well as the surface outboard of this area. It features a linear planform and its shape consists of supercritical airfoils. It is connected to the centerbody with a fairing which gradually adopts the outer wing profile when moving outboard.

The part of the centerbody behind the tank allows for engine and control surface placement. However, only the clean flying wing is taken into account for aerodynamic calculations in this study.

3.2. PARAMETERIZATION

To be able to aerodynamically optimize the LH2BWB aircraft concept, an inside-out driven parameterization of the geometry is made. This process entails describing a shape with a set of variables and parameters. This

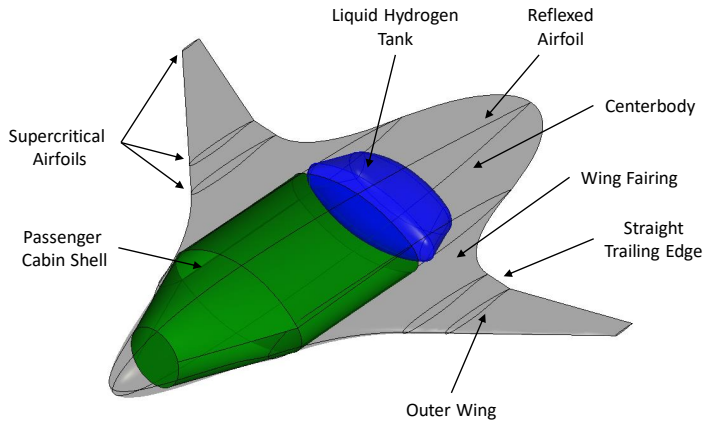

Figure 3.2: Isometric view of the LH2BWB concept

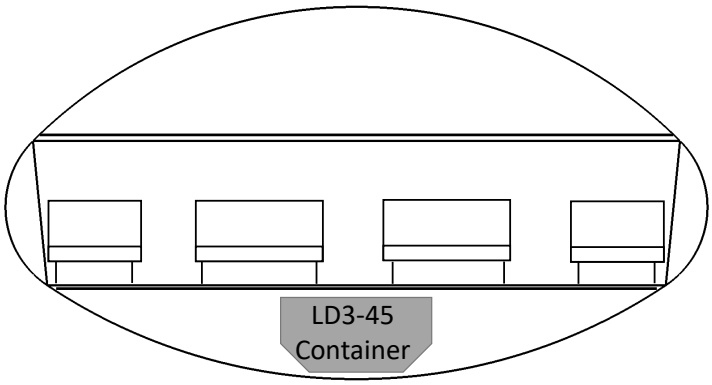

Figure 3.3: Pressure shell configuration concept

section will elaborate on the parameterization in the following manner. Firstly, a summary on the *ParaPy* Knowledge Based Engineering (KBE) software, which is used as the framework for this project, is given. Secondly, the inside-out buildup of the model is treated step by step, in the same order as it is carried out in *ParaPy*. Finally, a detailed view of the defined parameterization is given. The latter is described separately for the internal volumes, planform layout and airfoil shapes.

3.2.1. PARAPY PLATFORM

The Python-based *ParaPy*[1] software is used as the platform to carry out this study. This KBE platform allows for automatic geometry generation which can subsequently be put through coupled analysis modules. The KBE approach has multiple features that reduce computational effort and increase the ease of geometry evaluation. Examples of these features are runtime caching, demand-driven evaluation and dependency tracking [53]. Three important reasons for the selection of the *ParaPy* framework are the following:

- It allows for readily available optimization algorithm implementation, since its Python-based
- The basis for a coupling between the geometry, *Salome* meshing tool and the SU2 analysis software is available from the work by Hillen [54] and Faggiano and Vos [55].
- Multiple geometric shapes are already parameterized and hence can serve as a basis for the parameterization of the LH2BWB

The implementation of the parameterization in *ParaPy* is further elaborated upon in Appendix A.

[1] https://www.parapy.nl/ accessed at 14-10-2021

3.2.2. AIRCRAFT GEOMETRY PARAMETERIZATION OVERVIEW

To turn the concept into a geometry that can be optimized, a parameterization is made. The latter is aimed to be both robust and flexible to be suitable for optimization [37]. Also, variables are used as efficiently as possible to reduce the size of the design vectors used in the optimization.

This section treats the different steps and techniques used to create the geometry used for this research project. To provide a general overview of the parameterization a step-wise buildup is provided first.

Accounting for the LH_2 fuel tank in the initial design introduces the necessity for an inside-out driven approach. This approach is visually represented in Figure 3.4. The starting point of the design is the passenger cabin as can be seen in Figure 3.4a. This is followed by the generation of oval sections which form the cabin pressure shell (3.4b). Also, the generation and integration with the tank to form a shell containing the internal volumes is part of this step. Caps and fairings are fitted to cross-sections of this shell to attain an aerodynamic shape on the centerbody (3.4c). These newly created sections are then lofted (3.4d). Finally, the wing fairings and outer wings are merged with the centerbody (3.4e). The use of the oval cabin shape in a BWB and the fitting of caps, wings and fairings are partially derived from the work by Brown and Vos [56].

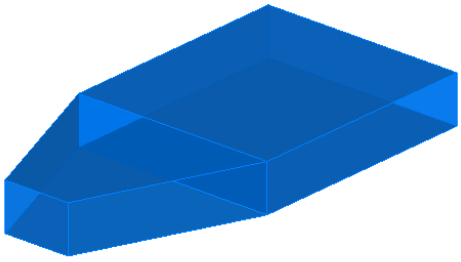

(a) Generation of the cabin box

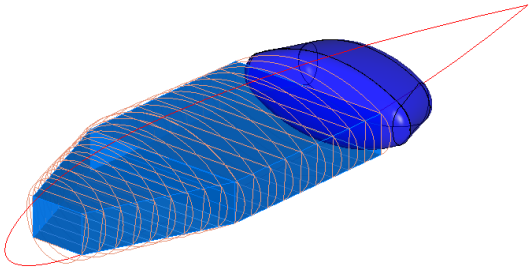

(b) Cabin (orange curves) and tank (black curves) oval generation based on center airfoil

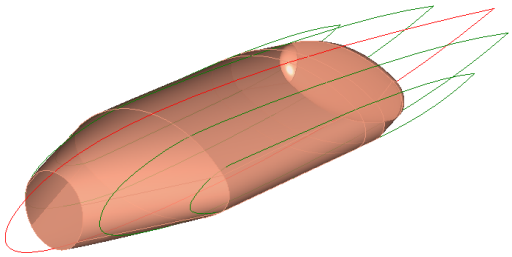

(c) Fitting caps to streamwise sections

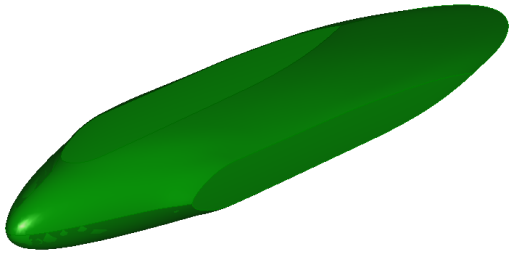

(d) Spanwise lofting of the centerbody sections

(e) Merging centerbody with fairing and outer wing

Figure 3.4: Stepwise representation of the LH2BWB outer mold line generation

3.2.3. INTERNAL VOLUME PARAMETERIZATION

The internal volumes for which a parameterization is made consist of two main components. The first is the passenger cabin shell. Its parameterization is described separately for both the layout and structure.

The second component described in this section, is the liquid hydrogen tank. These two components do not fill the entire available volume and hence space is available for aircraft systems that are not specifically accounted for.

CABIN FLOOR LAY-OUT

The passenger cabin has the shape of a baseball 'homeplate' as can be found in literature [35]. Figure 3.5a shows the front cabin consists of a trapezoid, while the aft cabin floor has a rectangular shape. In this study, the front width is fixed at 3 m, which should be sufficient for a cockpit base width. The cabin width w_{cabin} for the aft part of the cabin is fixed at 9 m in this work. This value aims for an efficient fitting of a 14 seat abreast configuration including 3 aisles according to the dimensions stated in Section 3.1. Only discrete width values allow the efficient fitting of a fixed number of seats abreast. However discrete values are not preferable for optimization, since they can 'mask' optima with the chosen optimization algorithm [57]. Therefore the cabin width is part of the parameterization but is not a variable in the optimization performed in this research. The cabin floor area follows from Section 3.1 and is set to 137.5 m^2. The front cabin sweep angle, Λ_{cb}, is therefore the only variable in the cabin floor layout in this study. The front cabin area is calculated first because its shape is fixed by the widths and sweep angle. The remainder of the required floor area then defines the length of the rectangular aft cabin shape, since its width is already defined. The cockpit itself is not modeled, but is accounted for by leaving sufficient room until the most forward point of the aircraft.

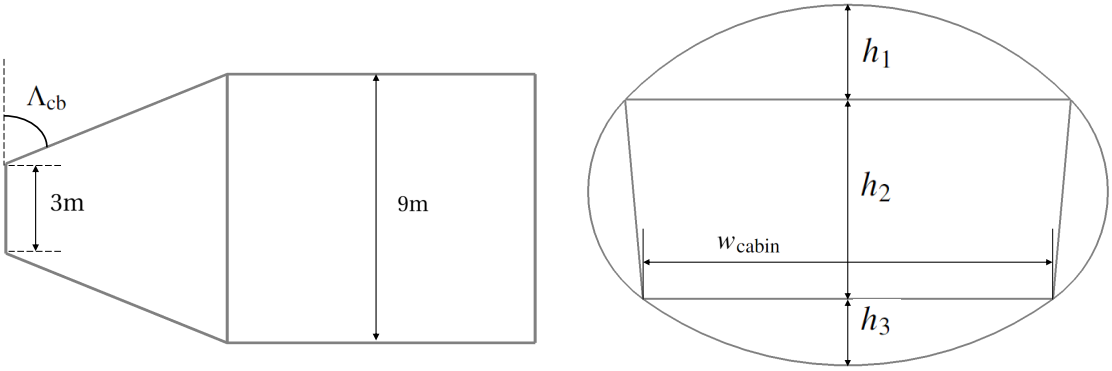

(a) Cabin floor shape parameterization

(b) Oval fuselage concept parameterization

Figure 3.5: Parameterization of the passenger cabin as applied in this work

OVAL FUSELAGE SHAPE

The coupling between an aerodynamic outer shape and an internal structure is made by utilizing the oval fuselage concept by Vos and Hoogreef [52]. It aims to reduce structural weight by applying an inside-out-driven approach. The parameterization features a shell with an oval cross-section which contains a rectangular cabin shape, as can be seen in Figure 3.6 [52]. When the oval shell is pressurized, forces are transferred through nodes A and B in the figure. This causes the vertical sidewall of the cabin to become loaded by a tension force while the horizontal plates of the cabin carry a compressing force. This concept forms an efficient option to handle the cabin pressure loads [52]. The oval fuselage parameterization forms a direct coupling between the inside and outside geometry and was therefore deemed suitable for this study.

In this study, the arc radii follow from the local crown (h_1), cabin (h_2) and keel (h_3) heights at a specific section as can be seen in Figure 3.5b. The oval cabin width w_{cabin} is set at floor height. The crown and keel heights are determined by the center airfoil thickness at this section and hence provide a connection between the outer shape of the aircraft and the internal layout as can be seen in Figure 3.4b. Thick airfoil sections are preferable from a structural point of view. These imply smaller arc radii and lower stresses but are often not beneficial in terms of aerodynamic performance. Since the opposite also applies, a trade-off is present which can be accounted for using a multidisciplinary optimization. This study does not consider any structural load calculations. Therefore, minimal arc radii are set as constraints during aerodynamic optimization.

The airfoil shape on the centerbody is defined by CST-coefficients, which is discussed later in this section. The actual shape of the body in *ParaPy* follows from defining 10 ovals each for the front cabin and the aft cabin and subsequently lofting them separately. These two shapes are then merged to form a fused cabin shell. Despite this being a stable method to form the cabin shell, only zeroth-order continuity is attained on

the transition section. If this would not be corrected, sharp peaks in the pressure distribution occur. Therefore a smoothing process is carried out in a later stage of the parameterization. The geometric inconsistency this causes is further discussed in Section 4.1.

Another consequence of using the oval fuselage concept is that the airfoil section at the cabin sidewall is flat. Since the cabin height is constant, no airfoil curvature is present in this part. However, the leading and trailing edge caps still provide design flexibility. The pressure distribution in this section is elaborated upon in Chapter 5.

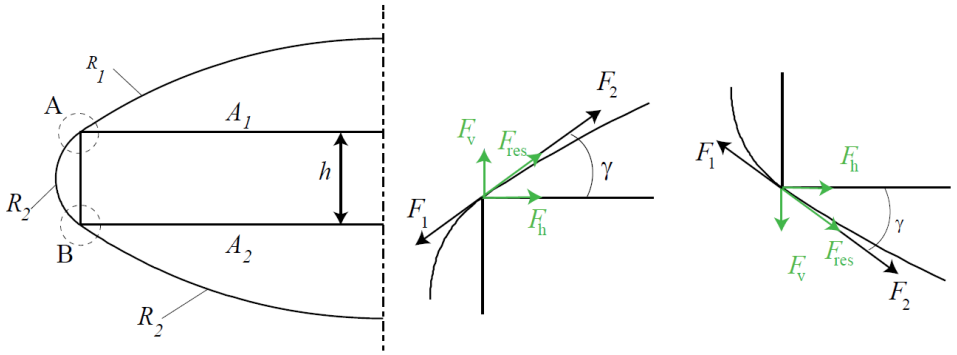

(a) Semi cross section (b) Force balance at A (c) Force balance at B

Figure 3.6: Overview of the oval fuselage concept and its load transfer mechanism [5]

LIQUID HYDROGEN TANK PARAMETERIZATION

The liquid hydrogen tank is located behind the passenger cabin as can be seen in Figure 3.2. Similar to the passenger cabin, the tank also adopts the oval pressure shell shape. The parametric model follows the work by van Woensel [43]. This model deviates from earlier studies where mostly cylindrical tanks are used. It aims to make efficient use of the available internal volume while maintaining a feasible structure.

As can be seen in Figure 3.7, the center section of the tank contains the majority of the volume. It consists of two linearly lofted ovals, set apart by tank length l_{tank}. The front tank oval adopts the height ratios of the aft cabin oval but is scaled in height to the local center airfoil thickness. The front tank width $w_{\text{tank,front}}$ is identical to the aft cabin width of 9 m. For the aft tank oval, the width $w_{\text{tank,aft}}$ follows from a tank sweep angle Λ_{tank} and the front tank oval width. Hence $w_{\text{tank,aft}}$ is a dependent parameter. Tank widths are defined at the bottom plane of the internal trapezoidal structure. The aft tank oval height for h_2 follows from the following equation:

$$h_{2,\text{tank,aft}} = 1.4 \cdot h_{2,\text{tank,front}} \cdot \frac{w_{\text{tank,aft}}}{w_{\text{tank,front}}} \tag{3.2}$$

The factor of 1.4 is deemed to provide a balance between aft oval radii and the efficient use of available space. Without this factor, the aft tank oval would feature small arc radii due to the tapering of the tank and the relatively small airfoil thickness decrease. This value is found for a tank sweep angle of 23°. Furthermore, the aft tank oval has equal crown and keel heights to attain an optimal stress distribution in the oval.

The domes on both sides of the ovals are formed by lofted semi-ellipses. These ellipses have a ratio of 1.6 between the major axis and minor axis. According to Brewer [9] this value provides the best balance between the structural weight and available volume use within an aircraft. Based on the parameterization above, the liquid hydrogen tank has only two variables apart from the airfoil shape, which are the tank length and sweep angle. During the optimization, these parameters are fixed at a tank length of 2.5 m and a tank sweep angle of 23° to attain the desired volume and fixed. The insulation foam thickness is multiplied by the tank surface area to obtain the insulation volume. This volume is subtracted from the tank volume to yield the effective volume. This effective volume should then be sufficient for the required liquid hydrogen volume.

3.2.4. PLANFORM LAYOUT DEFINITION

The planform parameterization seeks to combine the centerbody shape with a flexible planform outline bearing aerodynamically favorable features. The planform layout can be seen in Figure 3.8. Table 3.2 presents parameters that are fixed during the optimization to ensure a robust geometry. The layout defines the positions of the sections that are used for the lofting process. The outcome of the lofting process determines the actual

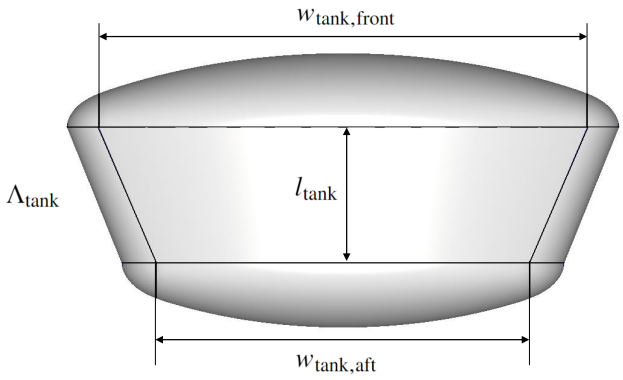

Figure 3.7: Bottom view of the liquid hydrogen tank parameterization

planform outline which is shown in green. The chord lengths for the center airfoil and outer wing mainly determine the aircraft size. The centerbody planform shape partially depends on the cabin floor shape defined earlier. Two sections are present at a spanwise fraction v_i. It was experienced at least two cross-sections at each side of the symmetry plane are required to provide satisfactory consistency between the cabin pressure shell and the outer mold line (OML). Since using more sections introduces more variables, two cross-sectional locations per side are utilized. The leading edge outline is based upon a fixed distance, t_{shell}, from the cabin wall. This definition is chosen since it provides for a limited thickness of aircraft doors. The intended trailing edge outline follows a method from literature where it is defined by a Bézier curve (red in Figure 3.8). This curve has 4 control points, $a_{\text{TE}}^{(i)}$, which are positioned such that they provide tangency at the endpoints of the curve [58, 59]. Each control point has a weight, $w_{\text{TE},i}$, to alter the shape of the curve. The weights of control points 1 and 2 are a variable in the optimization. The control points at the start and end of the curve have a fixed value of 1. This is deemed to provide sufficient flexibility while using a limited amount of variables.

On the centerbody, the (green) OML follows the intended (red) outline. On the wing fairing, a slight difference occurs due to the lofting process. This difference is visible in Figure 3.8. The longitudinal position of the cabin with reference to the centerbody airfoil follows from the front cabin as can be seen in Figure 3.8.

Positioning of the outer wing is performed with reference to the leading edge of section 2 via μ_{ow} and w_{fairing}. The longitudinal position of the outer wing root is in terms of center chord fraction. Since the spanwise position is coupled to the front cabin sweep line, this sweep parameter influences the leading edge of the outer wing root in 2 dimensions: x and y. The fairing width is added to provide sufficient spanwise offset for a smooth transition towards the outer wing. The outer wing layout is defined by a span b_{ow}, leading-edge sweep angle Λ_{ow}, taper ratio λ and a spanwise trailing-edge kink location ϕ_{kink}. The section between the wing fairing and kink location has fixed zero trailing edge sweep to limit the number of variables.

Table 3.2: Fixed planform parameters during this study

Parameter	Value in this study	Unit
w_{fairing}	2	m
t_{shell}	0.3	m
v_1	0.55	-
v_2	0.99	-

3.2.5. AIRFOIL SHAPE PARAMETERIZATION

Based on the planform described in the previous section, a three-dimensional shape is generated. Figure 3.9 provides an overview of the section shape definition. The cross-sections 1 and 2 are fitted with both leading edge and trailing edge end caps to improve aerodynamic performance. Sections 0,3,4 and 5 are build from CST-defined airfoils, which are treated later in this section. Furthermore, sections 3 to 5 have independently defined twist angles, ϵ. These angles are computed at the semi-chord position. A negative twist angle implies a nose down airfoil orientation with reference to the center airfoil chordline.

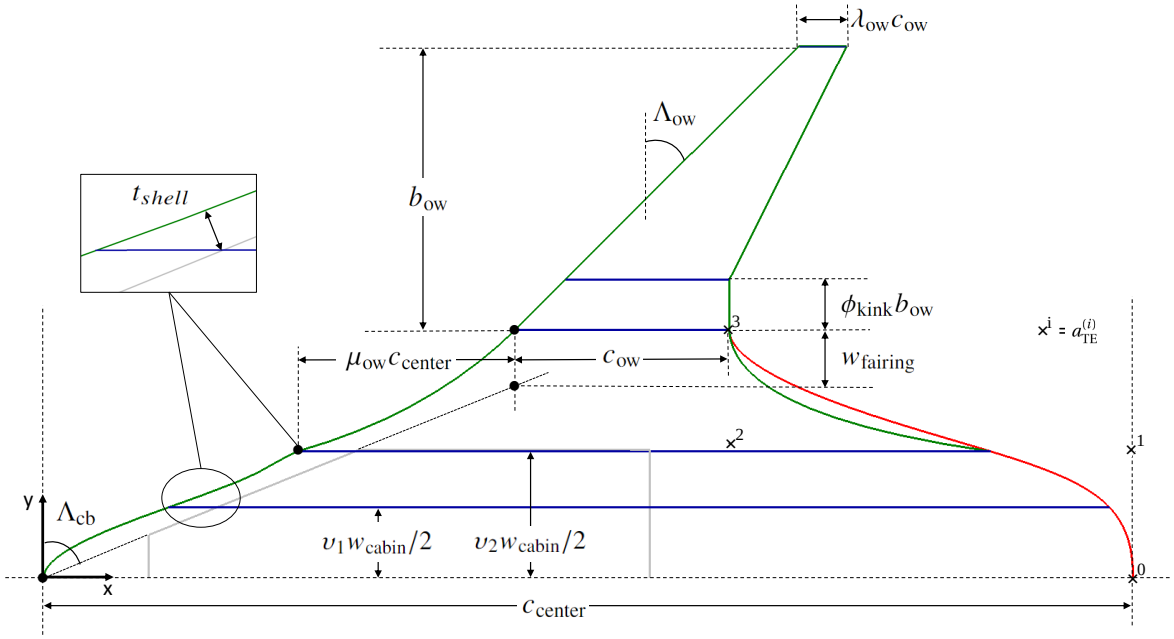

Figure 3.8: Parameterization of the LH2BWB planform layout. The resulting planform outline is shown in green, while the intended trailing edge outline is red. The positioned spanwise sections are shown in blue.

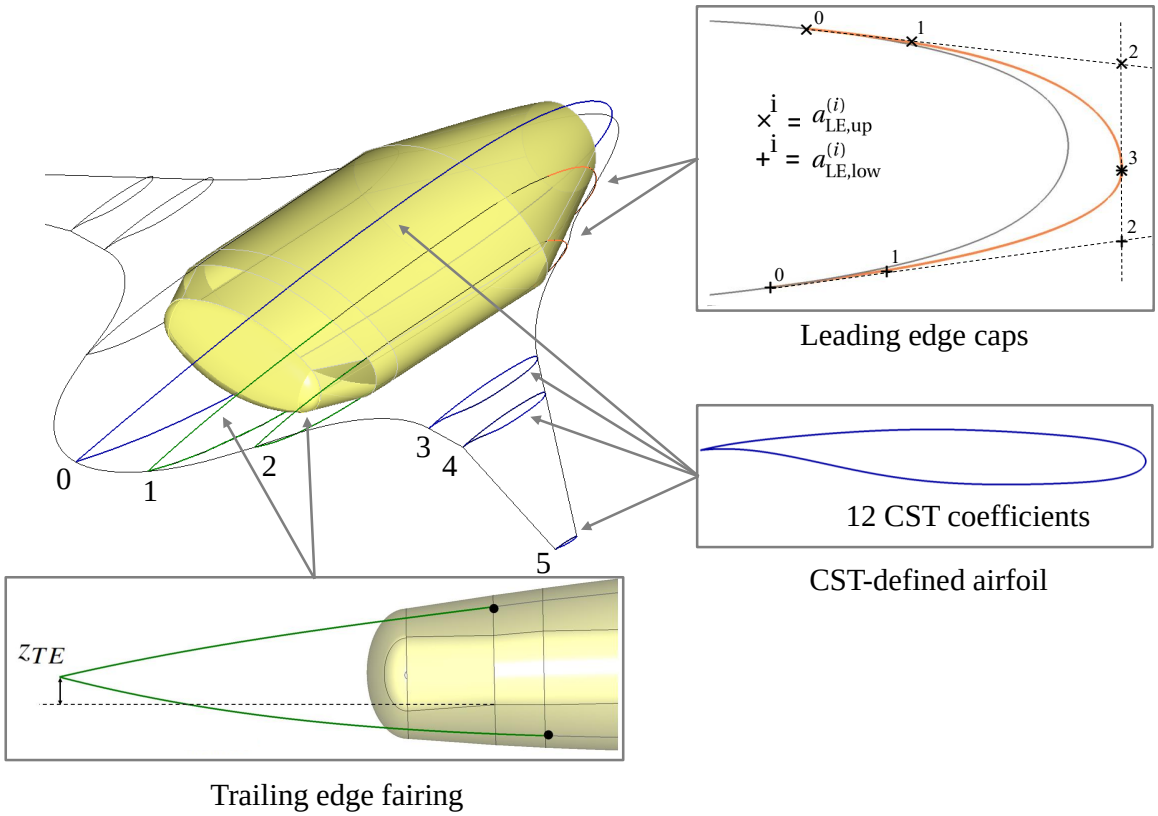

Figure 3.9: Parameterization of the sections for the LH2BWB concept

LEADING EDGE CAPS

The leading edge caps and trailing edge outline are formed by Bézier curves. Such curves are described by using control points $a^{(i)}$ and Bernstein polynomials $b_{i,n}(u)$ as can be seen in this equation [37]:

$$\mathscr{B}(u) = \sum_{i=0}^{n} a^{(i)} b_{i,n}(u) \tag{3.3}$$

Also optional weights w_i can be used for each control point to alter the shape of the Bézier curve. For each value of the variable u between 0 and 1, a point along the curve is present. It should be noted that control of the curve is not local but global. When one changes one control point or weight, this impacts the entire curve. The degree of the curve is equal to the number of control points minus one [37].

Two separate Bézier curves are used for the upper and lower side of the caps. In this parameterization, $a^{(i)}_{\text{LE,up}}$ and $a^{(i)}_{\text{LE,low}}$ denote the control points for these upper and lower sides respectively. The 8 control points used in the leading edge cap parameterization assure first-order continuity at the leading edge and the attachment point to the pressure shell by their positioning. This method is derived from the work by Brown and Vos [56]. For both upper and lower cap, $a^{(1)}$ is placed at 1/3 of the cap length. The leading edge endpoints of the upper and lower curves are placed at a fixed distance from the swept part of the front cabin pressure shell This distance follows from the front cabin sweep angle and shell thickness as can be seen in the planform layout. This method is chosen to account for design flexibility while doors in this part of the cabin are still feasible. Varying the weights $w_{\text{up},i}$ and $w_{\text{low},i}$ of the control points allows the leading edge shape to deform. In this study, only the weights of control points 1 and 2 are allowed to vary to maintain variable efficiency. The actual leading edge z-location is fixed at half of the cabin height. The attachment point for section 2 is placed at the cabin sidewall. The leading edge cap of section 1 starts, in the x-direction, halfway the front cabin shell. It was found this provided a more stable parameterization, which is preferable in optimization studies.

TRAILING EDGE CAPS

The trailing edge caps follow a polynomial method that is described by Hillen [54]. The upper and lower curves of the cap pass through specified start and endpoints while providing second-order continuity at the attachment point. The fourth-order polynomial defining the curve is solved by using four boundary conditions, which lead to the following four equations:

$$x_{end}^3 a_1 + x_{end}^2 a_2 + x_{end} a_3 + a_4 = z_{end} - c x_{end}^4 \tag{3.4}$$

$$x_{start}^3 a_1 + x_{start}^2 a_2 + x_{start} a_3 + a_4 = z_{start} - c x_{start}^4 \tag{3.5}$$

$$3x_{start}^2 a_1 + 2x_{start} a_2 + a_3 = \frac{dz}{dx}(x_{start}) - 4c x_{start}^3 \tag{3.6}$$

$$6x_{start} a_1 + a_2 = \frac{d^2 z}{dx^2}(x_{start}) - 12c x_{start} \tag{3.7}$$

The endpoint is derived from the trailing edge outline at the considered section. The shape of both the upper and lower curve can be influenced by the parameter c. However, in this study c is set to 0 for robustness. Varying this parameter is experienced to yield intersecting upper and lower curves in some cases and hence is less suitable for optimization. Besides the trailing edge x-location, the trailing edge height, z_{TE}, is the only remaining variable for the trailing edge cap shape.

The lower curve of the trailing edge cap starts at the x-position of the most aft cabin oval. The upper curve starts at the longitudinal position of the LH2 tank front oval.

Using the cross-sections of the shell containing the passenger cabin and fuel tank, causes sharp edges to occur at transitions between internal volumes. The sharp corners in the streamwise direction are highly unfavorable in the flow field and are therefore smoothened by replacing such sections with a smooth interpolation between points. The inconsistency this causes is assessed in Chapter 4.

AIRFOIL SHAPE DEFINITION

To define the shape of an airfoil, one seeks a method that can define a wide range of shapes with a limited amount of variables. Examples of such methods are Bézier curves, B-splines and the class function/ shape function transformation technique (CST) [37]. Masters et al. [60] assessed the minimal amount of variables required for each method to approximate predefined airfoil geometries within a specific tolerance. The CST method was found to outperform the other available methods. Hence this method is deemed to be the most suitable for use in the parameterization of the airfoil shapes.

The CST geometry representation method was developed by Kulfan specifically for airfoil parameterization [6, 61]. A list of requirements for the representation of aerodynamic bodies was compiled which included general characteristics such as efficiency, robustness and effectiveness but also included being able to influence key design parameters of an airfoil directly. The resulting representation can be found in the following

equation, with $\psi = x/c$ and $\zeta = z/c$:

$$\zeta(\psi) = C_{N2}^{N1}(\psi)S(\psi) \tag{3.8}$$

The shape is determined by the product of a class function $C(\psi)$ and a shape function $S(\psi)$ [6]. The class function determines the basic shape of the and is defined by:

$$C_{N2}^{N1}(\psi) = (\psi)^{N1}[1-\psi]^{N2} \tag{3.9}$$

To represent an airfoil with a round nose and a sharp trailing edge, $N1$=0.5 and N_2=1 [6].

The shape function is used to control the basic shape of the airfoil, which is defined by the class function. In the same way, also basic features such as maximum thickness and location can be defined. To be able to cover a wide range of airfoil shapes, the Bernstein polynomials are used as shape function in this study:

$$b_{i,n}(u) = \binom{n}{i} u^i (1-u)^{n-i} \tag{3.10}$$

In this equation, n represents the order of the Bernstein polynomial. In Figure 3.10 [6] the influence of the individual terms along the chord can be examined for a third-order Bernstein polynomial. Each individual term of this polynomial can be scaled with a coefficient A_i:

$$S(\psi) = \sum_{i=1}^{n} A_i b_i(\psi) \tag{3.11}$$

Changing one of the coefficients influences the entire shape and hence local control is not possible.

Kulfan and Bussoletti [61] demonstrate that a Bernstein polynomial of order 2 can already approximate a symmetrical NACA airfoil within a defined wind tunnel tolerance. This means 6 parameters are required to describe the airfoil accurately. For this study, 12 parameters are chosen for airfoil parameterization: 6 for the upper side and 6 for the lower side. This number is able to approximate 65% of a wide range of airfoils within a tolerance specified by Kulfan [60]. Variable efficiency is a more important factor in the optimization than being able to specify every airfoil to the slightest detail. Hence the number of 12 parameters is deemed to provide a balance between efficiency and accuracy. While sections 3 and 4 in Figure 3.9 have identical airfoil shapes, the center section 0 and the tip section 5 have separate definitions.

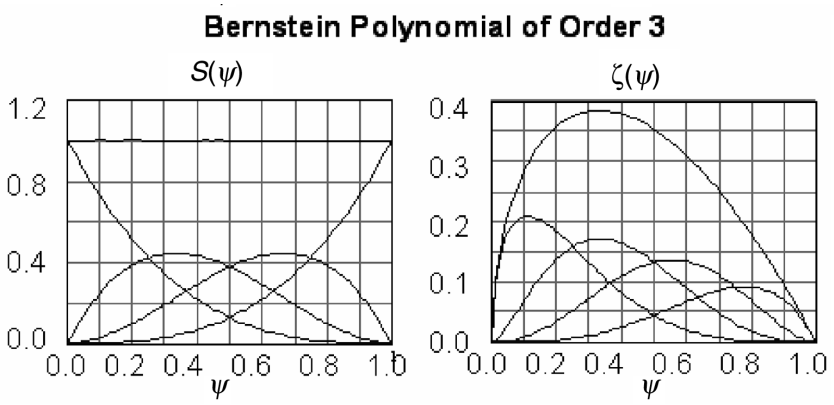

Figure 3.10: The effect of individual terms of the Bernstein polynomial along the chord [6]

SECTION LOFTING PROCESS

The spanwise lofting of the sections is performed separately for the three components as defined in Figure 3.2:

- For the centerbody, sections 0 to 2 and their mirrored counterparts are used
- The wing fairing is based on sections 2 and 3
- The outer wing is based on sections 3 to 5

The outer wing shape is based on a linear loft, whereas the centerbody and wing fairing use nonlinear surfaces to provide smooth transitions. Lofting is a process within *ParaPy* that allows a surface to pass through multiple defined sections. The resulting shape of the surface in this study is found to mainly depend on the number of sections and the section positioning. The behavior of the surface between the sections hence can be controlled up to a limited level. To obtain a satisfactory shape, the centerbody is lofted over extra sections that are positioned at the transitions between the centerbody and wing fairing. Despite this measure, these transitions only have zeroth-order continuity. Since this is mainly in the streamwise direction, effects on the flowfield are limited as shown in Chapter 5. Also, the wing fairing is lofted over an extra section at the transition between the fairing and the outer wing. This transition is almost tangent. The inability to fully control the nonlinear surface lofts causes inconsistencies between the pressure shell and the OML of the aircraft. Since this study focuses on the aerodynamic design and not the structural implementation, the amount of consistency achieved is deemed to be sufficient. The smoothness of the model is more important for this work. The same explanation applies to the bubble shape on the leading edge of the centerbody, which is an undesired phenomenon caused by the lofting. It is looked closer upon in the aerodynamic results chapter.

3.3. AERODYNAMIC DESIGN AND OPTIMIZATION METHOD

This study seeks to find the optimal aerodynamic shape subject to a set of constraints. To reach this optimum, an optimization framework is in place. This framework will be treated first in this section. The evolutionary optimization algorithm which is part of the framework is treated subsequently.

3.3.1. OPTIMIZATION FRAMEWORK

As can be seen in Figure 3.11, the followed optimization strategy compromises two different routes that both yield an optimal design. The baseline design is used as initial input for both methods. The single step optimization design vector consists of both planform and shape variables. On the other hand, in the dual step optimization first a planform optimization is performed. Based on the resulting design, a 3D shape optimization is run. The latter focuses on the 2D airfoil sections. Such a multi step design method has been performed earlier by Meheut et al. [62]. In this study on the LH2BWB, a multi step method allows for comparison between optimum shapes attained in different manners and can therefore provide more insight into the outcome of the research.

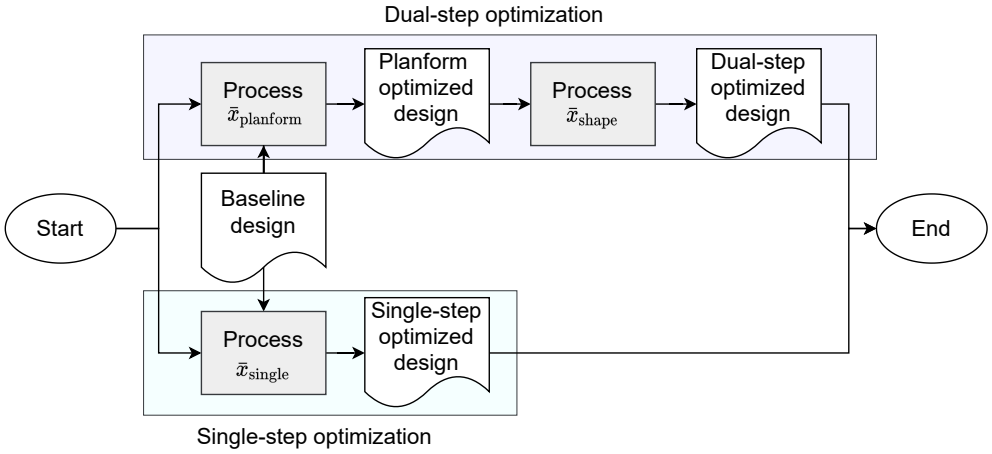

Figure 3.11: Flowchart for the establishment of different optimized designs

The process of modifying the design vector is presented in Figure 3.12. Aerodynamic analysis methods present in this figure will be elaborated upon in Section 3.4 The chosen aerodynamic analysis methods and optimization algorithm induce a considerable computational load. Zingg et al. [63] therefore suggest using the genetic algorithm in combination with low-fidelity methods. This principle is integrated into the form of using a low-fidelity filter before any computationally expensive calculations are performed. Also, the applied geometric constraints are evaluated before any advanced analysis takes place. The objective function encompasses the minimization of the sum of the inviscid and viscous drag and hence both are calculated for each filtered design iteration.

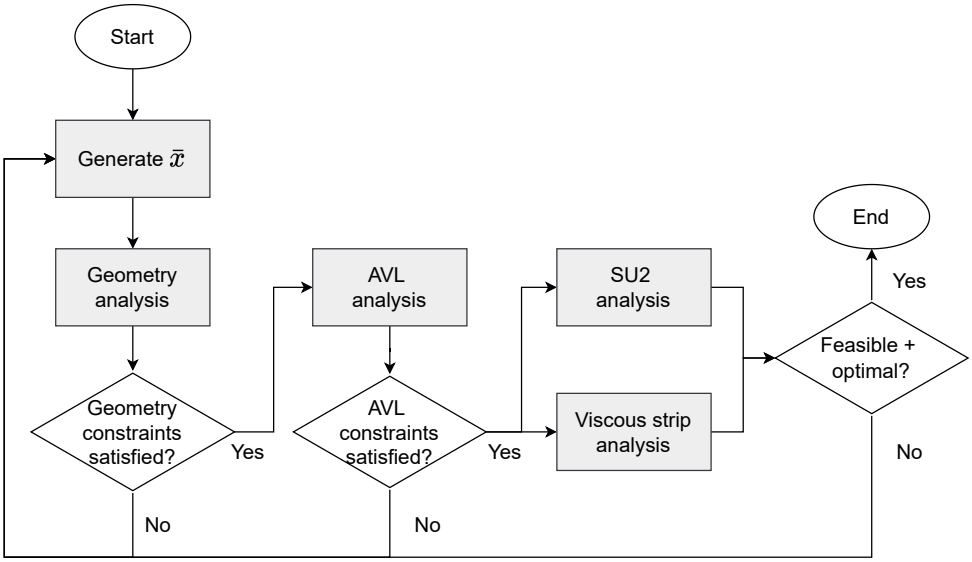

Figure 3.12: Flowchart of the optimization process

The shape is deemed to be at an optimum when the aerodynamic efficiency, L/D, during cruise conditions is at its highest. To allow this objective to be feasible for optimization algorithms, it is written in the negative null form:

$$\begin{aligned} &\text{minimize} && -C_L/C_D(\bar{x}) \\ &\text{subject to} && g_j(\bar{x}) \leq 0 \quad j = 1..., m \\ & && x \in X \subseteq R^n \end{aligned} \tag{3.12}$$

Each optimization requires an initial design vector, $\bar{x}_0$ consisting of n design variables. Bounds are used to limit the values between which the design variable can vary. The parameter bounds define a set constraint X which is a subset of the total design space R^n. The bounds are set such that a robust geometry is present to enable stable optimization. The specific design choices for the baseline design are elaborated upon in Chapter 5. The inequality constraints are denoted by g_j, where j is the constraint number and m denotes the total amount of constraints.

3.3.2. OPTIMIZATION ALGORITHM

The optimization algorithm used in this study is the Differential Evolution (DE) algorithm by Storn and Price [64]. This is a zeroth-order heuristic technique and can be listed under the evolutionary algorithms (EA). Although these algorithms typically need more function evaluations than a gradient-based method, they are able to find the global minimum of the objective function in a robust manner [65]. The robustness partly stems from the absence of a need for gradient information. This gradient information is necessary however to verify one is at the absolute minimum value of the local or potentially global optimum [66]. This study focuses on shape and pressure field features and hence finding the absolute optimum value is not of primary importance. A *Python* implementation of the algorithm which also allows parallel computing is provided within *SciPy*.

Shortly, the algorithm starts with a population of designs from which the best performing individual in terms of the objective function is selected. The design vector (chromosomes) of this individual is combined with the vector of other designs, yielding a new generation. Again the best performing design is selected and this process continues for multiple generations. The result of the optimization follows from the best-performing individual that has been computed among all generations. Multiple parameters can be adjusted to influence design space and convergence rate. A more detailed description of this process is given below:

INITIATION

The algorithm works with populations P_G of design vectors $\bar{x}_{i,G}$. In these equations, G stands for generation and i indicates the specific vector in that generation. The design vector itself consists of n variables. The

population has a size *NP* and its initial generation P_0 is generated using Latin Hypercube Sampling (LHS):

$$P_G = [\bar{x}_{0,G}, \bar{x}_{1,G}, ..., \bar{x}_{NP-1,G}] \tag{3.13}$$

$$\bar{x} = [x_0, x_1, x_j ...., x_n] \tag{3.14}$$

MUTATION

To attain the optimum design vector, trial vectors are created. First, a mutant vector $\bar{v}$ is created according to:

$$\bar{v}_{G+1} = \bar{x}_{best,G} + F \cdot (\bar{x}_{r1,G} - \bar{x}_{r2,G}) \tag{3.15}$$

When using the 'best1bin' strategy, the best performing design vector $\bar{x}_{best}$ is mixed with two random design vectors, $\bar{x}_{r1}$ and $\bar{x}_{r2}$, of the previous generation. The mutation constant F, which must be between 0 and 2, can be either a fixed or a varying value. The latter is called dithering and can speed up convergence [57]. A high mutation constant increases the search space.

CROSSOVER

The trial vector $\bar{u}$ is created by combining design variable values of the mutant and reference vectors:

$$u_j = \begin{cases} v_j & \text{for randbin}(j) \leq C \quad \text{or} \quad \text{if } u_j = u_n \\ (x_{i,G})_j & \text{for randbin}(j) > C \end{cases} \tag{3.16}$$

For each design variable j a value is generated from a binomial distribution on $[0, 1]$. If this value is less than or equal to the crossover constant C, the parameter value from the mutant vector $\bar{v}$ is used. Otherwise, the variable value from the original vector is used. A high crossover constant hence increases the search area. The last variable of each trial vector stems from the mutant vector to increase diversity.

SELECTION

If the trial vector outperforms the original best vector, the trial vector is used in the new population P_{G+1}. Otherwise the original vector is used. When the algorithm is used in a parallel manner, the best vector gets updated every generation.

CONSTRAINTS

Constraints on the optimization problem are implemented by assigning very low performance values to designs that violate them. This means infeasible trial vectors will always be rejected when compared to a feasible design in the selection step of the algorithm. This way of constraint handling is also known as the death penalty method [67]. Since the algorithm tends to minimize the objective function, penalties are assigned large values. The method is straightforward to implement:

$$f(\bar{x}) = \begin{cases} \text{fun}(\bar{x}) & \text{if feasible} \\ \text{penalty} & \text{if infeasible} \end{cases} \tag{3.17}$$

If a design is found to be infeasible only after its evaluation in SU2, a lower penalty is assigned. Hence, if in the selection phase two infeasible designs are compared, the algorithm prefers the design that is closer to the feasible design space .

3.4. AERODYNAMIC ANALYSIS METHODS

The optimization methodology requires a suitable drag estimation method. The resulting optimization designs should be close to the aircraft geometries that would perform best in physical flow conditions. On the other hand, the computational effort involved in each design evaluation should be limited to enable a feasible optimization. Three different aerodynamic analysis methods were used in this study. All of these are elaborated upon in this section. Firstly, AVL is treated which is used as a low fidelity filter as explained in Section 3.3. Secondly, the Euler solver and its setup are discussed. This solver is used to compute the inviscid drag coefficient, $C_{D\text{inv}}$. The viscous drag coefficient $C_{D\text{visc}}$ is estimated by an empirical strip method, which is described in Section 3.4.3. Finally, Section 3.4.4 elaborates on the neutral point calculation method.

The viscous and inviscid drag components are computed separately by the use of different methods. These are later joined by the following equation to yield the objective function value:

$$\frac{C_L}{C_D} = \frac{C_L}{C_{D\text{inv}} + C_{D\text{visc}}} \tag{3.18}$$

3.4.1. ATHENA VORTEX LATTICE

In this study, AVL is mainly used for filtering purposes. Hence, the angle of attack and pitching moment computations are of main interest. AVL is a Vortex VLM and assumes an inviscid and irrotational flow. Also, it neglects thickness and thereby reduces the wing to a cambered surface. In literature, Li et al. [50] use a VLM as part of a low fidelity method in a design space reduction. To estimate the pitching moment as close as possible, two AVL runs are performed. The first one serves to compute the neutral point of the design. The second run uses this neutral point to compute the center of gravity around which the pitching moment is calculated. Also, the design cruise lift coefficient is based partially on the induced drag computed by AVL. A cambered surface that is linearly interpolated between the camber lines of the airfoils (sections 0 to 5 in Figure 3.9) serves as an input for this method. This input differs from the actual geometry substantially. However, if sufficient margins are taken, it serves its purpose of filtering out infeasible designs well.

3.4.2. COMPUTATIONAL FLUID DYNAMICS ANALYSIS

The CFD analysis software used for the computations is *Stanford University Unstructured* (SU2). It is an open-source package developed to solve the partial differential equations (PDE's). Due to the readily available coupling with the *ParaPy* software, this is deemed a suitable suite. In this study, the Euler equations are used to estimate the inviscid drag, lift and pitching moment coefficients. When applying the nomenclature provided in Figure 2.2 the inviscid drag includes the wave and induced drag. Chapter 2 describes why this solver provides a balance between computational effort and accuracy. Also, the shortcomings of the Euler method are treated in that chapter. The Reynolds numbers on the LH2BWB aircraft are relatively high, especially on the centerbody. This could mean that not including boundary layer effects has a limited impact on the results. Furthermore, the curvatures are more pronounced due to the absence of boundary layer displacement thickness. Hence, the supervelocities predicted by the Euler solver will be higher than in reality [48]. This implies the Euler solver most likely over-predicts the presence of shock waves and associated wave drag.

Regarding numerical schemes, both an upwind and central difference scheme are tested for suitability in the verification chapter. These numerical schemes are used in the discretization of convective fluxes. Both the Jameson-Schmidt-Turkel (JST) and Roe schemes are applied. The JST scheme is a second-order method, while the Roe scheme is a first-order method [47].

The remainder of this section elaborates on the setup of the solver in terms of the computational mesh and domain respectively.

GRID GENERATION

The SU2 aerodynamic solver requires a computational grid as an input. The main aspects of such a grid are the type, topology, and the number of volume elements. The grid used in this study is of the unstructured type. The connections between cells are less straightforward than for a structured mesh, which has a more regular discretization. Therefore an unstructured mesh is computationally more inefficient to solve [47]. Since the geometry constantly changes in this study, a highly automated type of meshing is required. An unstructured grid provides the capability to discretize a complex domain in a fairly reliable manner and hence is most suitable.

The grid is generated using the *Salome* meshing software[2]. Its integration into *ParaPy* and robust working makes this package suitable for aerodynamic optimization studies. The meshing process works by connecting the nodes defined on the model edges, forming segments. Thereafter, the surface and volume are filled based on these segments. This is a bottom-up approach. The mesh topology and fineness can be influenced using six parameters:

- Number of nodes per unit length on model edges
- Maximum 2D cell size, defined separately for the model and the outer domain
- Maximum 3D cell size
- Maximum cell growth rate, defined separately in 2D and 3D

Since the study only considers Euler computations, a structured discretization of the boundary layer is not necessary. The 3D mesh consists of tetrahedrons which leads to triangular shapes on surfaces. This can be seen in Figure 3.13a, where an example of a very coarse mesh on the aircraft model is provided. The size of the cells grows gradually when moving further away from the aircraft model. The amount of volumes used to generate results is based on the grid convergence study in Section 4.3.

[2] www.salome-platform.org

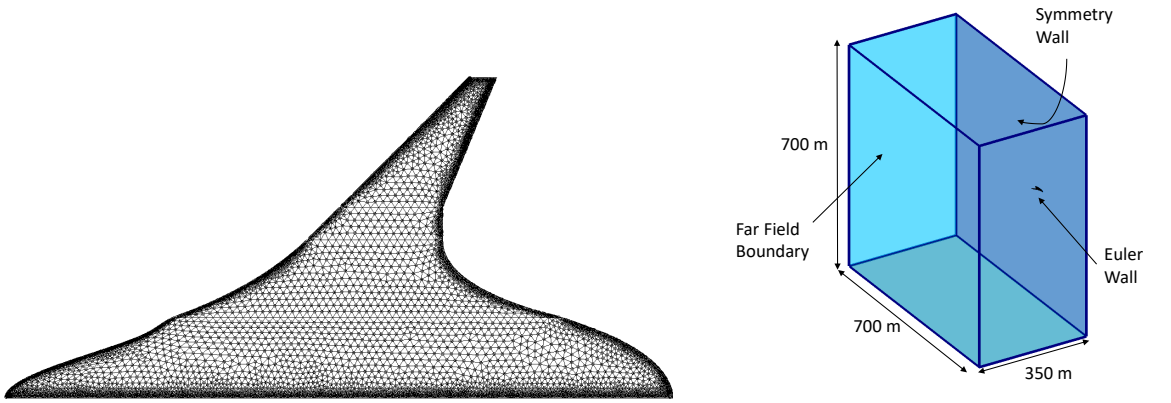

(a) Example of a coarse unstructured surface mesh on the LH2BWB geometry

(b) The computational domain used for SU2 calculations

Figure 3.13: Mesh example and computational domain used for CFD calculations

COMPUTATIONAL DOMAIN

The computational domain used for the SU2 simulations consists of a parallelepiped, with half of the LH2BWB model attached at one side. It is shown in Figure 3.13b, where also the following boundary conditions are indicated:

- Symmetry: since the LH2BWB model is symmetric, half of it can be omitted using the symmetry condition. This in turn reduces computational effort.
- Euler boundary: the flow cannot penetrate the wing, which is a physical barrier.
- Far-field: the flow can pass through these walls

The domain size used in this study has the following dimensions in terms of aircraft body lengths:

- 7 in front of to the aircraft model
- 13 behind the aircraft model
- 10 below, above and aside of the aircraft model

The body length applied for this is 35 m. These values were chosen by scaling the settings in the study by Qin and Siouris [38], which considers a larger BWB in the transonic domain. To gain further confidence in the domain size, the result of the objective function is compared to the outcome of a domain that is 50% larger in every direction. This yields a domain with 337.5 % of the volume of the chosen domain size. This resulted in a 0.7% difference in the estimated inviscid drag coefficient between the two domain sizes. Further shrinking down the domain does not bring major benefits, since in an unstructured grid the volume of the outer cells is relatively large. Hence they make up a small percentage of the total amount of cells and computational effort.

3.4.3. VISCOUS DRAG ESTIMATION

The viscous drag component can form a substantial part of the total drag. Since it is omitted in the Euler computations, a different method is used to estimate this viscous part. Since the coupling of the boundary layer equations is deemed to be beyond the scope of this project, empirical relations from literature are used. As is shown in Section 4.4, this gives satisfactory results with the chosen numerical method.
The empirical method works by combining flow characteristics with model shape properties to attain the zero-lift drag. The following equation [68] provides this combination with the skin friction coefficient, C_F and the form factor, FF , respectively:

$$C_{D_{\text{visc}}} = C_F \cdot FF \cdot \frac{S_{\text{wet}}}{S_{\text{ref}}} \tag{3.19}$$

For the flat-plate skin friction approximation, separate equations are available for a laminar and turbulent boundary layer. In this work an equation by Raymer[69] is used:

$$C_{F,\text{turb}} = \frac{0.455}{(\log_{10} Re)^{2.58}(1+0.144M^2)^{0.65}} \tag{3.20}$$

This equation is based on turbulent boundary layer flow, which is applicable on the LH2BWB given its cruise speed and chord lengths.

For the form factor, multiple equations are available. However, for an airfoil with 12% thickness, the resulting form factors differ less than 10% [68]. The form factor used in this study follows from Torenbeek [45] and allowed for a stable implementation into the aerodynamic analysis module with the geometry at hand:

$$FF = 1 + \left(2.7\frac{t}{c} + 100\left(\frac{t}{c}\right)^4\right)\cos^2(\Lambda_{0.5}) \tag{3.21}$$

To apply this method to the LH2BWB geometry, its semi-model is discretized into 10 streamwise strips. For each of these strips, the form factor, wetted area S_{wet} and the local C_F is computed. By summing the contribution of each strip and dividing by the total reference area, the zero-lift drag coefficient for the entire aircraft is computed.

3.4.4. PITCHING MOMENT COEFFICIENT COMPUTATION

Imposing bounds on the pitching moment to limit trim drag is found to be a driver in aerodynamic shape design, as explained in Chapter 2. Therefore, the aerodynamic moment requires evaluation in a sufficiently detailed manner. The center of gravity location directly influences the pitching moment. It is placed such that each design is longitudinally stable. In the early stages of designing, the center of gravity position can still be influenced [39] and therefore this solution seemed fitting. Firstly, the neutral point position is determined by using this equation:

$$x_{\text{NP}} = x_{\text{ref}} - c_{\text{ref}} \cdot \frac{dC_m/d\alpha}{dC_L/d\alpha} \tag{3.22}$$

Where the reference chord follows from the *ParaPy* implementation from Hillen [54] according to:

$$c_{\text{ref}} = \frac{2}{S}\int_0^b c^2(y)dy \tag{3.23}$$

The derivatives follow from SU2 computed values. Two lift conditions serve as input: one at the design C_L = 0.2 and one at C_L = 0.19. The delta in angle of attack yielded by these lift coefficients was examined to provide an accurate estimation of the local derivatives around the cruise point. As can be seen in Section 4.2, numerical error present in the Euler computations is believed not to have an impact on these calculations. Subsequently, the center of gravity is positioned in front of the neutral point with a static margin of 2% of the MAC. A margin of 1% MAC corresponds to the minimum absolute distance seen in conventional aircraft of comparable size. Hence the extra buffer leads to a reference position within the aft half of the center of gravity range. AVL provides the neutral point as output by itself, using the same equation.

4

VERIFICATION AND VALIDATION

This section presents the verification and validation of parameterization and analysis methods. Firstly, the parameterized outer shell is compared on consistency to the cabin pressure shell in Section 4.1. Secondly, the method for calculating the aerodynamic derivatives used in the neutral point computation is elaborated upon. Thirdly, a grid convergence study on the LH2BWB concept is provided in Section 4.3. Finally, in Section 4.4 a reference case is used for solver validation.

For a mesh quality assessment, one can refer to the work by Faggiano and Vos [55] where the *Salome* meshing package and the *ParaPy* software have been applied similarly.

4.1. GEOMETRY VERIFICATION

The parameterization procedure follows an inside-out approach. This approach starts with cabin shell generation. To verify the outer shell is consistent with the oval cabin structure, the geometry is examined qualitatively. Figure 4.1 presents the consistency of the cabin pressure shell compared to the outer mold line. In general, the consistency is deemed satisfactory. The largest deviation is found at the transition section between the front and aft cabin. Figure 4.2 provides a cross-section in the yz plane for both shells at this transition. The figure shows that on a more outboard part, the shells are slightly inconsistent. This is caused by the smoothing that is applied to the cross-section to remove sharp edges in the streamwise direction. Another contribution to this inconsistency is the lofting process. This process can only be controlled up to a limited degree as explained in Section 3.2. In Chapter 5 a closer look is taken at the consequences for the pressure distribution of this and other geometric imperfections.

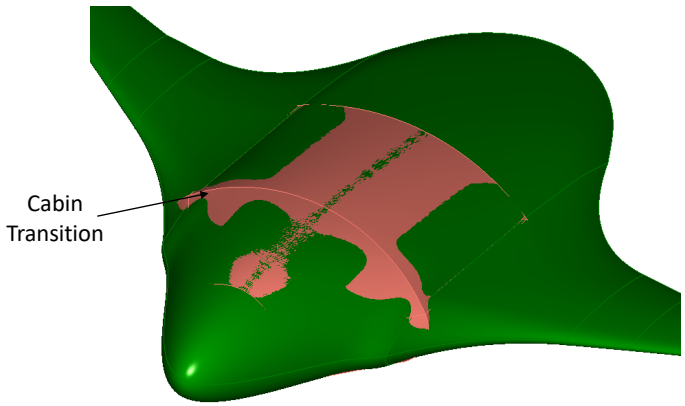

Figure 4.1: Consistency of the green outer shell with the orange passenger cabin pressure shell

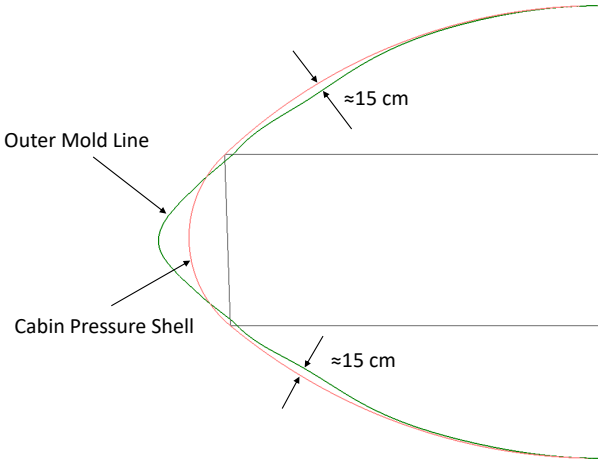

Figure 4.2: Consistency of the green outer shell with the orange cabin pressure shell at the transition between the front and the aft cabin of the baseline design

4.2. AERODYNAMIC DERIVATIVE CALCULATION VERIFICATION

The method to calculate the neutral point location mentioned in Section 3.4.4, uses the derivatives of the lift and pitching moment coefficients. To verify the calculated derivatives indeed approximate the local curve slopes to a satisfactory degree, Figure 4.3 is presented. In these plots, the approximated derivatives stemming from datapoints around $C_L = 0.19$ and $C_L = 0.20$ can be compared to the slope for a larger range of angle of attacks. For C_{L_α}, the calculated value yields a curve that passes right through all data points as can be seen in Figure 4.3a. Thus, the chosen parameters provide a satisfactory approximation and are not subject to any major numerical error present in the CFD output. Regarding C_{m_α} in Figure 4.3b, the curve is examined to be non-linear. However, the calculated slope provides a linear curve that is tangent around the eventually chosen cruise C_L. Therefore, the pitching moment derivative is also deemed to be calculated with satisfactory accuracy.

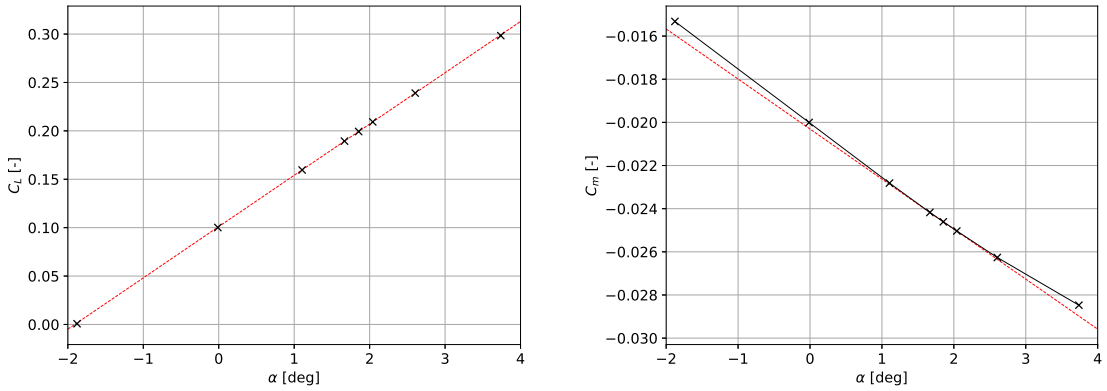

(a) Lift coefficient over angle of attack

(b) Pitching moment coefficient over angle of attack

Figure 4.3: Lift and pitching moment derivative plots. Slopes are fitted for datapoints around $C_L = 0.19$ and $C_L = 0.20$, Mach = 0.78

4.3. GRID CONVERGENCE STUDY

To determine which mesh settings provide a satisfactory result at an efficient computational cost, a grid convergence study is performed. Settings for the unstructured mesh generation are varied such that the mesh gets finer while maintaining the same topology as much as possible. These settings can be found in Appendix B. The results of the grid convergence study for the parameters of interest are displayed in Figure 4.4. Figure 4.4a presents the grid convergence in absolute form. As can be seen, the pitching moment reaches conver-

gence at 1.2 million cells. On the other hand, the inviscid drag coefficient has still not fully converged at the finest mesh tested. Therefore, a curve is fitted to the data points in Figure 4.4a. Figure 4.4b shows the relative error, ϵ_{rel}, compared to the most accurate solution. The relative error for the inviscid drag coefficient is computed as follows:

$$\epsilon_{\text{rel}} = \frac{C_{D_{\text{inv}}} - C^{\text{fine}}_{D_{\text{inv}}}}{C^{\text{fine}}_{D_{\text{inv}}}} \tag{4.1}$$

For the pitching moment, the same approach is applied. The finest solution used for this moment coefficient is at $3.2{\cdot}10^6$ elements. For the drag coefficient, a data point at $6{\cdot}10^6$ elements is retrieved from the fitted curve in the left figure. the optimizations, a mesh containing $1.2{\cdot}10^6$ cells is chosen since it has an acceptable error and limited computation time. This mesh results in an error of 7.2 % for the inviscid drag coefficient and 0.2% for the pitching moment coefficient. Although the inviscid drag is substantially overestimated, it is deemed to be sufficient for the goal of comparing design performance during optimization since all designs are subject to this overestimation due to their similar shapes. Quantitative results in this work are acquired using meshes containing 3.2 million volumes, yielding an error of 1.9 %.

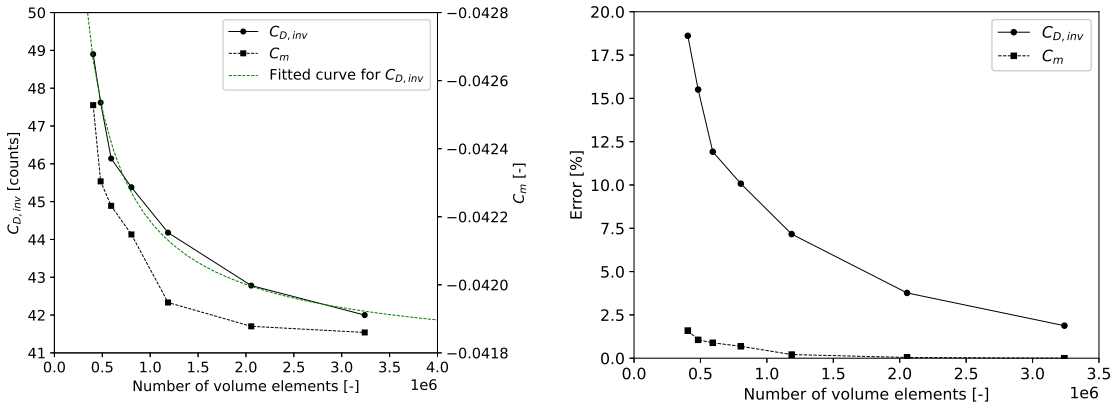

(a) Grid convergence plot for inviscid drag and pitching moment

(b) Relative error for inviscid drag and pitching moment

Figure 4.4: Grid convergence study plots

4.4. AERODYNAMIC SOLVER VALIDATION

The aerodynamic analysis method that is presented in Section 3.4 is validated with the ONERA M6 wing in this section. The validation is performed by using experimental data of the wing. Firstly, the reference object will be elaborated upon. This is followed by a validation using pressure coefficient plots. Lastly, lift over drag data of the analysis method is compared with higher order solver solutions.

4.4.1. ONERA M6 WING

The ONERA M6 wing has served as a validation object for many research projects [70]. The transonic conditions associated with this wing can cause a lambda shock to form on the upper surface. The difficulty of predicting the shape of this lambda shock makes it an often chosen reference object for solvers that are to be used in the transonic domain [71].

The M6 wing was developed by ONERA in the late 1970s. The semi-wing is straight-tapered, swept and does not feature twist. It is displayed in Figure 4.5 [7]. The geometry has the following values: taper ratio = 0.56, aspect ratio = 3.8, quarter-chord sweep angle = 26.7°, span = 1.196 m, MAC = 1.1963 and root chord = 0.8059 m. The ONERA D airfoil at the root results in a streamwise thickness-over-chord ratio of slightly less than 10%. The wind-tunnel data that is used in this work stems from the experiment by Schmitt and Charpin conducted in 1979 [7]. The wing was placed at a 3.06° angle of attack and Mach number of 0.8395, yielding a Reynolds number of $11.72 \cdot 10^6$. Freestream temperature and pressure are at sea-level conditions. Also, the wing is clamped to the wind-tunnel wall.

The unstructured mesh of the ONERA M6 wing used for the Euler computations includes 108,396 nodes

and 582,752 tetrahedral elements. The mesh is provided by the SU2 team[1]. The computational domain features a parallelepiped shape with the semi-wing attached to one of the side walls. This wall uses symmetry boundary conditions while the other domain walls have far-field based conditions. An exception is the wing surface, which has an Euler wall. Thus, the domain setup is identical to the setup used for aerodynamic calculations on the LH2BWB.

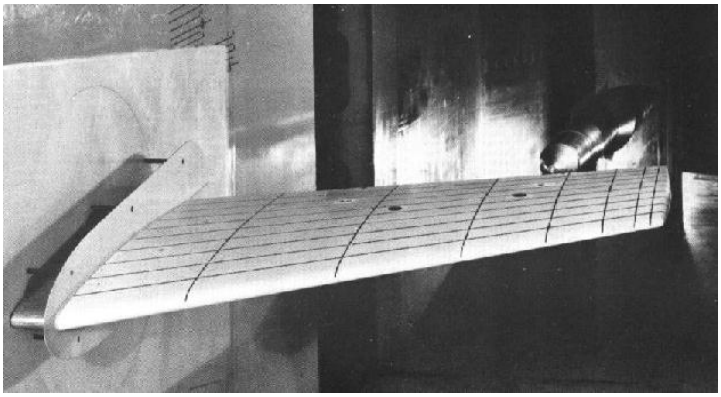

Figure 4.5: The ONERA M6 wing in the experiment by Schmitt and Charpin [7]

4.4.2. SPANWISE PRESSURE DISTRIBUTIONS

Two-dimensional pressure distributions for six spanwise sections on the ONERA M6 wing are presented in Figure 4.6. Three sets of data are present in each plot. The Euler solver is used with both a JST and Roe convective scheme to assess which is most suitable for use in optimization. The experimental data stems from test 2308 by Schmitt and Charpin [7]. The plots provide a comparison of the Euler solver performance in terms of pressure distribution and especially shock location.

In general, the numerical Euler computations match the experimental data to a satisfactory degree. However, the prediction of the shock location and strength varies with spanwise location. The Euler data on the most inboard section in Figure 4.6a shows a stronger shockwave compared to the experimental data. This section is located close to the wind-tunnel wall. The wind-tunnel experimental setup is expected to play a role in the shock strength discrepancy since studies performed using RANS and DES solvers display the same discrepancy with experimental data [70].

For outboard sections, the Euler solver performs satisfactorily. An exception is present at 80% span, see Figure 4.6d. Here a double shock is present in experimental data, which is tied to viscous effects. Hence, the Euler solutions do not predict the first shock. Also, the separation taking place at the trailing edge resembles a viscous effect that is not captured with the Euler solver. The failure to predict this viscous effect should be taken into account when examining the adverse pressure gradients at the trailing edges of the optimization results. Note that Euler results at y/b = 0.99 in Figure 4.6g display a discrepancy in predicting the pressure distribution near the trailing edge. Even high-order solvers using eddy viscosity models cannot reproduce the experimental data due to complex phenomena taking place at the tip [72]. Nevertheless, the Euler solvers are able to predict the pressure distribution for within satisfactory accuracy for the majority of the span.

In general, the Roe scheme predicts the flow field slightly more accurately. However, the JST scheme was able to converge to lower residuals in shorter times. Since this observation is beneficial for optimization, the JST scheme is selected for this study.

[1] https://su2code.github.io, accessed at 17-05-2021

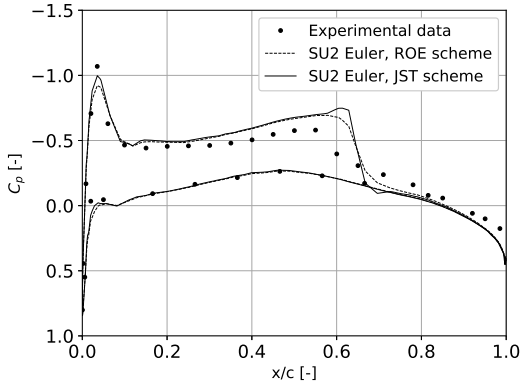

(a) y/b = 0.2

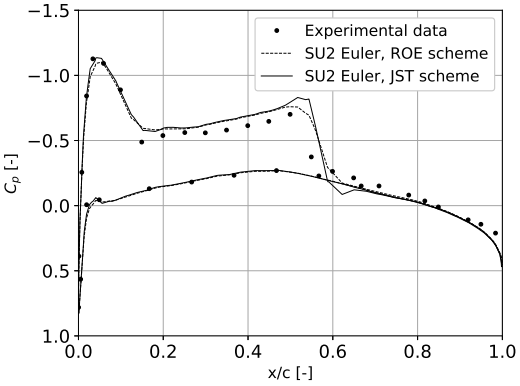

(b) y/b = 0.44

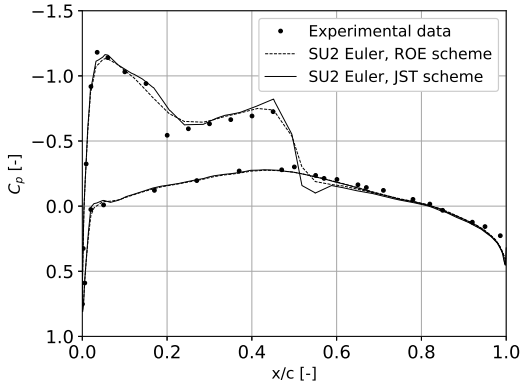

(c) y/b = 0.65

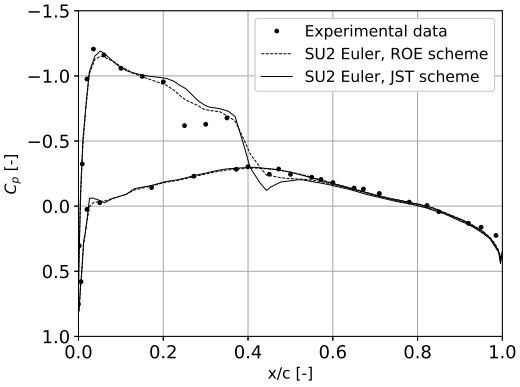

(d) y/b = 0.8

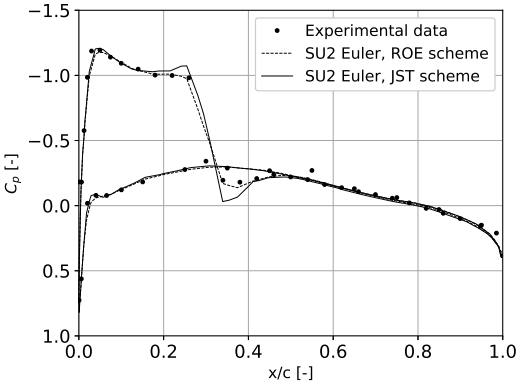

(e) y/b = 0.9

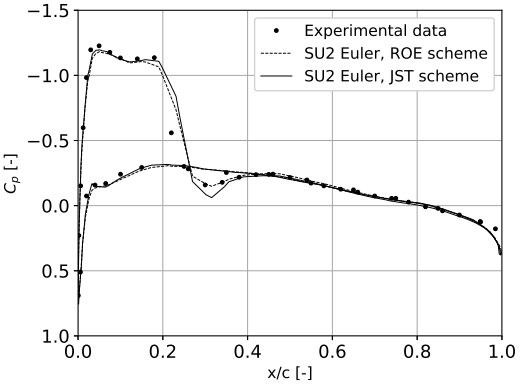

(f) y/b = 0.95

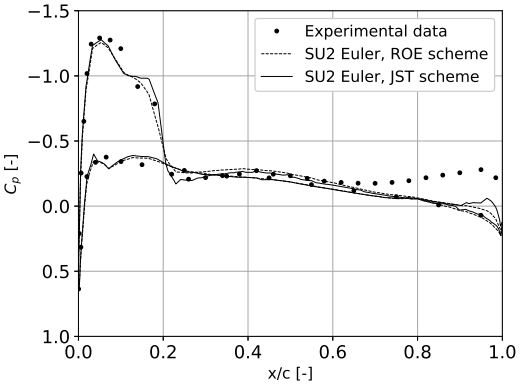

(g) y/b = 0.99

Figure 4.6: C_P distribution of ONERA M6 at various spanwise sections, α = 3.06°, Mach = 0.8395

4.4.3. DRAG POLAR

The previous section has shown that the Euler solver can predict the pressure distribution on a transonic wing within the desired accuracy. However, the objective function in the optimization involves the lift and drag coefficients. To determine whether the solver is able to satisfactory predict the aerodynamic forces, a lift over drag polar is given in Figure 4.7. The data from literature stems from higher order simulations, such as Detached Eddy Simulations performed by Durrani and Qin [70], and also includes data from earlier studies. Experimental data is not present in the plot since this data does not contain values for aerodynamic forces. By taking the total drag coefficient in account, the combination of the Euler solver and the viscous module can be validated. The viscous drag for the ONERA M6 wing is approximated by using the strip method as described in Section 3.4.3. This method is used by applying the form factors from Torenbeek [45] with the ONERA airfoil shapes provided by NASA [73].

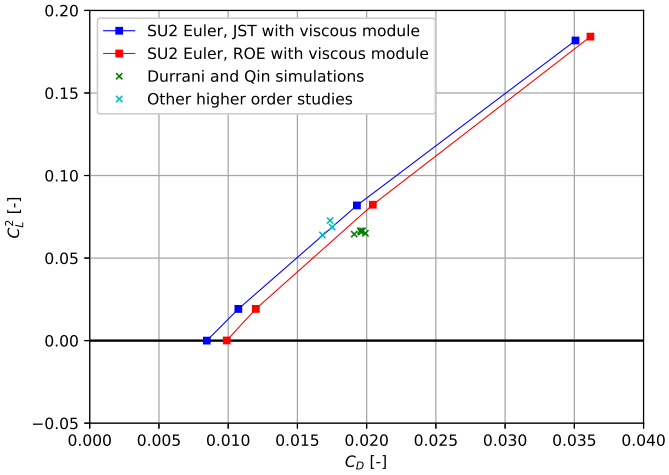

Figure 4.7: Lift over drag polar for the ONERA M6 wing at Mach 0.8395. Higher order data stems from Durrani and Qin [70]

Both the Euler solutions pass through the data points. The Roe scheme is positioned more in between the clusters, while the JST scheme passes right through the datapoints from other higher order studies summarized by Durrani and Qin. Since the latter concerns multiple studies by different authors, the JST scheme is deemed to provide a satisfactory drag estimation. It can be seen there is a small difference in drag coefficient at the zero lift condition between the Roe and JST schemes. The viscous drag estimation is identical for both solutions. Also, the zero lift condition means a absence of lift induced drag. Hence, this difference originates from either wave drag to volume or other inviscid drag sources. Such drag contributions however cannot be distinguished by using Figure 2.2.

The JST scheme provides satisfactory results, is robust and converges quickly. Therefore, it is chosen for the aerodynamic optimization.

5

RESULTS & DISCUSSION

This chapter will both elaborate on the setup used to generate the data and shapes, as well as the results. The experimental setup is provided in Section 5.1. The results are presented and discussed in Section 5.2 and subsequently put into perspective in Section 5.3. All aerodynamic coefficients provided in this chapter follow from a reference area of 450 m^2.

5.1. EXPERIMENTAL SETUP

The setup of the optimization consists of multiple aspects. Firstly, the aerodynamic setup is elaborated upon. The optimization process encompasses a substantial amount of computational effort. Therefore measures to limit this effort as well as the algorithm setup are treated secondly. Thirdly, the geometric and aerodynamic constraints applied during optimization are elaborated upon. Fourthly, the baseline design is presented and discussed. Finally, the setup of each of the optimization cases is treated.

5.1.1. AERODYNAMIC SETUP

The optimization of the LH2BWB is performed for a single flight condition, which is the cruise condition. The cruise Mach number is set to 0.78, equal to the reference aircraft. Atmospheric conditions are based on the ISA conditions at a cruise altitude of 11,000 m. This altitude is slightly higher than the design cruise altitude of the CSR-01 reference aircraft (10,666 m). A summary of these conditions can be found in Table 5.1.

Table 5.1: Flight conditions for LH2BWB aerodynamic optimization at h_{cruise} of 11,000 m

Parameter	Value	Unit
Mach	0.78	-
ρ_{cruise}	0.364	kg/m^3
p_{cruise}	19277	Pa
T_{cruise}	216.6	K
$C_{L_{\text{cruise}}}$	0.2	-

A conceptual study has not yet been performed and hence no weight estimation is available. Therefore a different approach to determine a suitable cruise lift coefficient is used. The fixed lift coefficient at which the optimization takes place is determined by examining a drag polar for the baseline design. This drag polar consists of AVL estimated induced drag and viscous strip data for the viscous drag. It indicates at which lift coefficient, the lift-over-drag ratio will be highest. This is found to be around a C_L of 0.2, based on a S_{ref} of 450 m^2. This value for the reference area is fixed throughout the optimization. Hence, every design provides an equal amount of lift regardless of its actual S_{ref}. This allows for a fair comparison between designs.
The center of gravity location is such that the design is longitudinally stable as described in Section 3.4.4. With the reference chords of the various presented designs, a static margin with an absolute value of around 0.5 m is present.

5.1.2. COMPUTATIONAL SETUP

The optimization is performed with the algorithm that is been described in Section 3.3. The maximum amount of iterations that is performed is set to 20 while the population size is equal to 4 times the amount of design variables present in that optimization. To perform the design evaluations in parallel, the 'deferred' update technique is used. This means the best design vector, upon which mutant vectors are partially based, is updated every generation instead of continuously. This potentially leads to slower convergence but more evaluations are possible since total computation time is lower in parallel computing. For the mutation constant F, dithering is used: its value varies between 0.5 and 1. The cross-over constant C is set to 0.7.

Although a part of the designs are filtered out by constraints, the number of designs that are evaluated with SU2 require substantial computational power. Therefore, multiple measures are taken to keep the computation time within bounds:

- 4 designs are evaluated simultaneously with the use of parallel computing
- An automated coupling has successfully been made with which the locally running optimization algorithm can perform the SU2 Euler calculations on a remote High Performance Computing (HPC) station
- The SU2 solver has a parallel setup by using grid partitioning: the problem is split up into multiple smaller problems which allows multiple cores to work in parallel.
- Following the grid convergence study in Section 4.3, a mesh fineness that provides a balance between accuracy and computational time is chosen
- A maximum of 350 iterations per CFD run is set. This yields objective function values that are within 0.25% of the values present after 600 iterations.

Running the algorithm, generating geometries, running AVL and meshing the designs takes place on a single (local) device. Also, the intermediate calculation of the neutral point following from SU2 results is performed on this device. With an Intel i5 1.6 GHz processor and 8GB memory it takes around 15 minutes to generate a mesh with 4 parallel processes.

The nodes used on the HPC-cluster have 20 cores using the Intel E5 2.5 GHz processor and 6.5 GB memory per core. These cores are used in parallel and lead to a design evaluation time of around 15 minutes. Multiple HPC nodes are used to allow the parallel aerodynamic evaluation of multiple designs. In total, each design evaluation takes around 35 minutes to be completed in the parallel setup. This time also takes into account geometry and AVL evaluations.

5.1.3. CONSTRAINTS

The optimization constraints present in this study serve the purpose of generating aerodynamic shapes that comply with certain aerodynamic and geometric requirements. Each of these constraints will be treated separately below.

TOTAL WINGSPAN

The wingspan is not allowed to exceed 36 meters:

$$g_1 = b_{\text{total}} - 36\text{m} \leq 0 \tag{5.1}$$

This value is based on gate class C of the ICAO Annex 14 - Aerodrome Reference Code, in which the reference aircraft fits. From a conceptual point of view, this allows the aircraft to be compatible with the same airports as its conventional counterparts.

OUTER WING THICKNESS

Although this is not a multidisciplinary study, the outcome of the optimization should not be structurally infeasible. Therefore thickness-to-chord ratio constraints are present for sections 3 and 5 Determination of the t/c value takes place perpendicularly to the local semi-chord sweep angle since this is also approximately in the direction of the wingbox. First, the semi-chord sweep angles for both parts of the outer wing are computed. The streamwise chordlenghts of sections 3 and 5 are multiplied with the cosine of these sweep angles. Finally, the maximum absolute thickness of sections 3 and 5 is divided by the calculated chordlengths. Values are set at a 12% and 10% thickness over chord ratio for the root and tip chords respectively:

$$g_2 = 0.12 - (t/c)_3 \leq 0 \tag{5.2}$$

$$g_3 = 0.10 - (t/c)_5 \leq 0 \tag{5.3}$$

CENTERBODY THICKNESS

The centerbody is required to house all the internal volumes. Multiple constraints are in place to ensure this. Firstly, the keel height at the aft of the cabin should be at least 1.16 m to provide sufficient height for an LD3-45 cargo container:

$$g_4 = 1.16m - h_{3,\text{aftcabin}} \leq 0 \tag{5.4}$$

Secondly, the liquid hydrogen tank front oval radii should not be lower than a minimum value to avoid heavy structures resulting from large in-plane stresses. For both the crown and keel arc this value is set to 10 m:

$$g_5 = r_{\text{tankoval,front}} - 10m \leq 0 \tag{5.5}$$

Thirdly, the aft tank oval has minimum arc radii of 8 m. This applies for both the crown and keel arc since they are equal due to the parameterization:

$$g_6 = r_{\text{tankoval,aft}} - 8m \leq 0 \tag{5.6}$$

The arc radii limit values are based upon earlier research using the oval fuselage concept [52, 55]. Further research has to verify whether these values do not induce high structural weights. Constraints on the minimum thickness on a forward part of the airfoil are not present. The typical shape of used centerbody airfoils has its thickest point around x/c = 0.3. Also, since the cabin is tapered in this part, oval arc radii are typically smaller than at the aft of the cabin.

PITCHING MOMENT

Trim drag can be substantial for BWB aircraft. Therefore the pitching moment during cruise should be limited. Ideally, the aircraft should trim itself during this phase of the flight resulting in zero trim drag. However, in the optimization, this would require an equality constraint. Since this type of constraint presents a difficulty with the heuristic optimization method chosen, such a requirement is deemed infeasible [**?**]. Therefore the pitching moment is bounded by an inequality constraint:

$$g_7 = -0.020 - C_m \leq 0 \tag{5.7}$$

This value is deemed to provide a balance between keeping the pitching moment within reasonable limits without reducing the feasible design space too much. Section 3.4.4 describes the process of calculating the pitching moment. For the filter evaluation performed in AVL, the identical value is used since this method tended to underestimate the pitch down moment.

ANGLE OF ATTACK

The maximum angle of attack during cruise is set at 3° to account for passenger comfort as described in chapter 2:

$$g_8 = \alpha_{\text{cruise}} - 3° \leq 0 \tag{5.8}$$

This value is evaluated by the Euler computations at the design lift coefficient. The AVL filter uses a 4° value since its accuracy is found to be relatively low compared to the SU2 computations.

5.1.4. BASELINE DESIGN

To perform the aerodynamic optimization, an initial design vector has to be established. This baseline design is constructed in the following manner. Firstly, the general layout of the internal volumes is determined. This sets the fuselage's width and approximate length. Secondly, the outer wing airfoils were fitted based on local lift coefficient and Mach number. The outer wing makes use of a supercritical NACA SC(2)-0412 profile for sections 3 and 4. The NACA SC(2)-0410 airfoil is used in section 5. These airfoils provide enough thickness to comply with the t/c constraints as described in Section 5.1.3, including a margin. The maximum local lift coefficient of around 0.6 on the outer wing requires the use of supercritical airfoils. Thirdly, the centerbody airfoil is determined. The centerbody makes use of a reflexed airfoil that is provided in figure 3 of the study by Qin et al.[29]. This airfoil is scaled to 90% of its original thickness to have a better fit with the internal volumes. This yields a thickness-over-chord ratio of 14.6%. The reflexed airfoil was found to have a beneficial effect on the pitching moment: it became less negative compared to a symmetrical airfoil of similar thickness. Setting an initial twist distribution is performed such that a satisfactory, close to elliptical, spanwise load distribution as predicted by AVL is attained. The resulting pitching moment coefficient is slightly below -0.020.

5.1.5. OPTIMIZATION CASES SETUP

In total three optimizations are performed: a planform optimization, a 3D shape optimization and a single step optimization. In Table 5.2 the design vector for each of the optimizations is presented. In this section, each optimization setup is described separately.

Table 5.2: Design vectors used for the three optimizations

Design Vector	Variables	Amount
$\bar{x}_{\text{planform}}$	c_{center}, c_{ow}, Λ_{cb}, Λ_{ow}, b_{ow}, ϵ_3, ϵ_4, ϵ_5, μ_{ow}, ϕ_{kink}, λ_{ow}, $w_{\text{TE,outline}}$	13
$\bar{x}_{\text{shape}}$	$\bar{x}_{\text{CST,0}}$, $\bar{x}_{\text{CST,3}}$,$\bar{x}_{\text{CST,5}}$, ϵ_3, ϵ_4, ϵ_5,$w_{\text{up,1}}$, $w_{\text{low,1}}$,$w_{\text{up,2}}$, $w_{\text{low,2}}$, $z_{\text{TE,1}}$, $z_{\text{TE,2}}$	49
$\bar{x}_{\text{single}}$	c_{center}, c_{ow}, Λ_{cb}, Λ_{ow}, b_{ow}, ϵ_3, ϵ_4, ϵ_5, μ_{ow}, ϕ_{kink}, λ_{ow}, $w_{\text{TE,outline}}$, $\bar{x}_{\text{CST,0}}$, $\bar{x}_{\text{CST,3}}$, $\bar{x}_{\text{CST,5}}$, $z_{\text{TE,1}}$	50

PLANFORM OPTIMIZATION

The planform optimization takes into account 13 variables, including the twist variables. The latter are allowed to vary within a range of 3°. For every other variable, specific bounds are set to guarantee a robust geometry while maintaining a sufficiently large design space. These bounds can be found in Appendix B.

3D SHAPE OPTIMIZATION

The dual step optimization uses the resulting planform parameters of the planform optimized design. It focuses on optimizing the airfoil shapes at each of the sections of the baseline design. The CST-coefficients of sections 0,3,4 and 5 are used to influence the overall shape of the airfoil. For sections 1 and 2, design flexibility is provided by the 8 leading edge cap control points weights as well as the trailing edge heights. Also including the twist angles adds up to 49 variables. The CST-coefficients are bounded to be between 75% and 125 % of their original value while the twist angle range is reduced to 1.5°. The latter should yield a faster convergence in this optimization that has a high number of design dimensions.

SINGLE STEP OPTIMIZATION

The single step optimization has a variable set that consists of both planform and airfoil shape variables. The 13 variables used in the planform optimization are part of the variable set. Regarding the airfoil shape, the 3 CST-defined airfoils and a centerbody trailing edge height $z_{\text{TE,1}}$ are included. The latter is present since the shape optimization featured a distinctive shape due to this variable. In total 50 variables are included, but design freedom for the leading edge caps on the centerbody is limited. Bounds are identical as for the other optimizations and the twist limitations are taken from the dual step optimization.

5.2. OPTIMIZATION RESULTS

Both numerical and visualized results are presented for the four designs in this section. Tables 5.3 and 5.4 summarize the aerodynamic and geometric results of the optimizations respectively. All optimized designs show an increase in aerodynamic efficiency compared to the baseline design. They also have similar reference chord values and none of the designs has a wingspan at the constraint limit of 36 m. The planform optimized design displays an almost 3 counts decrease in inviscid drag compared to baseline, while the viscous drag decreases with 3.5 counts. Furthermore, both the cruise angle of attack and the pitching moment coefficient increase. The internal volume decreases while the wetted area increases. The 3D shape optimization manages to decrease both the viscous and inviscid drag by 1 count each, compared to the planform optimized design. The angle of attack increases with 0.2° and the pitching moment is close to its constraint value. The volume shows a reduction of 4.6% and also the wetted area decreases slightly. Finally, the single step optimized design has an L/D that is lower than for the dual step optimized design. This lower performance stems from a higher inviscid drag coefficient. The single step optimized design has a relatively low angle of attack of 1.8° and a pitching moment coefficient that is also close to the constraint value. Its volume and wetted area are the highest of all 4 designs.

To further assess the designs, their resulting variable settings for each design are present in Tables 5.5 and 5.6. For all the optimized designs, the center chord length, c_{center}, has increased compared to the baseline design. Another common feature of the optimized designs is the increased washout when moving to the wingtip. Furthermore, twist angles for sections 4 and 5 are very similar for the optimized designs. The trailing edge height at section 1 for both the dual and single step optimized designs decreases. The airfoil shapes

Table 5.3: Aerodynamic results of the optimization cases. All values are calculated with an S_{ref} of 450 m^2.

Design	C_L/C_D	C_L [-]	C_D [cts]	$C_{D,\text{inv}}$ [cts]	$C_{D,\text{visc}}$ [cts]	α [°]	C_m [-]
Baseline	18.9	0.20	106.0	50.8	55.2	1.8	-0.0207
Planform opt.	20.0	0.20	99.8	48.1	51.6	2.2	-0.0163
Dual step opt.	20.5	0.20	97.5	47.0	50.5	2.4	-0.0194
Single step opt.	20.3	0.20	98.5	48.0	50.5	1.8	-0.0196

Table 5.4: Geometric results of the optimization cases

Design	S_{wet} $[\text{m}^2]$	V $[\text{m}^3]$	$c_{\text{ref}}[m]$	$x_{\text{cg}}[m]$	$b_{\text{total}}[m]$	S $[\text{m}^2]$
Baseline	1014	1063	23.2	16.8	35.2	454
Planform opt.	1020	1054	23.5	18.2	35.7	451
Dual step opt.	1008	1006	23.5	18.3	35.7	451
Single step opt.	1025	1079	23.5	21.9	35.5	442

Table 5.5: Variable values defining the outer shape for the various versions

	Variable	Baseline	Planform opt.	Dual step opt.	Single step opt.
	c_{center} [m]	37	37.32	37.32	38.58
	c_{ow} [m]	7.5	7.89	7.89	8.08
	Λ_{cb} [°]	68	70.4	70.4	74.4
	Λ_{ow} [°]	45	50.8	50.8	47.0
	b_{ow} [m]	9	9.92	9.92	10.09
Planform	ϵ_3 [°]	0	0.13	-0.02	0.22
	ϵ_4 [°]	0	-0.34	-0.47	-0.54
	ϵ_5 [°]	-2	-3.32	-3.43	-3.25
	μ_{ow} [-]	0.2	0.173	0.173	0.182
	ϕ_{kink} [-]	0.2	0.181	0.181	0.174
	λ_{ow} [-]	0.2	0.226	0.226	0.183
	w_{TE} [-]	[1,1,1,1]	[1,1.86, 0.92,1]	[1,1.86, 0.92,1]	[1,2.42, 1.72,1]
LE caps	$w_{\text{up},1}$ [-]	[1,1,1,1]	[1,1,1,1]	[1,1.34, 0.89,1]	[1,1,1,1]
	$w_{\text{low},1}$ [-]	[1,1,1,1]	[1,1,1,1]	[1,1.07 , 1.42, 1]	[1,1,1,1]
	$w_{\text{up},2}$ [-]	[1,1,1,1]	[1,1,1,1]	[1,1.85 , 0.59,1]	[1,1,1,1]
	$w_{\text{low},2}$ [-]	[1,1,1,1]	[1,1,1,1]	[1, 1.92, 0.93,1]	[1,1,1,1]
TE caps	$z_{\text{TE},1}$ [m]	1.05	1.05	0.78	0.85
	$z_{\text{TE},2}$ [m]	1.05	1.05	1.25	1.05

belonging to the CST coefficient results are treated later in this section. The remaining planform variables are discussed at the hand of the top view pressure distributions.

These pressure distributions at cruise conditions are presented in Figure 5.1 for all four designs. The baseline design in Figure 5.1a has a 45° swept leading edge on the outer wing. The outer wing shows lower pressure coefficients than the centerbody. Especially at the wingtip, the leading edge suction peak is relatively high with a value of C_P = -1.6. On the outer wing, a region of suction increase is seen around the half chord position. Despite the loading on the outer wing, the isobars do not indicate the presence of a shockwave. The planform optimized design in Figure 5.1b features an outer wing which is swept back almost 6° further than at the baseline design. Regarding the centerbody, its sweep increases and it features a more square-like trailing edge. The width of the straight trailing edge section decreases, while the suction peak on the outer wing reduces to a value of C_P = -1.3.

As can be seen in Figure 5.1c, the flow field on the outboard part of the dual step optimized design is different compared to the planform optimized design. The suction peaks are lower and the pressure stays more or less constant until the half chord position. Also, an area of increased suction is present at the zero sweep trailing edge part. As can be seen in Figure 5.1d, the planform shape for the single step optimized design differs from the dual step optimized design. The major difference is a more aft-placed outer wing

Table 5.6: CST values results for the various versions. $\bar{x}_{CST} = [A_1, A_2, ..., A_{12}]$

Version	Section	$\bar{x}_{CST}$
Baseline & Planform optimized	0	(0.2072, 0.2646, 0.1456, 0.2385, 0.1597, 0.1912, -0.1898, -0.1431, -0.1875, -0.1616, -0.2421, -0.2530)
	3 & 4	(0.1823, 0.1195, 0.1490, 0.2179, 0.1249, 0.2745, -0.1809, -0.1261, -0.1357, -0.2602, -0.0796, 0.1409)
	5	(0.1475, 0.1029, 0.1193, 0.1878, 0.0951, 0.2509, -0.1462, -0.1103, -0.1036, -0.2209, -0.0823, 0.1358)
Dual step optimized	0	(0.1682, 0.2049, 0.1279, 0.231, 0.1859, 0.1919, -0.225, -0.1225, -0.1486, -0.1829, -0.2745, -0.2206)
	3 & 4	(0.1472, 0.1452, 0.1853, 0.1789, 0.1027, 0.3005, -0.1677, -0.1295, -0.1174, -0.2179, -0.0874, 0.1211)
	5	(0.1375, 0.1027, 0.1412, 0.2018, 0.0727, 0.2110, -0.1486, -0.1112, -0.1037, -0.2034, -0.0817, 0.1247)
Single step optimized	0	(0.1747, 0.3193, 0.1427, 0.1988, 0.1973, 0.1811, -0.2196, -0.1483, -0.197, -0.1764, -0.2589, -0.2437)
	3 & 4	(0.1568, 0.1055, 0.1838, 0.219, 0.1319, 0.3377, -0.147, -0.1136, -0.1586, -0.2937, -0.0816, 0.1177)
	5	(0.1751, 0.1188, 0.0942, 0.1822, 0.0997, 0.2988, -0.1438, -0.1097, -0.093, -0.1758, -0.0975, 0.1609)

with a lower sweep angle. The centerbody sweep angle increases by a noticeable amount. Similarities are present on the trailing edge of the centerbody, which has a square shape again. The overview shows lower leading edge suction peaks compared to the planform optimized design, but a similar pressure pattern is visible around halfway the chord on the outer wing. Also, a region of suction occurs at the zero trailing edge sweep section, although it is less pronounced as in the dual step optimized design.

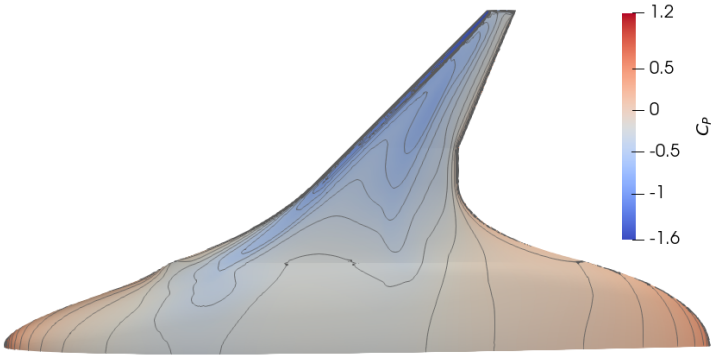

(a) Baseline

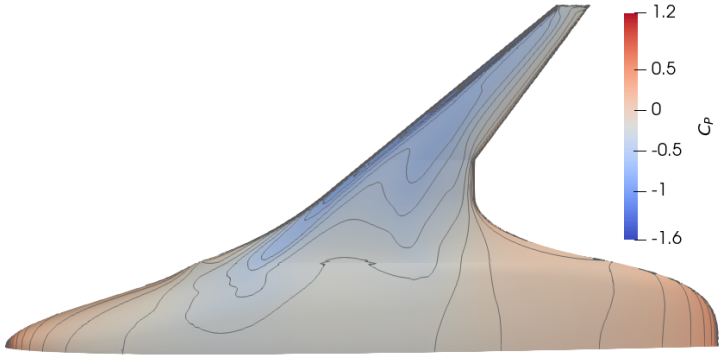

(b) Planform optimized

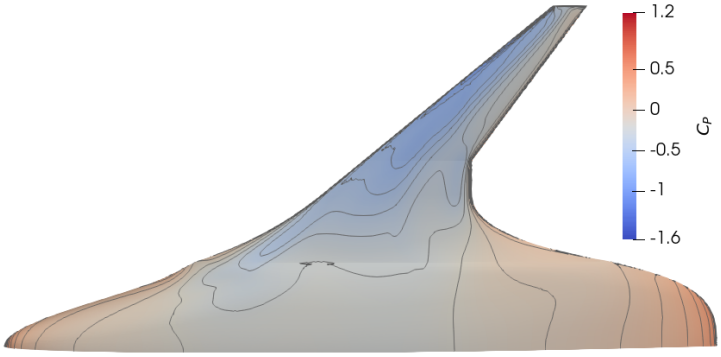

(c) Dual step optimized

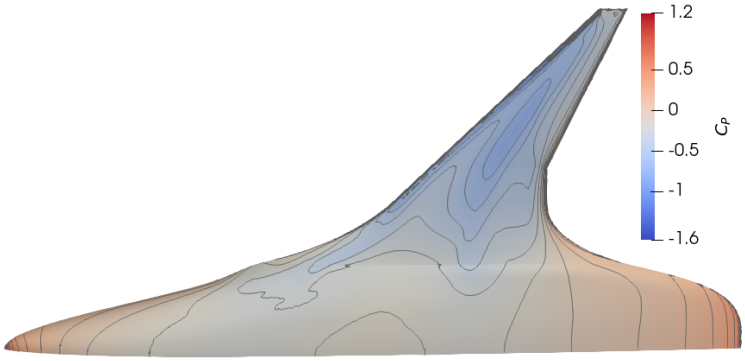

(d) Single step optimized

Figure 5.1: Pressure contours on the upper side of the various designs, $C_L = 0.2$, Mach = 0.78.
Isobars are plotted with a spacing of $C_P = 0.1$

OPTIMIZATION CONVERGENCE AND CONSTRAINT ACTIVITY

Figure 5.2 shows the convergence of each optimization to their maximum L/D value. The SU2 computation number concerning the total amount of SU2 computations for the optimization at hand, forms the horizontal axis. The initial L/D value for each optimization stems from the first feasible design. As can be seen, the largest improvements take place in the first quarter of the optimizations. The planform and dual step optimizations display a small performance increment in the remainder of the optimization while the single step optimized design reaches its optimum value already in this early stage. The latter is thought to show an indication of the ability of the DE algorithm to, by chance, reach an optimum after a limited amount of computations. Since the performance increase is small or zero in the last half of the optimizations, convergence to a local or potentially global minimum is achieved. Furthermore, the large improvements visible in optimizations which include planform variables indicate that these are key in reaching an optimum design.

The computational times vary among the different optimizations. The planform optimization took 109 hours, the shape optimization 490 hours, and the single step optimization 206 hours. Hence, the computational cost for the shape optimization relative to the gained performance increase is high. Despite yielding a slightly lower performance in terms of aerodynamic efficiency, the single step optimization required almost three times less computational effort than the total dual step optimization.

Constraint activity cannot directly be quantified with the used optimization algorithm. However, the pitching moment coefficients for the dual step and single step optimized design are close to the constraint value. Hence it is believed that the pitching moment constraint is a drive in the optimization, which agrees with the literature [39]. The lowest thickness-over-chord ratio found in the optimized designs for section 3 is 14.1%, occurring for the planform optimized design. For section 5 this value is equal to 12.1

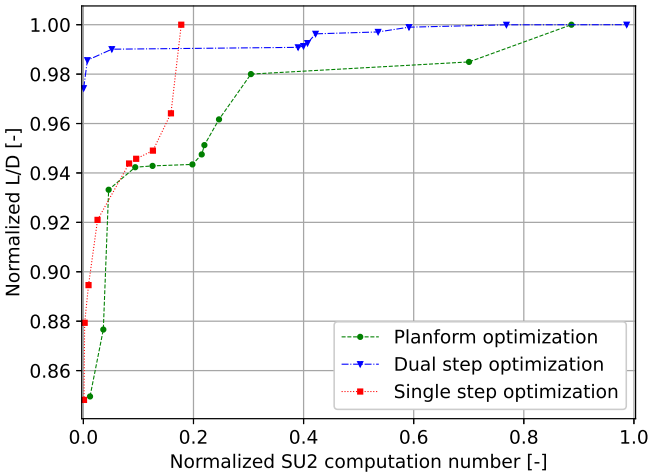

Figure 5.2: Convergence to the maximum L/D value for each optimization

SPANWISE LIFT DISTRIBUTIONS

Two different representations of the spanwise aerodynamic load distribution are plotted in Figure 5.4. The spanwise lift distribution in Figure 5.3a shows the results for the four designs. Also, an ideal elliptical lift distribution that helps to minimize induced drag is presented for C_L = 0.2 and b = 35.5 m. Regarding this elliptical distribution, the baseline design displays a lower aerodynamic loading on the centerbody. The wing fairing and outer wing compensate for this by having a higher lift load. It can be seen that all optimized designs increase inboard loading while reducing the outboard load. This yields lift distributions that are closer to the elliptical distribution. Load relief on the outboard wing can also be seen in Figure 5.3b. The maximum sectional lift coefficient of the baseline design is 0.65. For the single step design, this value drops to 0.61, and for the planform and optimized designs to 0.57. The lift coefficients on the wing fairing (25 to 50 % of span) are typically higher for the optimized designs compared to the baseline design. This does not directly translate to a higher sectional aerodynamic load on the fairing and hence it should be contributed to reduced chordlengths in this region. On the center section, the sectional lift coefficients are around 0.06 for all designs. Due to this relatively low value, supercritical airfoils are not necessary on this part. It even allows

for thick sections without causing high supervelocities as can be seen in the pressure distributions.

The lift distributions of the optimized designs partially result from a modified twist distribution. The latter is almost identical for all optimized designs and shows an increased washout towards the wingtip compared to the baseline design. This agrees with the study of Qin et al.[29], which also displays an aerodynamic load reduction on the outboard wing mainly by increasing washout. However, in this study the reduction of wave drag does not appear to be the primary beneficial effect due to the absence of shock waves. Hence the lift distribution resembles a more elliptical shape instead of a combination with a triangular outline as seen in the work by Qin et al. Hence, the more elliptical lift distributions of the optimized designs are thought to be the main reason for the reduced inviscid drag coefficients. The resulting lift load on the center section shows more variety among the optimized designs. The single step optimized design displays a similar load as the baseline design here. The planform and dual step optimized designs show an increase in aerodynamic loading. Since the planform and baseline design feature the same center airfoil, the main reason for this increase is believed to be the higher angle of attack. The dual step optimized design has an even higher aerodynamic load on the center to which its modified airfoil shape also contributes. The relative increase of the aerodynamic load for the single step optimized design between 10 and 20% of the span is believed to relate to the low trailing edge in this section. The difference in pitching moment between the baseline and the planform optimized design can be partially attributed to less outboard loading. Hereby, the lift shifts along the swept wing forward and changes the pitching moment as reasoned by Lyu and Martin [39].

In Figure 5.4, the normalized spanwise lift distributions of both the baseline and dual step optimized designs are presented. Also the elliptical lift distributions and normalized sectional lift derivatives, $c_{l_\alpha} \cdot c$, are plotted for both designs. This indicates the alterations in the lift distribution for different angles of attack. Although the lift distribution at the design cruise lift coefficient is already near the elliptical lift distribution, the sectional lift derivatives show a closer distribution. Especially on the inboard part, the resemblance to the elliptical shape is higher. This could indicate that improvements can be made by further optimizing the inboard airfoil shapes and twist distribution.

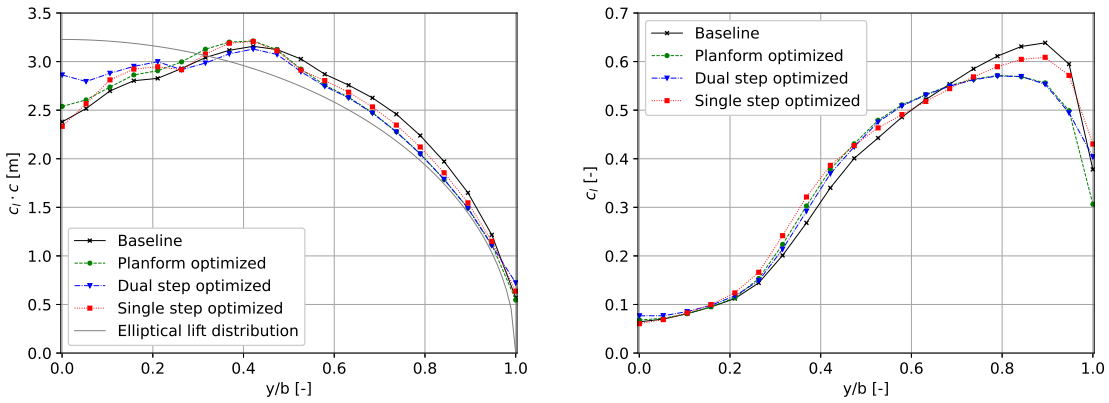

(a) Spanwise lift distribution, elliptical for b = 35.5 m

(b) Spanwise sectional lift coefficient

Figure 5.3: Spanwise aerodynamic load on the optimized designs, C_L = 0.2, Mach = 0.78

VISCOUS DRAG DISTRIBUTION

The resulting spanwise viscous drag load for each design is presented in Figure 5.5. The results can be interpreted with the use of the empirical strip equations. It can be seen that all optimized designs show an improvement compared to the baseline design, despite longer chordlengths on the centerbody. Since all optimized designs have an increased centerbody leading edge sweep angle and a more rectangular trailing edge outline, the semi-chord sweep angles are increased. The reduction this causes in form factor is clearly visible when comparing the planform optimized and baseline design on the centerbody section, since they have identical airfoil shapes. The dual step optimized design shows an even further reduction of viscous drag on the centerbody compared to the planform optimized design due to its modified airfoil shape. The latter yields a lower thickness-over-chord ratio and hence a reduction of form factor. The values for C_F are constant for the four designs on most spanwise locations. The maximum difference between local C_F values was found to be 3% and is purely caused by a different chordlength. Since this difference in C_F is small, the increased sweep

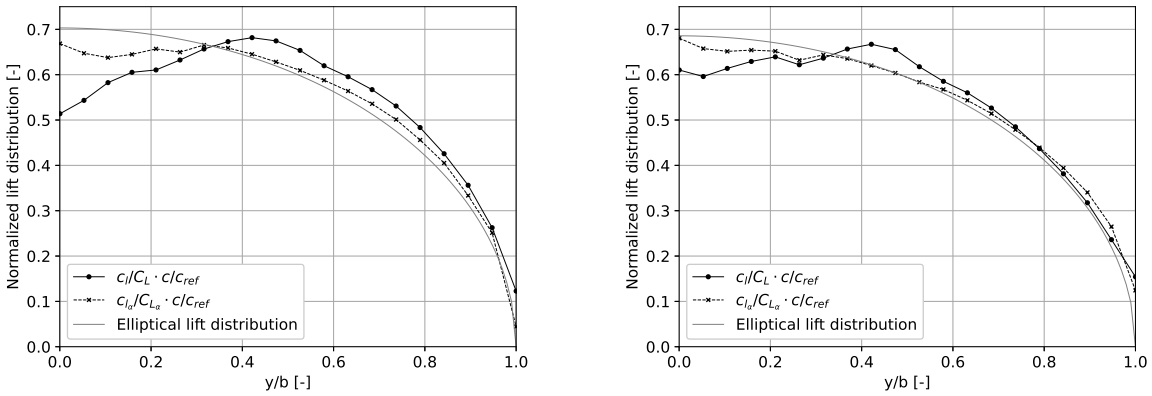

(a) Baseline

(b) Dual step optimized

Figure 5.4: Spanwise normalized lift and c_{l_α} distributions for the baseline and dual step optimized designs, C_L = 0.2, Mach = 0.78

angles are the main contributors to the viscous drag reduction of 3 counts displayed by the planform optimized design compared to the baseline design. The used factors of influence in the empirical method could therefore be a driver in the shape optimization, which should be verified in further research. Around y/b = 0.15 a decrease in the reduction of the viscous drag load with span can be distinguished. This was found to be caused by a negative semi-chord sweep angle in combination with a relatively high thickness-over-chord ratio.

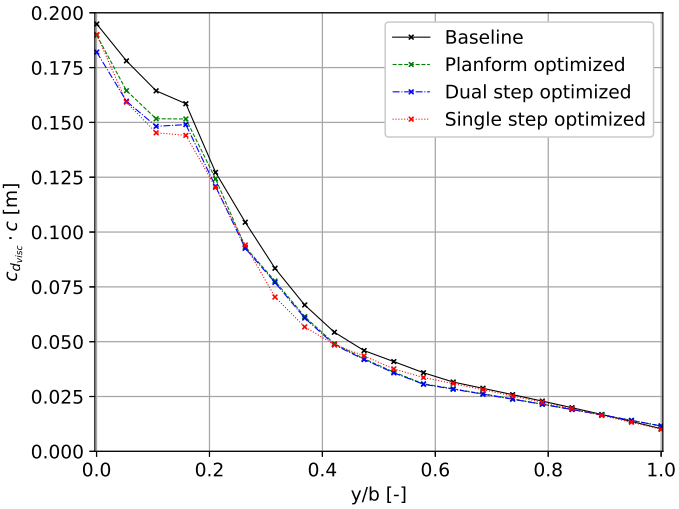

Figure 5.5: Distribution of the local viscous drag coefficient following from the empirical strip methods

CROSS-SECTIONAL AREA DISTRIBUTIONS

A cross-sectional area distribution is provided in Figure 5.6. The cross-sections are made along the x-axis in the yz-plane. In this figure also a Sears-Haack body area distribution is presented. Such a body minimizes zero-lift wave drag in transonic flow [48]. The Sears-Haack body is plotted using the volume and center chord length as an input according to equation 6.50, page 298 in the work by Vos and Farokhi [48]. The body shape is plotted for a volume of 1063 m^3 and a length of 34 m. Hence, it can only be directly compared to the baseline design. Direct comparisons for the other optimized designs can be found in Appendix C.

It can be seen that the baseline design matches the Sears-Haack body well. This agrees with the study of Wakayama [74], which also mentions the higher similarity of a BWB with a Sears-Haack body compared to a conventional aircraft. Additionally, smooth transitions are present, which was also contributes to reducing the wave drag [48]. The front half of the baseline design shows a higher volume compared to the Sears-Haack

body, while it lacks volume in the aft half. The optimized designs all show an aft shift of internal volume, which brings them closer to the ideal sectional area distribution. This shift matches with the higher wing sweep angles. The single step optimized designs aft positioning of the outer wing is also visible in Figure 5.6. The volume difference between the planform and dual step optimized designs stems from the front half shape altering of the aircraft. It was found the dual step optimized design matches the Sears-Haack distribution best of all four designs.

It should be kept in mind that the area distributions do not include vertical fins, engine pylons and engine nacelles. The placement of these components can be used to improve the area distributions. Although wave drag is not a primary drag source for the optimized designs, the similarities of the optimized designs with the Sears-Haack body indicate a potential for higher cruise speeds at a limited performance penalty.

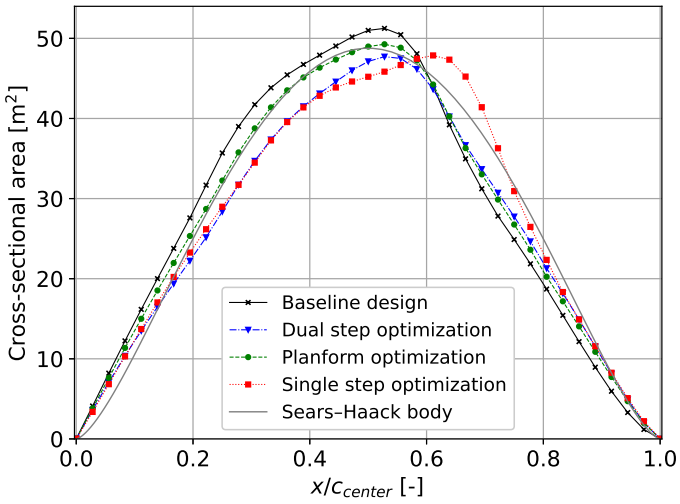

Figure 5.6: Cross-sectional area distribution for all designs, including the Sears-Haack body for V = 1063 m^3, l = 37 m

SECTIONAL PRESSURE DISTRIBUTIONS

In Figure 5.7, 2D pressure distributions of the planform and the dual step optimized designs are presented for a range of spanwise sections. Also in part of the plots, the critical pressure coefficient C_P^* is presented for reference. On the centerbody, pressure coefficient values for the dual step optimized design are lower while the pressure difference between the lower and upper sides stays more or less constant. The downforce on the aft part of the centerbody is reduced as can be seen in figures 5.7a and 5.7b. On the wing fairing and outer wing, the suction peak present at the leading edge has largely been removed as shown in Figures 5.7c to 5.7f. Instead supersonic plateaus are present which provide front-loading for the airfoil. For both designs, the flow decelerates to subsonic speeds without displaying a shockwave. The aft loaded part of the supercritical airfoils stays more or less constant. The adverse pressure gradient present at the trailing edge of the outboard sections has such steepness that in viscous flow conditions separation is very likely to occur. This separation causes a reduction of the aft load generated on the supercritical airfoils. Hence more lift would need to be generated on the centerbody. Reist and Zingg [75] demonstrate this effect by performing a RANS analysis on a Euler optimized BWB. The regions of aft suction are noticeably smaller for the optimized designs in the LH2BWB study and hence the inboard load shift caused by separation is believed to be smaller compared to the study by Reist and Zinng [75]. Also the lift distributions allow for a small reduction of outboard loading while still maintaining an elliptical shape as can be seen in Figure 5.4. The pitching moment decrease for the dual step optimized design is believed to be caused by the altered chordwise pressure distributions, which show a lower leading edge suction peak on the outboard sections and no aft downforce on the centerbody. The reduction of the downforce also contributes to the aerodynamic load increment on the center section of the dual step optimized design as seen in Figure 5.3a.

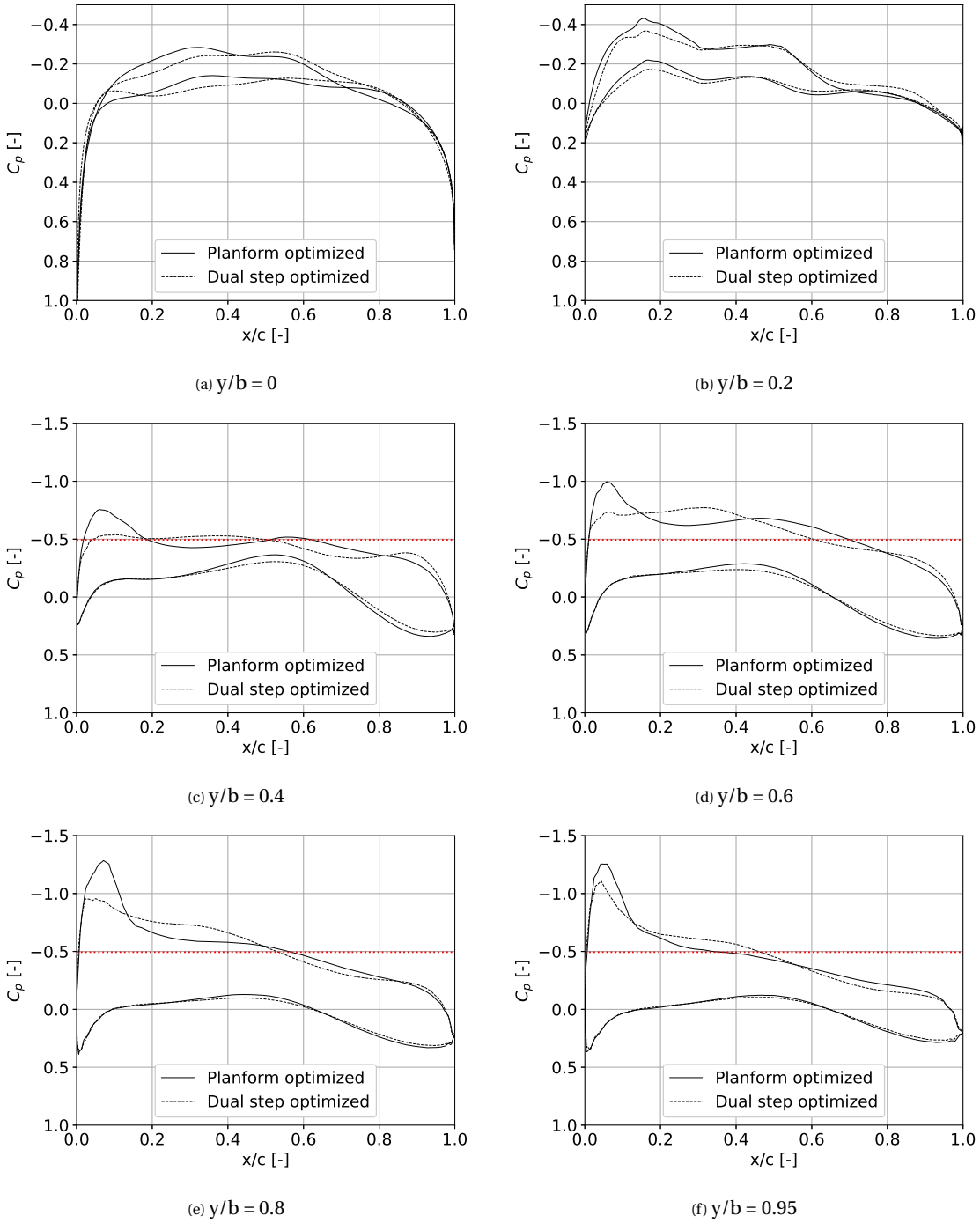

(a) y/b = 0

(b) y/b = 0.2

(c) y/b = 0.4

(d) y/b = 0.6

(e) y/b = 0.8

(f) y/b = 0.95

Figure 5.7: Resulting C_p distributions of the dual step optimized design compared to the planform optimized design at various spanwise sections. Conditions C_L = 0.2, Mach = 0.78 and C_p^* = -0.494 (horizontal dashed line)

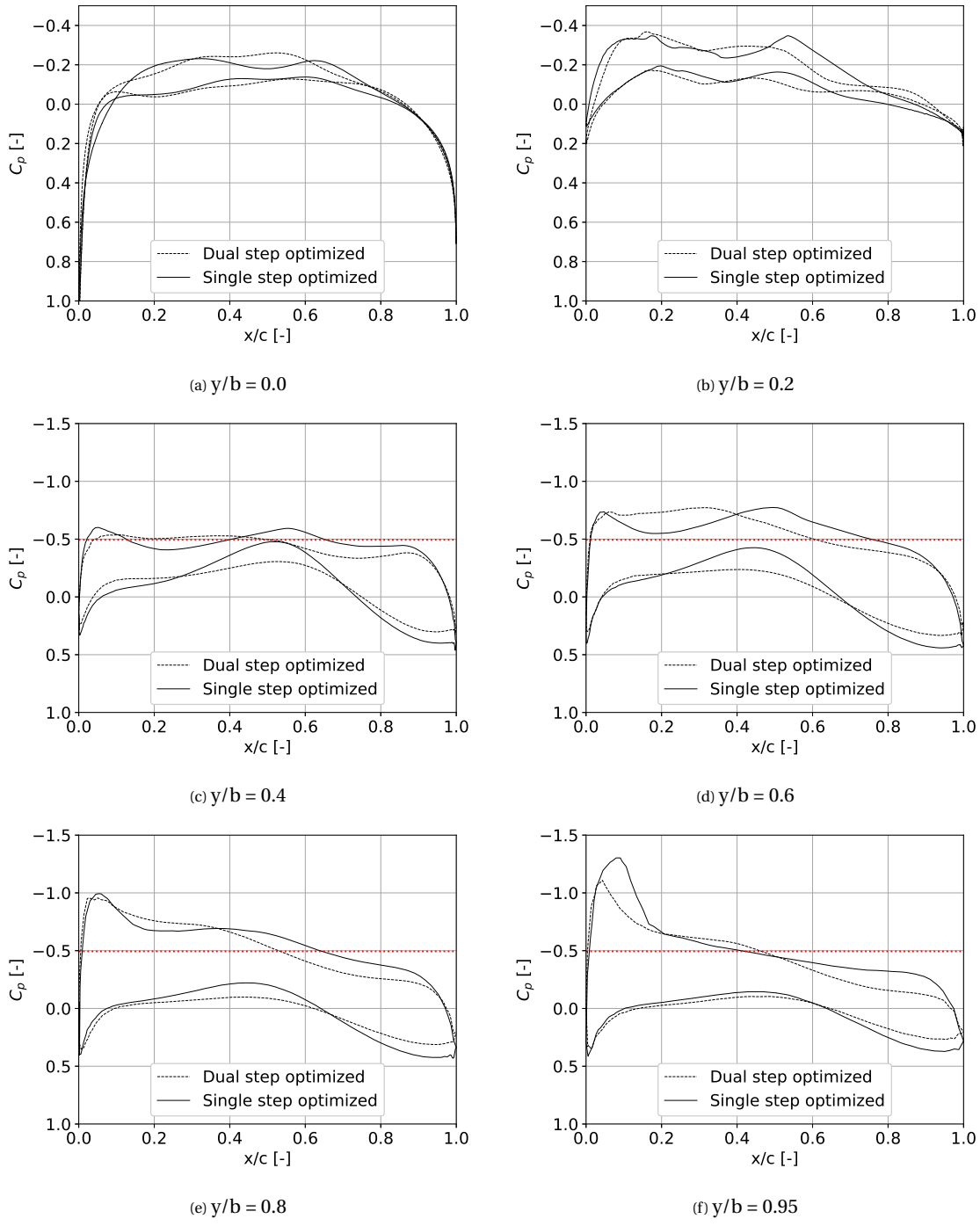

(a) y/b = 0.0

(b) y/b = 0.2

(c) y/b = 0.4

(d) y/b = 0.6

(e) y/b = 0.8

(f) y/b = 0.95

Figure 5.8: Resulting C_p distributions of the single step optimized design compared to the dual step optimized design at various spanwise sections. Conditions C_L = 0.2, Mach = 0.78 and C_p^* = -0.494 (horizontal dashed line)

A comparison between the chordwise pressure distributions of the dual step and single step optimized designs is presented in Figure 5.8. The centerbody sections in Figure 5.8a and 5.8b show that for the single step optimized design, more lift is generated just before and aft of the semi-chord in comparison to the dual step optimized design. Also, a relatively sharp suction peak can be distinguished just aft of the semi-chord position at y/b = 0.2. For the outboard part, the pressure distributions in Figure 5.8c to 5.8e show suction peaks that are similar in value, but followed by a larger pressure recovery. Supersonic plateaus such as seen in the shape optimization are less present and a lower amount of lift is produced directly behind the suction peak. Towards the tip, the leading edge suction peak is higher and spans a longer proportion of the chordlength. The aft loading of the airfoil however increases for every outboard section and larger adverse pressure gradients are present at the trailing edge. Although the chordwise pressure distributions for these two designs are different, they yield an identical pitching moment coefficient which is close to the constraint value. Therefore, a performance increment could occur when more negative pitching moments are allowed. This would increase the trim drag and hence a trade-off is thought to be present here.

The parameterization of the outer mold line of the models features a 'bubble' on the leading edge transition from the centerbody to the outer wing. Since this bubble is unintended, its effect on the pressure distribution is assessed. Figure 5.9 shows the sectional pressure distribution at the spanwise location where the bubble occurs. At the leading edge, first, a pressure recovery is seen before the pressure coefficient decreases. This does not match the results presented earlier and therefore the bubble causes a deviation in the pressure field. The curvature introduced to the leading edge leads to suction taking place at this section along the leading edge in a spanwise direction. It can also be seen that the middle part of the section does not feature any curvature and therefore pressure is constant at this part.

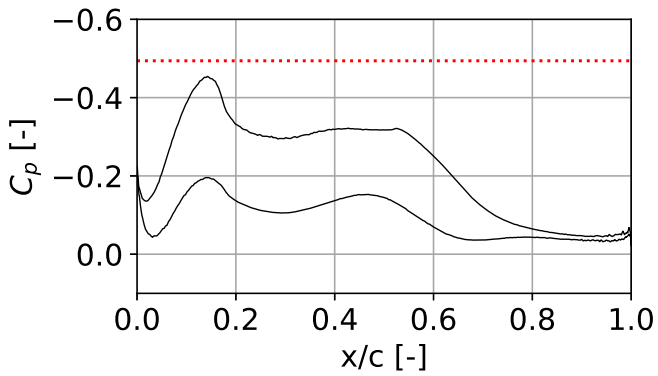

Figure 5.9: Resulting C_p distribution of the dual step optimized design at the spanwise transition from the centerbody to the wing fairing. Conditions C_L = 0.2, Mach = 0.78 and C_p^* = -0.494 (horizontal dashed line)

SECTIONAL SHAPES

In Figure 5.10, the streamwise sectional shapes for both the planform and dual step optimized designs are presented. The center airfoil in Figure 5.10a shows a decrease in thickness and camber on the front half of the airfoil. The other centerbody section in Figure 5.10b shows similar changes and also presents the lower trailing edge height. For both sections, the leading edge radius decreases compared to the planform optimized design. The thinner section shapes match with the less negative pressure coefficients present on the dual step optimized centerbody. They also display that the cross-sectional area reduction on the front half of the dual step optimized design in Figure 5.6 stems from the centerbody. The reduction of the aft downforce in the dual step optimized design is caused by the decrease in aft reflex.

The outboard sections in Figure 5.10c to 5.10f show differences between the two designs which are similar for each section. The leading edge radius is smaller and an increased camber is present at the middle section of the airfoils. Also, the sections are thinner overall. These shape features yield the supersonic plateaus on the front parts of the sections. Since the aft part of the outboard sections is more similar, also smaller differences in aft loading are present.

The section comparison for the dual and single step optimized designs is presented in Figure 5.11. The centerbody sections display a difference in thickness on the front half of the airfoil, while the leading edge radius

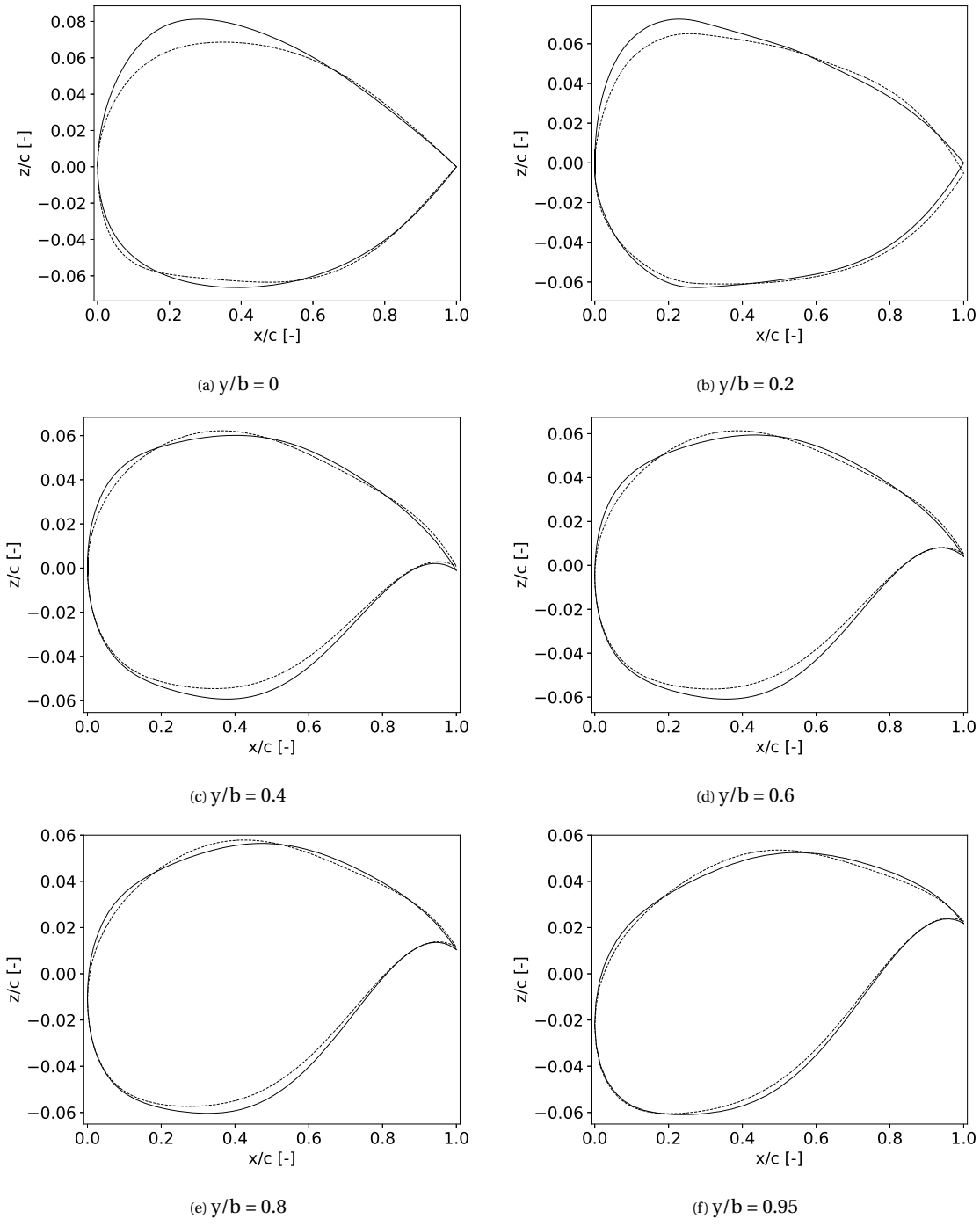

(a) $y/b = 0$ (b) $y/b = 0.2$

(c) $y/b = 0.4$ (d) $y/b = 0.6$

(e) $y/b = 0.8$ (f) $y/b = 0.95$

Figure 5.10: Sectional shape results for the dual step optimized design (dashed) compared to the planform optimized design (continuous)

is more or less identical as can be seen in Figures 5.11a and 5.11b. Hence the center airfoil shape for the single step optimized design is closer to the baseline center section, while also their angles of attack are similar. Hence a similar aerodynamic load occurs in the symmetry plane as can be seen in Figure 5.3a.

The outboard sections in Figure 5.11c to 5.11e display that the single step optimized design has thicker sections from 35 % of the chordlength up to the trailing edge. This thickness explains the higher suction values seen in the aft half of the sectional pressure distribution of the single step optimized design. The leading edges radius is similar for both designs. This provides similar suction peak strengths as seen in the pressure distributions. The outer wing section in Figure 5.8f shows less twist for the single step optimized

design and hence displays a higher suction peak.

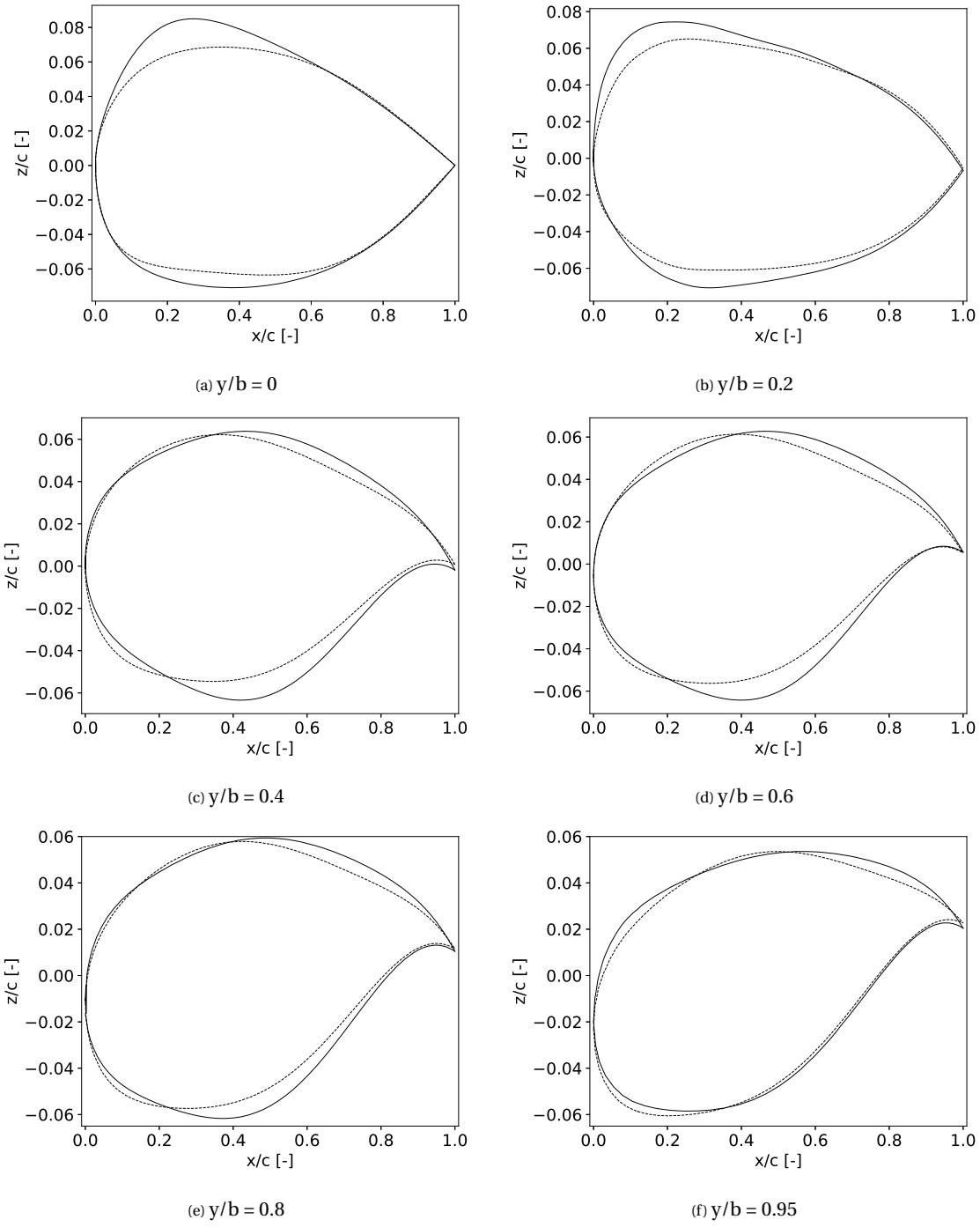

(a) $y/b = 0$ (b) $y/b = 0.2$

(c) $y/b = 0.4$ (d) $y/b = 0.6$

(e) $y/b = 0.8$ (f) $y/b = 0.95$

Figure 5.11: Sectional shape results for the single step optimized design (continuous) compared to the dual step optimized design (dashed)

5.3. LH2BWB CONCEPT PERFORMANCE AND COMPARISON

This section aims to provide more general insight into the performance and characteristics of the LH2BWB concept. This is done by first providing an overview of performance at various angles of attack. Secondly, the concept is compared to other aircraft and studies.

5.3.1. OVERALL PERFORMANCE RESULTS

To further assess the performance of the aircraft at conditions other than the design cruise condition, two performance polars are plotted in Figure 5.12. The drag polars for all four designs can be found in Figure 5.12a, while the L/D polars are displayed in figure 5.12b. As can be seen, the optimized designs show an L/D improvement on the entire displayed range. The growth in efficiency also slightly increases with a rising lift coefficient, especially when comparing the baseline design with the dual step optimized design. The latter shows a flatter peak in its polar. This indicates that the design does feature a large performance reduction when moving away from the design operating conditions. Furthermore, the design cruise lift coefficient of 0.2 seems to be close to the polar optimum for all the designs. The optimization setup for this lift coefficient probably contributes to this.

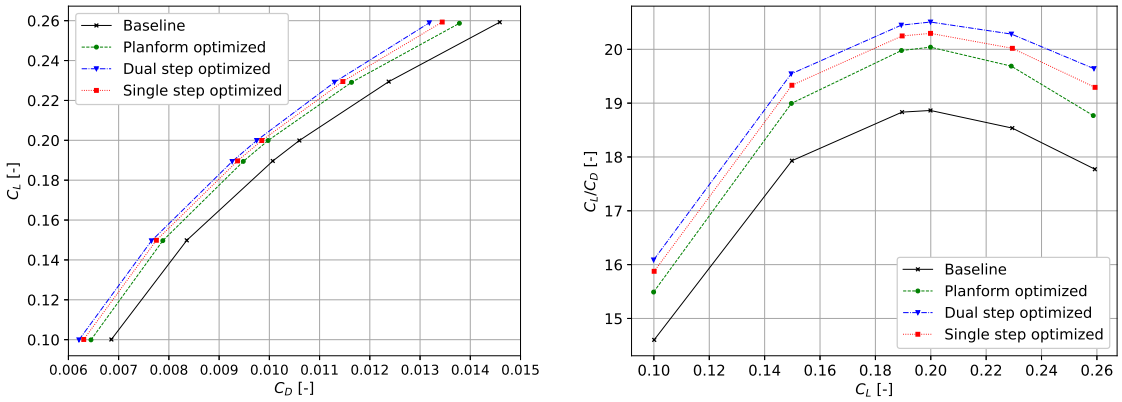

(a) Drag polar

(b) L/D polar

Figure 5.12: Aircraft performance polars of the various designs, Mach = 0.78

Table 5.7 presents data that describes the development of aerodynamic characteristics when moving away from the design point. The lift curve slope, C_{L_α} is in the same order of size for all designs, although the planform and dual step optimized designs are slightly less sensitive to changes in the angle of attack. The pitching moment derivative C_{m_α} is negative for all designs, making them longitudinally stable. The values for the Oswald efficiency number, e_0, and the zero-lift drag coefficient, C_{D_0}, stem from fitting the following equation [2] to the drag polars in Figure 5.12a:

$$C_D = C_{D_0} + \frac{C_L^2}{\pi A R e_0} \tag{5.9}$$

Although the curve fitting method has limited accuracy, it can be seen that the efficiency number increases for the optimized designs. This indicates a smaller drag increment when increasing the lift, which can also be seen in Figure 5.12a. The higher efficiency numbers for the optimized designs are likely due to an improved lift distribution. Also, the zero-lift drag decreases as a result of viscous drag reduction.

Table 5.7: Summary of additional performance data.C_{L_α} and C_{m_α} are calculated using lift coefficients equal to 0.19 and 0.20

	C_{L_α} $[\text{rad}^{-1}]$	C_{m_α} $[\text{rad}^{-1}]$	e_0 [-]	C_{D_0} [-]
Baseline	3.07	-0.064	0.86	53.4
Planform opt.	2.90	-0.064	0.88	50.1
Dual step opt.	2.88	-0.057	0.92	49.3
Single step opt.	3.03	-0.060	0.91	49.6

5.3.2. LH2BWB CONCEPT COMPARISON

Various aircraft characteristics resulting from this study are put into perspective to assess the specificity of this concept.

The aircraft equivalent skin friction drag, $\bar{c}_f$, can be computed using the following equation [76]:

$$C_{D_0} S_{\text{ref}} = \bar{c}_f S_{\text{wet}} \tag{5.10}$$

This parameter allows the comparison of viscous drag between aircraft, regardless of their size. For the dual step optimized design, this results in a value of $2.2{\cdot}10^{-3}$, which is relatively low compared to the value of $2.8{\cdot}10^{-3}$ found on the Airbus A320 [76]. Engines, vertical fins and control surfaces are not taken into account on the assessed LH2BWB designs. However, the increment of C_{D_0} caused by the addition of these elements goes along with a wetted area increase. Therefore, the difference in $\bar{c}_f$ caused by the additional components does not justify the large difference with the conventional reference aircraft. It is believed that the high Reynolds numbers present on the centerbody reduce this estimated drag component, since these form an integral part of the viscous drag estimation method used in this work. Higher-order simulations can provide further insight into these observations.

The size of the LH2BWB concept can be compared based on its wetted area. For the CSR-01 reference aircraft excluding the vertical tail, this value is around 740 m^2 [77]. This aircraft has the same passenger capacity and design range and features a conventional layout. Although the wetted area is 26% lower compared to the LH2BWB, the reference aircraft does not include a large LH_2 tank. BWB's normally have a lower wetted area compared to their conventional counterparts and hence this is an indication of the cost of integrating hydrogen. This penalty also applies to hydrogen-powered conventional aircraft, as described in Section 2.2.

When comparing the resulting LH2BWB shapes to kerosene-powered BWB's from other studies, multiple specific features of the tank integration arise. Placing the large hydrogen fuel tank behind the passenger cabin results in a relatively long center chord. Reist and Zingg [78] studied a kerosene-powered BWB with a nominal mission of carrying 160 passengers over 1000 NM. This aircraft has a center chord length of 30.5 m and is around 20% shorter than the optimized LH2BWB designs. Furthermore, the geometries used in major BWB studies by NASA [19] and the MOB project [29] do not feature a major part of the aft centerbody located behind the outer wing trailing edge. Due to the long center chord on the LH2BWB, the local lift coefficient of around 0.05 at the center airfoil is relatively low. The elongated centerbody stems mostly from the chosen tandem configuration of the cabin and tank. Also, the resulting ratio between length and width of the centerbody partially follows from the chosen cabin configuration. However, a wider cabin takes up more of the span and requires a thicker centerbody. Therefore, a long centerbody is considered to be part of the optimal solution for this concept.

Another observation regarding the lift distribution is that it approximates an elliptical shape. The study by Qin et al. [29] show optimized designs with a combined elliptical-triangular which results in the reduction of shock waves on the outboard wing. The absence of shock waves due to the design conditions used in this study relieves the need for further outboard load reduction. The study earlier mentioned study by Reist and Zingg [78], also displayed a lift distribution that tended more towards an elliptical shape. This study uses similar cruise conditions with $C_L = 0.22$ and Mach = 0.79. Therefore, the optimized lift distribution is believed to primarily depend on these conditions for the concept.

To quantify the effect of hydrogen fuel tank integration, the resulting L/D ratio of around 20 cannot be directly compared to kerosene-powered BWB's. However, Reist and Zingg [78] display an L/D of 26 for their optimized BWB with a similar mission. This value is computed using a RANS solver at similar cruise conditions as used in this study. The L/D values resulting from other studies can be found in Appendix D.The performance of the LH2BWB concept is thought to be a little lower than for conventional BWB's, although a direct comparison is necessary to verify this observation.

6

CONCLUSION & RECOMMENDATIONS

6.1. CONCLUSION

The goal of this study was to find the optimum shape in terms of aerodynamic efficiency during cruise conditions for the LH2BWB concept.

Pressure is rising on the aviation industry to innovate aircraft designs so that they can comply with the sustainability goals set to reduce climate change. Liquid hydrogen could serve as an innovative and cleaner propellant but its large storage volume introduces a challenge. Blended-wing-body aircraft could form a solution to this challenge due to their relatively high internal volume to wetted area ratio. Earlier research on the combination of these types of aircraft with liquid hydrogen tanks was mainly conducted using kerosene-based blended-wing-bodies. To gain further insights on optimum shape features for a liquid-hydrogen-powered blended-wing-body, an inside-out design approach was applied. The LH2BWB concept was sized, parameterized and aerodynamically optimized. The studied concept has a 150 passenger capacity and is aimed to have a range of 2750 NM. This leads to a liquid hydrogen tank with a volume of 98.5 m^3.

The geometry parameterization features 13 planform variables, excluding variables that were fixed during optimization. A total of 49 parameters can be varied to adjust the shape of the airfoil sections. Starting from a baseline design, both a dual step and a single step aerodynamic shape optimization were performed. The design cruise conditions applied during this single point optimization are Mach = 0.78, lift coefficient = 0.2 , cruise height = 11,000 m and reference area = 450 m^2. As an optimization algorithm, the differential evolution method was chosen. The Euler equations in combination with an unstructured mesh were used to estimate the inviscid drag. An empirical strip method was employed to quantify the viscous drag component. A pitching moment constraint was imposed to limit the amount of trim drag for a design.

The optimization resulted in two different designs in terms of planform and shape, which indicates the presence of multiple local optima. A 6 count drag reduction was achieved during the planform optimization, while the resulting drag for the dual step optimization is over 2 counts lower. This 8.7% increase in aerodynamic efficiency compared to the baseline design, yields an L/D of 20.5. The single step shows a drag reduction of 7.5 counts which yields a performance increase of 7.5%. Multiple common features are present in the optimal designs. The sweep angles on the centerbody are high: 70 degrees for the dual step optimized design and 74 degrees for the single step optimized design. The outer wing features 51-degree and 47-degree sweep angles respectively. These were deemed to be beneficial for a limited pitching moment, while also contributing to a lower viscous drag estimate. Shock wave associated wave drag appears to be absent or negligible on all of the presented designs. Hence, it is believed that the aerodynamic load on the outboard wing is reduced to approximate an elliptical lift distribution and thereby minimizes induced drag. This load shifting follows from increased outer wing washout, resulting in an increment in Oswald efficiency factor from 0.86 to 0.92 with a zero-lift drag coefficient of 49.5 counts for the dual-step optimized design. The two optimized designs differ in longitudinal positioning of the outer wing and thus no unambiguous option can be distinguished. Furthermore, cross-sectional shapes that are close to the Sears-Haack body area distribution are attained.

The chosen integration of the fuel tank introduces a relatively long centerbody. This yields low sectional lift coefficients of around 0.05 on the center airfoil. Compared to the dual step optimized design, the CSR-01 kerosene-powered reference aircraft has a 26% lower wetted area. The lift curve slope and the pitching moment derivative at cruise conditions for the dual step optimized design are equal to 2.9 rad^{-1} and -0.064 rad^{-1}

respectively. For the single step optimized design these values are 3.0 rad^{-1} and -0.060 rad^{-1}. The optimized designs display a performance plateau around the design cruise lift coefficient. So, deterioration at off-design performance does not take place.

The estimated aerodynamic performance for the optimized versions looks promising, making medium-range BWB's a suitable liquid hydrogen platform for the future.

6.2. RECOMMENDATIONS & LIMITATIONS

This research indicates the liquid-hydrogen-powered blended-wing-body concept to be promising from an aerodynamic performance perspective. This work aims to provide initial figures on aerodynamic performance and characteristics. During this study, multiple assumptions are made on structures, sizing and cruise conditions. These will need to be verified in other studies. In this process, feasibility on the conceptual and structural perspective will also become clear.

The liquid hydrogen volume taken into account during this project is based on the energy tank content of a kerosene aircraft. To verify that this hydrogen volume is sufficient to fulfill the design mission, the use of the Breguet range equation is required. This equation needs a weight estimation as input. Hence, a structural weight estimation study is recommended to provide further insight into the LH2BWB performance. Also, the estimated weight should yield a cruise lift coefficient that is on the performance plateau of the optimized designs given the reference area and cruise conditions. If the cruise point is not at this plateau, the shapes resulting from this study do potentially not supply optimal aerodynamic performance. The center of gravity positioning is based on yielding a longitudinally stable design. Therefore, a structural study can also verify if this center of gravity position is indeed feasible for the full aircraft design. This study focused on finding the aerodynamic optimal shape of the concept. A multidisciplinary optimization can therefore provide further insight on the optimal shape when other aspects are taken into account as well.

Vertical fins, engines and trim drag were not included in the drag estimation in this study. These should be calculated for a better estimate of overall aircraft performance. They do not only add viscous drag, but potentially also interference drag. Furthermore, the empirical strip method and the Euler solver used in this study cannot accurately model viscous effects. Especially at the trailing edge of the outboard wing, a steep adverse pressure gradient is present of which the effects can only be estimated by using a higher-order solver. These computations can also further verify the viscous drag estimation provided by the strip method.
Also, the dual and single step optimizations appeared to be bounded by the pitching moment constraint that was set. Therefore, it is recommended to assess whether the increase in trim drag cancels out the potential increase in aerodynamic performance when allowing a more negative pitching moment.
Since a single-point optimization is performed, off-design performance is not taken into account. Although performance around the design lift coefficient looks promising, design conditions needed for take-off and landing were not part of the current optimal designs. Therefore it should be looked into if the presented designs comply with the off-design requirements.

A possible configuration for the liquid hydrogen tank is presented in this work. Thereby the liquid hydrogen volume is accounted for. However other tank shapes might yield a more efficient design in terms of weight or volume use. Also, the liquid hydrogen tank was sized with values from the literature. A heat transfer model of the tank needs to be made to further verify the assumed hydrogen boil-off volume. The floor area of the passenger cabin is based on literature values as well. Although an initial seat abreast configuration is provided, a cabin configuration study can provide more insight into the actual passenger capacity since the optimized designs feature a tapered cabin.

Finally, the outer mold line of the aircraft can be further improved. Especially the transition between the centerbody and the wing fairing could benefit from the use of a Gordon Surface. This type of shape allows for more control than the lofted surface used in this study. An implementation of the Gordon Surface in *ParaPy* was not available during this research project.

BIBLIOGRAPHY

[1] A. Westenberger, *Hydrogen fueled aircraft,* in *AIAA International Air and Space Symposium and Exposition: The Next 100 Years, 14 July - 17 July 2003, Dayton, Ohio*.

[2] W. Mason, *Applied computational aerodynamics, volume 1: Foundations and classical pre-cfd methods,* (1992).

[3] M. I. Gerritsma, *Computational Fluid Dynamics* (Delft University Press, Delft, 2002).

[4] K. Risse, K. Schäfer, F. Schültke, and E. Stumpf, *Central reference aircraft data system (ceras) for research community,* CEAS Aeronautical Journal **7**, 121 (2016).

[5] M. Hoogreef, *The Oval Fuselage: A New Structural Design Concept for Blended Wing Body Cabins*, Msc thesis, Delft University of Technology (2012).

[6] B. M. Kulfan, *Universal parametric geometry representation method,* Journal of Aircraft **45**, 142 (2008).

[7] V. Schmitt and F. Charpin, *Pressure distributions on the onera m6 wing at transonic mach numbers,* (1979).

[8] C. Winnefeld, T. Kadyk, B. Bensmann, U. Krewer, and R. Hanke-Rauschenbach, *Modelling and designing cryogenic hydrogen tanks for future aircraft applications,* Energies **11** (2018), 10.3390/en11010105.

[9] G. D. Brewer, *Hydrogen aircraft technology* (CRC Press, Boca Raton, 1991).

[10] *Forecasts of scheduled passenger and freight traffic,* `https://www.icao.int/sustainability/Pages/eap-fp-forecast-scheduled-passenger-traffic.aspx`, accessed: 25-3-2021.

[11] A. Krein and G. Williams, *Flightpath 2050: Europe's vision for aeronautics,* Innovation for Sustainable Aviation in a Global Environment: Proceedings of the Sixth European Aeronautics Days, Madrid **30** (2012).

[12] M. Mazraati, *World aviation fuel demand outlook,* OPEC Energy Review **34**, 42 (2010).

[13] A. G. Rao, F. Yin, and J. P. Van Buijtenen, *A hybrid engine concept for multi-fuel blended wing body,* Aircraft Engineering and Aerospace Technology **86**, 483 (2014).

[14] F. Yin, A. Gangoli Rao, A. Bhat, and M. Chen, *Performance assessment of a multi-fuel hybrid engine for future aircraft,* Aerospace Science and Technology **77**, 217 (2018).

[15] M. Ponater, S. Pechtl, R. Sausen, U. Schumann, and G. Hüttig, *Potential of the cryoplane technology to reduce aircraft climate impact: A state-of-the-art assessment,* Atmospheric Environment **40**, 6928 (2006).

[16] D. R. J. Mukhopadhaya, *Performance analysis of evolutionary hydrogen-powered aircraft,* (2022).

[17] H. G. Klug and R. Faass, *Cryoplane: hydrogen fuelled aircraft — status and challenges,* Air and Space Europe **3**, 252 (2001).

[18] M. Guynn, J. Freh, and E. Olson, *Evaluation of a Hydrogen Fuel Cell Powered Blended-Wing-Body Aircraft Concept for Reduced Noise and Emissions*, Tech. Rep. NASA/TM-2004-212989 (NASA, 2004).

[19] R. H. Liebeck, *Design of the blended wing body subsonic transport,* Journal of Aircraft **41**, 10 (2004).

[20] C. Goldberg, *Techno-economic, Environment and Risk Analysis of an Aircraft Concept with Turbo-electric Distributed Propulsion*, Ph.d dissertation, Cranfield University (2017).

[21] R. Martinez-Val, E. Perez, J. Perez, J. Palacín, E. Aeronauticos, and E. Aeronautica, *Optimising transport flying wings,* in *25th International Congress of the Aeronautical Sciences (ICAS), 3 - 8 September 2006, Hamburg, Germany*, Vol. 1.

[22] E. Torenbeek, *Advanced Aircraft Design : Conceptual Design, Analysis andOptimization of Subsonic Civil Airplanes* (John Wiley Sons, Incorporated, New York,, 2013).

[23] D. Howe, *Blended wing body airframe mass prediction,* Proceedings of the Institution of Mechanical Engineers, Part G: Journal of Aerospace Engineering **215**, 319 (2001).

[24] R. Liebeck, M. Page, and B. Rawdon, *Blended-wing-body subsonic commercial transport,* in *36th AIAA Aerospace Sciences Meeting and Exhibit, 12 January 1998 - 15 January, Reno,NV,U.S.A.*

[25] R. Liebeck, *Blended wing body design challenges,* in *AIAA International Air and Space Symposium and Exposition: The Next 100 Years, 14 July 2003 - 17 July 2003, Dayton, Ohio.*

[26] J. Quinlan and F. H. Gern, *Conceptual design and structural optimization of nasa environmentally responsible aviation (era) hybrid wing body aircraft,* in *57th AIAA/ASCE/AHS/ASC Structures, Structural Dynamics, and Materials Conference, 4 - 8 January 2016 San Diego, California, USA.*

[27] A. Morris, *Mob a european distributed multi-disciplinary design and optimisation project,* in *9th AIAA/ISSMO Symposium on Multidisciplinary Analysis and Optimization, 04 September - 06 September 2002 Atlanta, Georgia.*

[28] N. Qin, A. Vavalle, A. Le Moigne, M. Laban, K. Hackett, and P. Weinerfelt, *Aerodynamic studies for blended wing body aircraft,* in *9th AIAA/ISSMO Symposium on Multidisciplinary Analysis and Optimization.*

[29] N. Qin, A. Vavalle, A. Le Moigne, M. Laban, K. Hackett, and P. Weinerfelt, *Aerodynamic considerations of blended wing body aircraft,* Progress in Aerospace Sciences **40**, 321 (2004).

[30] N. Qin, A. Moigne, and A. Vavalle, *Spanwise lift distribution for blended wing body aircraft,* Journal of Aircraft - J AIRCRAFT **42**, 356 (2005).

[31] M. Brown, *Conceptual design of blended wing body airliners*, Msc thesis, Delft University of Technology (2017).

[32] R. Martinez-Val, C. Cuerno, E. Perez, and H. H. Ghigliazza, *Potential effects of blended wing bodies on the air transportation system,* Journal of Aircraft **47**, 1599 (2010).

[33] P. Okonkwo and H. Smith, *Review of evolving trends in blended wing body aircraft design,* Progress in Aerospace Sciences **82**, 1 (2016).

[34] C. A. Mader and J. R. R. A. Martins, *Stability-constrained aerodynamic shape optimization of flying wings,* Journal of Aircraft **50**, 1431 (2013).

[35] C. Nickol, *Hybrid wing body configuration scaling study,* in *50th AIAA Aerospace Sciences Meeting including the New Horizons Forum and Aerospace Exposition, 09 January - 12 January 2012, Nashville, Tennessee.*

[36] E. M. Greitzer, P. A. Bonnefoy, and E. DelaRosaBlanco, *N+3 Aircraft Concept Designs and Trade Studies*, Tech. Rep. NASA/CR—2010-216794/VOL1 (NASA, 2010).

[37] A. Sóbester and A. I. J. Forrester, *Aircraft Aerodynamic Design : Geometry and Optimization* (John Wiley and Sons, Incorporated, New York, 2014).

[38] S. Siouris and N. Qin, *Study of the effects of wing sweep on the aerodynamic performance of a blended wing body aircraft,* Proceedings of the Institution of Mechanical Engineers, Part G: Journal of Aerospace Engineering **221**, 47 (2007).

[39] Z. Lyu and J. R. R. A. Martins, *Aerodynamic design optimization studies of a blended-wing-body aircraft,* Journal of Aircraft **51**, 1604 (2014).

[40] S. Peigin and B. Epstein, *Computational fluid dynamics driven optimization of blended wing body aircraft,* AIAA Journal **44**, 2736 (2006).

[41] B. Khandelwal, A. Karakurt, P. R. Sekaran, V. Sethi, and R. Singh, *Hydrogen powered aircraft : The future of air transport,* Progress in Aerospace Sciences **60**, 45 (2013).

[42] D. Verstraete, *The Potential of Liquid Hydrogen for long range aircraft propulsion*, Ph.d dissertation, Cranfield University (2009).

[43] C. v. Woensel, *Integration of a Liquid Hydrogen Fuel Tank into the Concept of the Flying-V*, Msc thesis, Delft University of Technology (2021).

[44] H. Smith, *Airframe integration for an lh2 hybrid-electric propulsion system,* Aircraft Engineering and Aerospace Technology **86**, 562 (2014).

[45] E. Torenbeek, *Synthesis of subsonic airplane design : an introduction to the preliminary design, of subsonic general aviation and transport aircraft, with emphasis on layout, aerodynamic design, propulsion, and performance* (Delft University Press, Delft, 1982).

[46] R. Whitford, *Design for air combat* (Jane's, London; New York, 1987).

[47] R. M. Cummings, W. H. Mason, S. A. Morton, and D. R. McDaniel, *Applied Computational Aerodynamics: A Modern Engineering Approach*, Cambridge Aerospace Series (Cambridge University Press, Cambridge, 2015).

[48] R. Vos and S. Farokhi, *Introduction to transonic aerodynamics* (Springer, Dordrecht, 2015).

[49] S. Deck, F. Gand, V. Brunet, and S. Khelil, *High-fidelity simulations of unsteady civil aircraft aerodynamics: Stakes and perspectives. application of zonal detached eddy simulation,* Philosophical transactions. Series A, Mathematical, physical, and engineering sciences **372** (2014), 10.1098/rsta.2013.0325.

[50] P. Li, B. Zhang, Y. Chen, Y. Chang-sheng, and Y. Lin, *Aerodynamic design methodology for blended wing body transport,* Chinese Journal of Aeronautics **25**, 508 (2012).

[51] Y.M.Baan, *A hybrid method for the interior and exterior design of blended-wing-body cabins*, Msc thesis, Delft University of Technology (2015).

[52] R. Vos, F. Geuskens, and M. Hoogreef, *A new structural design concept for blended wing body cabins,* in *53rd AIAA/ASME/ASCE/AHS/ASC Structures, Structural Dynamics and Materials Conference, 23 April - 26 April 2012, Honolulu, Hawaii*.

[53] G. L. Rocca, *Knowledge based engineering: Between ai and cad. review of a language based technology to support engineering design,* Advanced Engineering Informatics **26**, 159 (2012).

[54] M. Hillen, *Parametrisation of the Flying-V Outer Mould Line*, Msc thesis, Delft University of Technology (2021).

[55] F. Faggiano, R. Vos, M. Baan, and R. V. Dijk, *Aerodynamic design of a flying v aircraft,* in *17th AIAA Aviation Technology, Integration, and Operations Conference, 5-9 June 2017, Denver, Colorado*.

[56] M. Brown and R. Vos, *Conceptual design and evaluation of blended-wing body aircraft,* in *2018 AIAA Aerospace Sciences Meeting, 8–12 January 2018 Kissimmee, Florida*.

[57] K. Price, R. Storn, and J. Lampinen, *Differential Evolution: A Practical Approach to Global Optimization* (Springer Berlin Heidelberg, 2006).

[58] T. Laughlin, J. Corman, and D. Mavris, *A parametric and physics-based approach to structural weight estimation of the hybrid wing body aircraft,* (2013).

[59] M.-F. Liou, D. Gronstal, H. J. Kim, and M.-S. Liou, *Aerodynamic design of the hybrid wing body with nacelle: N3-x propulsion-airframe configuration,* in *34th AIAA Applied Aerodynamics Conference, 13-17 June 2016*.

[60] D. A. Masters, N. J. Taylor, T. C. S. Rendall, C. B. Allen, and D. J. Poole, *Geometric comparison of aerofoil shape parameterization methods,* AIAA Journal **55**, 1575 (2017).

[61] B. Kulfan and J. Bussoletti, *"fundamental" parameteric geometry representations for aircraft component shapes,* in *11th AIAA/ISSMO Multidisciplinary Analysis and Optimization Conference, 06 September - 08 September 2006*.

[62] M. Meheut, A. Arntz, and G. Carrier, *Aerodynamic shape optimizations of a blended wing body configuration for several wing planforms,* in *30th AIAA Applied Aerodynamics Conference 2012, 25 June - 28 June 2012, New Orleans, Louisiana*.

[63] D. W. Zingg, M. Nemec, and T. H. Pulliam, *A comparative evaluation of genetic and gradient-based algorithms applied to aerodynamic optimization,* European Journal of Computational Mechanics **17**, 103 (2008).

[64] R. Storn and K. Price, *Differential evolution – a simple and efficient heuristic for global optimization over continuous spaces,* Journal of Global Optimization **11**, 341 (1997).

[65] O. Hrstka, A. Kučerová, M. Lepš, and J. Zeman, *A competitive comparison of different types of evolutionary algorithms,* Computers Structures **81**, 1979 (2003).

[66] P. Y. Papalambros and D. J. Wilde, *Principles of optimal design : modeling and computation*, second edition. ed. (Cambridge University Press, Cambridge, 2000).

[67] Z. Michalewicz and M. Schoenauer, *Schoenauer, m.: Evolutionary algorithms for constrained parameter optimization problems. evolutionary computation 4(1), 1-32,* Evolutionary Computation **4**, 1 (1996).

[68] O. Gur, W. Mason, and J. Schetz, *Full-configuration drag estimation,* Journal of Aircraft - J AIRCRAFT **47**, 1356 (2010).

[69] D. P. Raymer, *Aircraft design : a conceptual approach*, 4th ed., AIAA education series (American Institute of Aeronautics and Astronautics, Reston, Va., 2006).

[70] N. Durrani and N. Qin, *Comparison of rans, des and ddes results for onera m-6 wing at transonic flow speed using an in-house parallel code,* in *49th AIAA Aerospace Sciences Meeting including the New Horizons Forum and Aerospace Exposition, Orlando, Florida*.

[71] J. Mayeur, A. Dumont, D. Destarac, and V. Gleize, *Reynolds-averaged navier-stokes simulations on naca0012 and onera-m6 wing with the onera elsa solver,* AIAA Journal **54**, 2671 (2016), cited By :15 Export Date: 18 June 2021.

[72] B. Eisfeld, *Onera m6 wing,* in *FLOMANIA — A European Initiative on Flow Physics Modelling*, edited by W. Haase, B. Aupoix, U. Bunge, and D. Schwamborn (Springer Berlin Heidelberg) pp. 219–224.

[73] *Onera m6 wing,* `https://www.grc.nasa.gov/www/wind/valid/m6wing/m6wing.html`, accessed: 17-5-2021.

[74] R. Gilmore, S. Wakayama, and D. Roman, *Optimization of high-subsonic blended-wing-body configurations,* in *9th AIAA/ISSMO Symposium on Multidisciplinary Analysis and Optimization, 04 September - 06 September 2002, Atlanta, Georgia*.

[75] T. A. Reist and D. W. Zingg, *Aerodynamic shape optimization of a blended-wing-body regional transport for a short range mission,* in *31st AIAA Applied Aerodynamics Conference, June 24-27, 2013, San Diego, CA*.

[76] E. Obert, *Aerodynamic Design of Transport Aircraft*, Aerodynamic Design of Transport Aircraft (Delft University Press, Delft, 2009).

[77] *Csr-01 reference aircraft data,* `https://ceras.ilr.rwth-aachen.de/tiki/tiki-index.php?page=CSR-01&structure=CeRAS`, accessed: 11-11-2021.

[78] T. A. Reist and D. W. Zingg, *Aerodynamic design of blended wing-body and lifting-fuselage aircraft,* in *34th AIAA Applied Aerodynamics Conference, 13-17 June 2016, Washington, D.C.*

[79] D. M. Pitera, M. A. DeHaan, D. Brown, R. T. Kawai, S. Hollowell, P. Camacho, D. Bruns, and B. K. Rawden, *Blended Wing Body Concept Development with Open Rotor Engine Intergration*, Tech. Rep. Tech. Rep. NASA/CR–2011-217303 (Boeing and NASA, 2011).

[80] R. T. Kawai, *Acoustic Prediction Methodology and Test Validation for an Efficient Low-Noise Hybrid Wing Body Subsonic Transport*, Tech. Rep. Tech. Rep. NF1676L-14465 (NASA, 2011).

[81] J. Frota, K. Nicholls, J. Whurr, M. Müller, P.-E. Gall, J. Loerke, K. Macgregor, P. Schmollgruber, J. Russell, M. Hepperle, S. Rodriguez, K. Taupin, J.-L. Godard, S. Dron, and K. Plötner, *Nacre - new aircraft concepts research: Final activity report 2005 – 2010"*, Tech. Rep. (Airbus SAS, 2011).

[82] J. Hileman, Z. Spakovszky, M. Drela, M. Sargeant, and A. Jones, *Airframe design for silent fuel-efficient aircraft,* Journal of Aircraft **47**, 956 (2010).

[83] S. Yang, M. Page, and E. J. Smetak, *Achievement of nasa new aviation horizons n+2 goals with a blended-wing-body x-plane designed for the regional jet and single-aisle jet markets,* in *2018 AIAA Aerospace Sciences Meeting* (2018).

A

UML DIAGRAM

A UML diagram for the classes used in the ParaPy code, is presented in Figure A.1. As can be seen, **LH2BWBaircraft** forms the main class. The **Winglet** class is not utilized in this study, but can be used for future research.

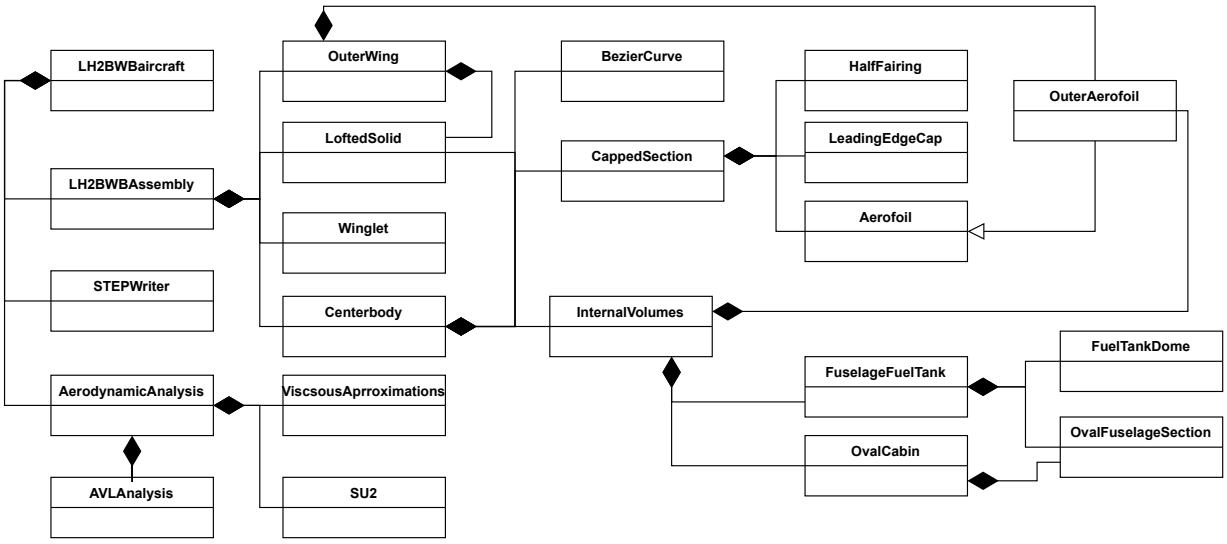

Figure A.1: UML diagram for the LH2BWB ParaPy implementation

B

ADDITIONAL TABLES

To provide further insight into the settings used in this study, additional tables are presented here. Table B.1 presents the bounds used for the variables during optimization. Table B.2 shows the mesh settings used during the grid convergence study presented in Section 4.3.

Table B.1: Variable bound values used during optimization. The format is (lower bound, upper bound) and values are relative to the baseline design. Except for the twist bounds, which are absolute.

	Variable	Planform opt.	Dual step opt.	Single step opt.
Planform	c_{center}	(0.95, 1.05)	-	(0.95, 1.05)
	c_{ow}	(0.7, 1.3)	-	(0.7, 1.3)
	Λ_{cb}	(0.85, 1.1)	-	(0.85, 1.1)
	Λ_{ow}	(0.8, 1.2)	-	(0.8, 1.2)
	b_{ow}	(0.5, 1.25)	-	(0.5, 1.25)
	ϵ_3 [°]	(-0.5, 2.5)	(-0.5, 1.0)	(-0.5, 1.0)
	ϵ_4 [°]	(-1.5,1.5)	(-1, 0.5)	(-1, 0.5)
	ϵ_5 [°]	(-4.5,-1)	(-4, -2.5)	(-4, -2.5)
	μ_{ow}	(0.75, 1.1)	-	(0.75, 1.1)
	ϕ_{kink}	(0.8, 1.2)	-	(0.8, 1.2)
	λ_{ow}	(0.8, 1.2)	-	(0.8, 1.2)
	$w_{\text{TE,outline}}$	(0.5, 2.5)	-	(0.5, 2.5)
LE caps	$w_{\text{up,1}}$	-	(0.5, 2)	-
	$w_{\text{low,1}}$	-	(0.5, 2)	-
	$w_{\text{up,2}}$	-	(0.5, 2)	-
	$w_{\text{low,2}}$	-	(0.5, 2)	-
TE caps	$z_{\text{TE,1}}$	-	(0.7,1.25)	(0.7, 1.25)
	$z_{\text{TE,2}}$	-	(0.7,1.25)	-

Table B.2: Overview of the mesh settings used in the grid convergence study

Nodes per length	Max size wing	Max size outer domain	Growth rate triangles	Max size tetrahedrons	Growth rate tetrahedrons	Number of volumes	Number of nodes
10	0.15	30	0.16	30	0.5	404682	95354
11	0.142	28.5	0.15	28.5	0.475	482594	112349
12	0.135	27	0.144	27	0.45	592723	134177
14	0.12	24	0.13	24	0.425	803987	178735
17	0.1	19.5	0.1	19.5	0.325	1186643	25970
20	0.075	15	0.08	15	0.25	2055258	439013
22	0.068	13.5	0.07	13.5	0.225	3240093	656633

C

Additional Cross-Sectional Area Distributions

Figure C.1 presents the cross-sectional area distribution for each design separately. Also the the Sears-Haack body is plotted for each design, based on the design volume and length.

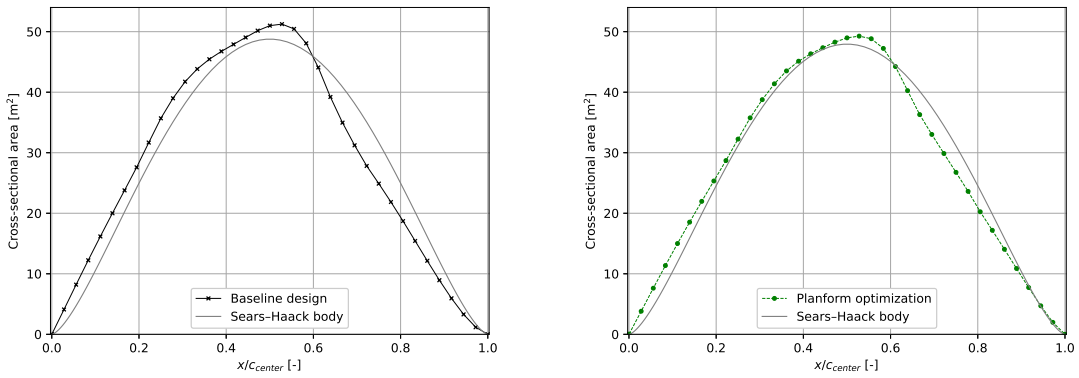

(a) Baseline

(b) Planform Optimized

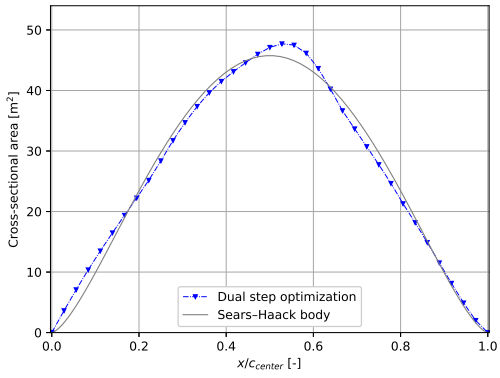

(c) Dual Step Optimized

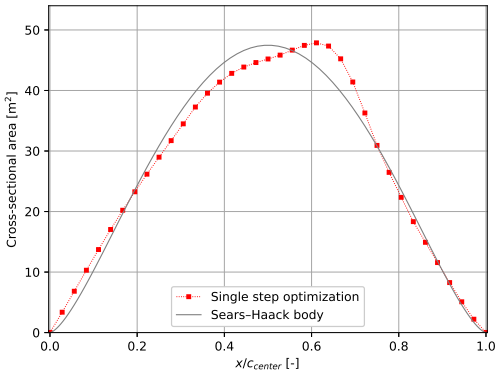

(d) Single Step Optimized

Figure C.1: Cross-sectional area distributions plotted separately for the four designs used in this study

D

BWB Performance in Literature

Table D.1: Overview of characteristics on different BWB's from literature

Aircraft	Range [km]	Pax [-]	MTOM [10^3 kg]	OEM [10^3 kg]	Payload [10^3 kg]	Cruise Mach [-]	Initial cruise altitude [m]	L/D [-]	AR [-]	Source
H3.2	14075	354	213	95	61	0.83	10644	24.2	4.74	[36]
BWB100-1	926	100	55	33		0.78	10973	23		[78]
BWB160-1	1852	160	99	57		0.79	10973	26.6		[78]
BWB220-1	5556	220	196	100		0.8	10973	28.9		[78]
BWB300-1	11112	300	375	189		0.84	10973	30		[78]
HWB98	4445	98	46	29	10	0.78		20.7		[35]
HWB160	5325	160	75	46	17	0.78		23.1		[35]
HWB216	12223	216	130	70	20	0.8		22.3		[35]
HWB301	13890	301	246	119	54	0.84		23.5		[35]
HWB400	10742	400	315	169	67	0.85		23.7		[35]
OREIO BL	12038		216	113	45		10672	23.3	5.646	[79]
N2A-EXTE	11112		214	102	47	0.81	11808	21.4		[80]
Boeing BWB	12964	800	373	187				23		[19]
N2A	11112		209	99	47	0.79	10668	21.5		[80]
N2B	11112		217	103	47	0.8	10668	21.4		[80]
VELA 3		750	700	327				22.1		[81]
NACRE-FW2		750	630	309				23.4		[81]
SAX-40	9260	215	151	94	23	0.8	12192	25.1		[82]
Ascent 1000	5926	112	47	30				21.6		[83]